Relative Measurement for Kinematic Calibration Using Digital Image Processing

by

Andrew A. Fratpietro, B.Eng.

Carleton University

A thesis submitted to

the Faculty of Graduate Studies and Research

in partial fulfillment of

the requirements for the degree of

Master of Applied Science

Ottawa-Carleton Institute for

Mechanical and Aerospace Engineering

Department of

Mechanical and Aerospace Engineering

Carleton University

Ottawa, Ontario

Sept 7, 2004

Your file Votre référence
ISBN: 0-612-97407-3
Our file Notre référence
ISBN: 0-612-97407-3

The undersigned recommend to

the Faculty of Graduate Studies and Research

acceptance of the thesis

Relative Measurement for Kinematic Calibration

Using Digital Image Processing

submitted by **Andrew A. Fratpietro, B.Eng.**

in partial fulfillment of the requirements for

the degree of Master of Applied Science

Dr. M. J. D. Hayes
Thesis Supervisor

Dr. J. C. Beddoes
Chair, Department of
Mechanical and Aerospace Engineering

Carleton University

Sept 7, 2004

Abstract

A camera-based robot measurement system is developed for the purpose of extracting relative measurements from sets of digital images for use in kinematic calibration. The system consists of a camera, lens, LED array, measurement head, data acquisition equipment and a precision-machined measurement artifact. A set of design requirements are established in order to drive the design of an image processing algorithm. The algorithm is developed using the MATLAB environment to process the digital images and extract metric information regarding the displacement error of a robotic end-effector in the X-Y plane of the robot workspace. Two novel post-processing algorithms are applied to the metric data in order to produce the relative measurements. One of these algorithms facilitates the removal of perspective distortion from image data, while the other is applied during cases where perspective distortion removal is not possible. The resolution provided by this relative measurement system is improved through the study of several parameters within the image processing algorithm and the final algorithm is characterized. This system is able to extract relative measurements to a mean resolution of ± 0.008 mm over a maximum displacement of ± 0.8 mm in the X direction and ± 0.5 mm in the Y direction. This mean resolution is approximately an order of magnitude less than the repeatability of the robotic manipulator to which the system is applied. Several suggestions for improving the resolution of this system are presented.

Acknowledgements

I would like to acknowledge the generous financial support of Machines and Manufacturing Ontario during my tenure at Carleton University.

I would also like to thank Professor M. John. D. Hayes for his guidance and critical feedback of this work. For this and for passing on his passion for fine beer, I am deeply in his debt.

I would like to extend my appreciation to Nick Simpson for offering up long hours of lab time in finding *glitches* in the software.

Most of all, I would like to acknowledge the fantastic support of the love of my life, Jill. Thank you for helping me through the difficult times.

List of Symbols

Subscripts:

x, y, z	x component, y component, z component
i, j	matrix indices for rows and columns

Superscripts:

H	*Robot hand* coordinate system
R	*Robot base* coordinate system
B	*Calibration body* coordinate system
C	Camera

Variables:

ρ	Scaling factor for homogeneous transformation
η	Slope of line of the form $y = \eta x + b$
b	Intercept of line of the form $y = \eta x + b$

Vectors:

$\mathbf{P}$	Robot pose vector
$\mathbf{q}$	Coordinate vector in the *World* coordinate system
$\mathbf{p}$	Coordinate vector in the *Image* coordinate System

Matrices:

$\mathbf{T}$	Transformation Matrix

Contents

List of Figures

List of Tables

Claim of Originality

Certain aspects of digital image processing with applications to relative measurement are presented herein for the first time. The following contributions are of particular interest:

1. The custom-tailored algorithm for the extraction of measurements from images of a precision-machined ruled-surface.

2. The validation procedure that quantifies measurement error for the aforementioned algorithm.

3. The description of the volume over which a particular camera-based calibration system can be applied.

4. The parametric study of the effects that certain parameters have on the measurement error resulting from this algorithm.

5. The novel test region used in the segmentation of lines from a digital image.

Parts of these results have appeared in three refereed publications and technical reports: [1, 2, 3].

Chapter 1

Introduction

The pose of a robot end-effector in Cartesian coordinates is determined by a combination of the robot joints used to control this pose (the forward kinematics). Alternately, the orientation of each of these robot joints can be determined based on the Cartesian pose of the robot (the inverse kinematics). In these two cases, the robot is described by either its Cartesian variables in the *Task Space* or by its joint variables in the *Joint Space*. Using one set of robot variables and a system of equations referred to as the kinematic model of the manipulator, one can transform one set of variables into the other. Joint variables describe the length or angle of each of the active joints that comprise the manipulator. In the case of an articulated, six degree-of-freedom robot with six revolute joints, the joint variables consist of six angles. These angles are used by the robot controller to move the robot. The Cartesian pose of this same articulated manipulator consists of three positional coordinates of an end-effector reference point and three orientation angles of an end-effector reference line. These variables allow the user to describe the pose of the robot.

In manipulating a robot, it is important to be able to map between these sets of variables. The user inputs the desired Cartesian pose of the manipulator into the robot controller. The controller must then transform these coordinates into a set of joint vari-

ables. These variables are used to control each joint in order to achieve the desired pose. The transformation from Cartesian pose to joint variables is referred to as the inverse kinematic transformation of the robot and requires the kinematic model of the manipulator. Most, if not all, robot controllers come equipped with this kinematic model, but due to manufacturing tolerances and assembly issues it is likely that this model does not accurately represent the robotic system. Certain parameters in the model, such as link lengths, will deviate from their actual values by some quantifiable difference. As a result, the robot will only be able to achieve accuracy in its pose up to some specified value. For some purposes, this lack of accuracy in robot pose is unacceptable. It is the purpose of kinematic calibration to identify these deviations and correct the kinematic model of the robot in order to increase the accuracy of its desired pose [4, 5].

The use of digital cameras in robotic calibration has increased rapidly over the past two decades [6, 7, 8] and there are a number of advantages that justify this research. In general, using a measurement device that does not require physical contact with any reference object in the robot workspace results in less contamination of the measurements than those produced using a contact device [9]. Optical-based devices do not require any physical contact with the workspace. One advantage of camera-based calibration is the relatively low cost of using images as opposed to alternative means which can result in up to an order of magnitude in cost-savings. Also, digital images have the potential to produce data that is as accurate as the more expensive devices such as tracking laser interferometers and coordinate measuring machines. It is easy to see the importance of such devices when one considers that the behaviours that robots are trying to emulate are anthropomorphic, and that one of the more important human senses used in the completion of these tasks is vision. For a human, a task such as picking up an apple seems trivial. One locates the apple using vision and then proceeds to move ones hand into a position to grab the apple. Little consideration is given to the location of the hand with respect to the eyes, but only

because such a routine has likely been accomplished hundreds of thousands of times over the course of one's life. The repetition of this motion has provided the human with a strong idea of where the hand is located with respect to the eyes. For most robotic systems using a camera, the transformation from camera to robot hand must be calculated and included in the robot kinematic model. The calculation of this transformation is referred to as the hand-eye calibration problem and has been well documented in robotic literature since the late 1980s [10, 11].

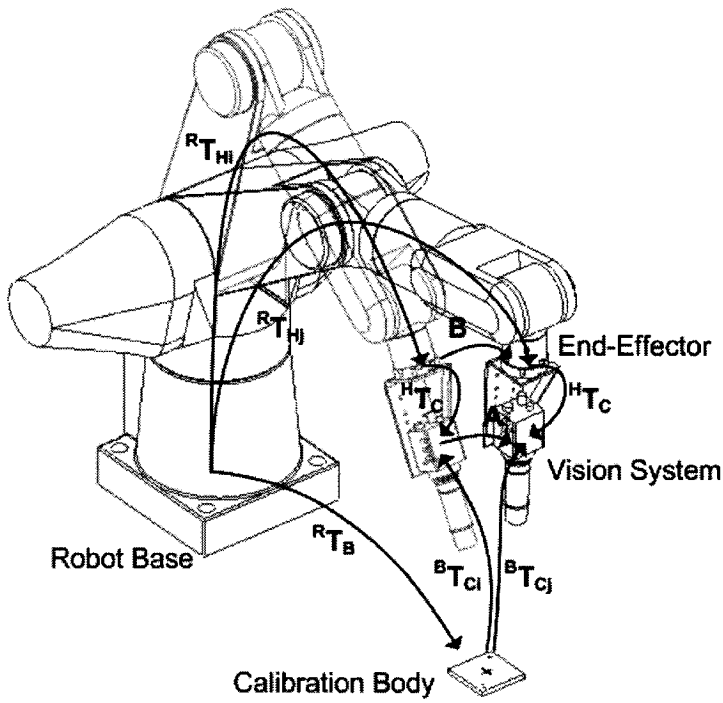

Figure 1.1: Transformations involved in robot hand-eye calibration.

In its simplest form, the hand-eye problem can be stated as the solution of the homogeneous transformation equation of the form $\mathbf{AX} = \mathbf{XB}$, where the matrix $\mathbf{X}$ represents the transformation from the robot-hand coordinate system to the camera coordinate system and is referred to as the hand-eye transformation. This transformation can also be denoted as seen in Equation 1.1.

$$\mathbf{X} = {}^{\mathbf{H}}\mathbf{T}_{\mathbf{C}}. \tag{1.1}$$

$\mathbf{X}$ is the unknown quantity in this problem. The matrix $\mathbf{B}$ represents the transformation between robot-hand poses. The coefficients of this matrix can be calculated from the robot joint encoder readings before and after an arm movement. The matrix $\mathbf{A}$ represents the transformation between camera positions before and after a robot movement. Assuming that the intrinsic parameters of the camera are already known, the coefficients of this matrix can be calculated using three dimensional geometry and a camera image recorded before and after each robot movement. In order to increase the accuracy in the solution of $\mathbf{X}$, several different robot arm poses are required resulting in the equation of the form $\mathbf{A}_n\mathbf{X} = \mathbf{X}\mathbf{B}_n$, where n represents the number of robot pose changes. Figure 1.1 shows the physical relationship between the parameters $\mathbf{A}$, $\mathbf{B}$ and $\mathbf{X}$. Considering that the indices i and j represent the initial and final pose of the robot, the matrix $\mathbf{A}$ can also be written as,

$$\mathbf{A} = {}^{\mathbf{B}}\mathbf{T}_{\mathbf{C}_j} {}^{\mathbf{B}}\mathbf{T}_{\mathbf{C}_i}{}^{-1}. \tag{1.2}$$

Where ${}^{\mathbf{B}}\mathbf{T}_{\mathbf{C}_j}$ represents the geometric transformation from a coordinate system originating on a reference body being viewed by the camera (B) to the robot camera coordinate system (C). The matrix $\mathbf{B}$ can be written as,

$$\mathbf{B} = {}^{\mathbf{R}}\mathbf{T}_{\mathbf{H}_j} {}^{\mathbf{R}}\mathbf{T}_{\mathbf{H}_i}{}^{-1}. \tag{1.3}$$

Where ${}^{\mathbf{R}}\mathbf{T}_{\mathbf{H}_j}$ represents the geometric transformation from the robot base coordinate system (R) to the robot hand coordinate system (H). For each robot movement, one $\mathbf{A}$ and one $\mathbf{B}$ matrix can be produced for the solution of $\mathbf{X}$.

The classical procedure presented above provides the hand-eye transformation matrix.

Remy et al. [12] advanced this approach by simultaneously considering the determination of the hand-eye transformation as well as the location of a calibration object in the robot world coordinate system. The calibration object that is implemented is a tetrahedron with each of its vertices illuminated by a single light emitting diode (LED). These LEDs make the vertices of the artifact more visible in the eye of the camera. A fifth LED is located beside the tetrahedron to allow the distinction between similar looking points of view. With this method, the robot is moved to n different positions and, at each position, an image of the calibration object is acquired. The data from these images is used to formulate equations solving for the best hand-eye transformation and the most likely location of the calibration object in the robot world coordinate system.

Ma [13] presents a new formulation of the hand-eye calibration problem as well as a technique for the intrinsic calibration of a camera. The latter technique is referred to as camera self-calibration since it requires no reference calibration object and uses images of the environment. This method takes advantage of the fact that the vision system is fully active by using specially designed robot motions in producing calibration data. Dongmin [14] applies a dual quaternion representation to the translational and rotational displacements associated with the hand-eye transformation. The use of a dual quaternion representation results in a computationally simple closed form solution when compared to some previously performed work using a quaternion representation and screw theory. This representation also allows the computation of unique solutions in situations where previous attempts have failed. The kinematic parameters are computed using an off-line non-linear regression method (gradient descent) and both translation and rotation are considered simultaneously.

Tsai [15] provides an example of the application of a radial alignment constraint method for the purpose of calibrating both the extrinsic and intrinsic parameters of a vision system. The emphasis in this paper is placed on determining the location of the camera centre and

calibrating a value referred to as the horizontal scale factor.

Zhuang and Wu [16] present a modification of Tsai's Radial Alignment Constraint method (RAC) to be used for hand-eye calibration. This modification addresses the issue that arises when the plane of the camera being calibrated is near parallel to the plane of the calibration board from which data is being extracted. This is referred to as a singular point of the system. Such a configuration can be observed by the application of Tsai's RAC method to the calibration of a SCARA.

In 1995, Horaud and Dornaika [17] wrote a paper presenting a modified approach to the hand-eye calibration problem involving the separation of the camera extrinsic and intrinsic parameters and the resulting errors. Zhuang [18] builds on the concepts discussed in this paper and reveals the merits and limitations of the concepts that are discussed. One such merit is the explanation that intrinsic and extrinsic camera parameters need not be made explicit due to the representation errors that this separation may cause. Another concept from [17] is the use of the pinhole camera model in decomposing the camera perspective matrices into intrinsic and extrinsic parameters. Zhuang [18] discusses that a complicated camera model should be used in this case in order to avoid compromising the accuracy of the system.

A method of self-calibration is presented by Wei et al. [19]. This procedure is applied to robots using active motion. The method is based on the tracking of a set of arbitrary world coordinate points. The location of these points is not required and can be estimated by the procedure. This method is iterative, but all initial conditions are determined through the solution of a set of closed form non-linear equations. As an extension of Tsai's RAC method, it is stated that the following modifications provide more accurate results than the original method. The image centre is assumed to be located at the apparent image centre. The image centre, focal lengths, the radial distortion parameter and external parameters are estimated simultaneously using global optimization.

The significance of the hand-eye calibration problem is that vision systems used for the purpose of robot kinematic calibration require that the transformation from the robot hand to the camera ${}^{\mathbf{H}}\mathbf{T}_{\mathbf{C}}$ be computed. The use of this transformation allows the absolute position of the robot hand to be extracted and used in the calibration procedure. In recent years, a novel concept [20] has been developed for the purpose of robot calibration that circumvents the requirement for determining this hand-eye transformation. Instead of using absolute measurements of the robot end-effector for robot kinematic calibration, this method uses relative measurements. A measurement of the position of the robot end-effector taken before a robot motion is compared to a measurement taken after a robot motion. Neither of these measurements contain the absolute position of the robot end-effector. Upon comparison of these measurements, the resulting value describes the relative displacement of the robot end-effector subjected to a planar motion.

The Denavit-Hartenberg (DH) parametrization is used to represent the kinematic model of the robotic manipulator. In general, there are four types of DH parameters. The first parameter, φ, is used to describe the angular position of each of the robot joints. In the case of describing an articulated manipulator with 6 revolute joints, the value of this parameter is dependant on the pose of the robot. The remaining parameters remain constant. The parameter α describes the angular offset between adjacent joints. The parameters a and d describe offset distance between a joint axis and an adjacent joint and the distance along a joint axis between a set of adjacent joints, respectively. One set of four parameters is required to properly model each joint on the manipulator. A more detailed description of the DH parameters and their usage in the relative measurement concept is available [21]. The general relationship between robot pose and DH parameters is seen in Equation 1.4.

$$ {}^{\mathbf{B}}\mathbf{P} = \mathbf{f}(\boldsymbol{\rho}). \tag{1.4} $$

In this relationship, ${}^{\mathbf{B}}\mathbf{P}$ is the pose of the robot end-effector with respect to the robot base coordinate system, $\boldsymbol{\rho}$ is the $4n \times 1$ vector of DH parameters used to represent the kinematic model of the manipulator and $\mathbf{f}(\boldsymbol{\rho})$ is the transformation between the robot base coordinate system and the robot end-effector. In taking the derivative of this equation with respect to the DH parameters, Equation 1.4 takes the form of Equation 1.5, which is then rearranged to the form of Equation 1.6.

$$\frac{\Delta^{\mathbf{B}}\mathbf{P}}{\Delta\boldsymbol{\rho}} \approx \frac{\partial \mathbf{f}}{\partial \boldsymbol{\rho}}, \tag{1.5}$$

$$\Delta^{\mathbf{B}}\mathbf{P} \approx \frac{\partial \mathbf{f}}{\partial \boldsymbol{\rho}}\Delta\boldsymbol{\rho} = \mathbf{J}\Delta\boldsymbol{\rho}. \tag{1.6}$$

Using the formulation of Equation 1.6, it is observed that the error in the measurement of robot pose ($\Delta^{\mathbf{B}}\mathbf{P}$) is equal to the product of the full positional Jacobian ($\mathbf{J}$) and the error in the DH parameters. The purpose of this calibration procedure is to identify and remove the errors in the DH parameters used to represent this system. The pose of the robot is usually described by six independent parameters. Three of these parameters describe the position of the robot end-effector. The other three parameters describe the orientation of the robot end-effector. Since these parameters are independent, all six of them are not required in order to establish a set of equations to be used in the calibration of the robot. These equations can be established using any subset of the six parameters. In order to keep the cost of this system relatively low, the only measurements that are used in this calibration scheme are the displacements in the 3×1 positional vector as seen in Equation 1.7.

$$\mathbf{X} = \begin{bmatrix} \Delta x \\ \Delta y \\ \Delta z \end{bmatrix}. \tag{1.7}$$

Given these positional displacements, the formulation of Equation 1.8 establishes the relationship between relative displacements and the D-H parameters, which are used to model the geometry of the robotic manipulator.

$$\begin{bmatrix} \Delta x \\ \Delta y \\ \Delta z \end{bmatrix} = \mathbf{J} \begin{bmatrix} \Delta \boldsymbol{\varphi} \\ \Delta \boldsymbol{\alpha} \\ \Delta \mathbf{a} \\ \Delta \mathbf{d} \end{bmatrix}. \tag{1.8}$$

The solution of this problem is discussed further in the literature [22, 23, 24]. In order for any of these solutions to work, it is important that the positional displacements in the vector of Equation 1.7 be accurately measured. There are two components to this positional measurement that are proposed for this measurement concept. The first component is the measurement of displacement in the Z direction of the world coordinate system. This measurement is produced using a laser distance sensor referencing a precision-machined flat surface in the $X - Y$ plane of the robot workspace. Only initial work was performed on this concept and it is not discussed in this thesis. The second component of measurement is the displacement of the robot end-effector in the $X - Y$ plane. The motivation of this thesis is to develop a calibration system for the purpose of producing these planar displacements. In general, the system consists of a CCD camera mounted through a measurement head onto the robot end-effector. This camera is positioned at various points along a measurement artifact and used for capturing images. The ruler has been used as a measuring device for many years: long before the development of

robotic manipulators. The accuracy of measurements produced using such a device has never been high enough to allow these measurements to be applied to any high-accuracy calibration scheme. The novel concept described in this thesis is extraction of high accuracy measurements using a precision-machined ruled surface with graduations placed at 1 mm increments. As illustrated in Figure 1.2, the robot moves the camera to a specified initial position at which point an image of the surface of the ruler is captured. This initial image is known as the reference image because it references the position of the robot end-effector before robot motion. The robot then moves the camera to a second position along the length of the ruler and another image is captured.

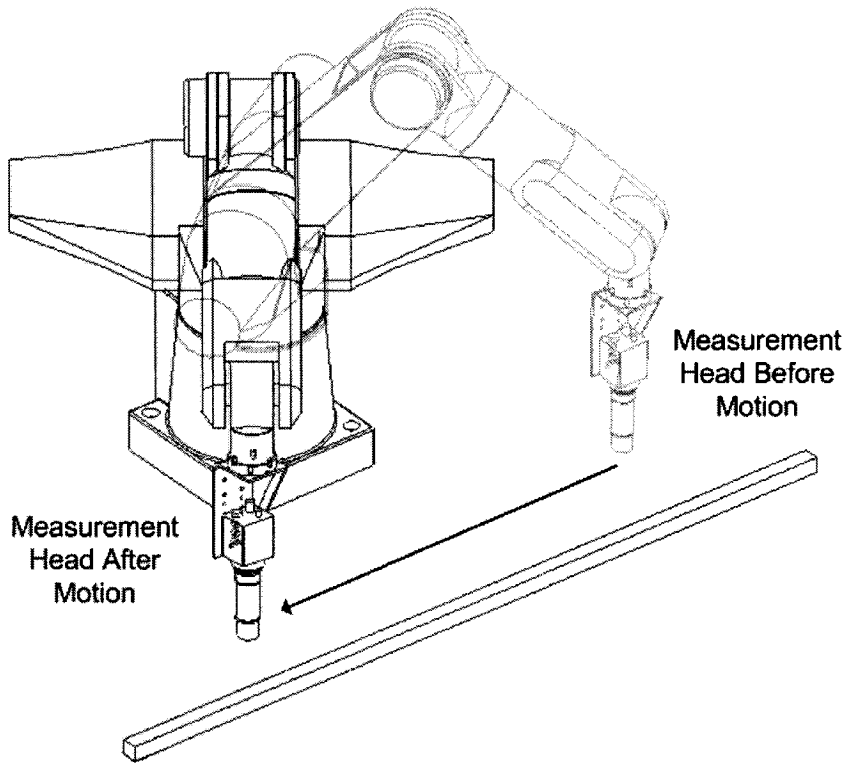

Figure 1.2: Typical measurement head orientation before and after robot motion.

A typical set of images captured during this process can be seen in Figure 1.3. The image on the left side of the figure is captured before robot motion and the image on the right side of the figure is captured after the robot motion. The distance between the two

positions described by these images is selected so that the ruled surface should appear identical in both images. This requires that the robot move in increment-multiples of 5 mm along the ruler. Any deviation observed between the two images of the ruled surface is used to indicate the displacement of the robot relative to its desired position. In this particular example, the displacement between these two images in the i and j directions is large enough to be visible to the human eye. One can note that these displacements can be visually estimated resulting in displacements given in the unit pixels. Digital image processing is used to achieve a higher degree of accuracy in these measurements, as well as proper scale and alignment.

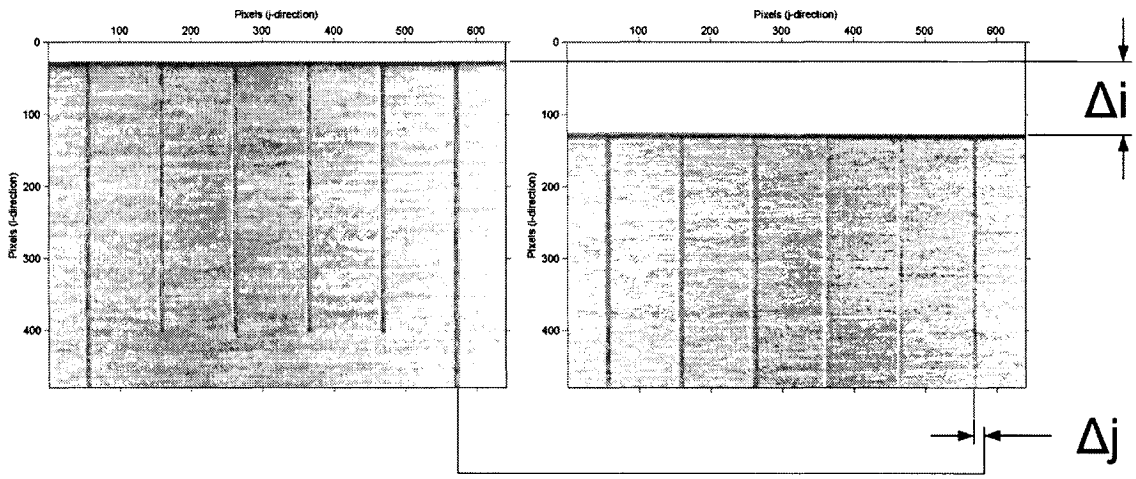

Figure 1.3: Comparison of images captured before and after robot motion.

There are a number of important steps [25, 26, 27] that have been developed over the years in order to extract metric information from images. Selecting and refining these steps for a specific application is the job of the algorithm developer. The subsequent chapters in this thesis describe the process of developing an algorithm for extracting metric information from these digital images. This process begins with the definition of design requirements and design limitations in Chapter 2. The different phases of the algorithm are each presented, along with a description of how they work, in Chapter 3. Chapter 4 offers a comparison between several available algorithms for different steps within the overall

process. A characterization of the final algorithm is also presented. In Chapter 5, some concluding remarks on the image processing algorithm are presented. This chapter also gives several recommendations for future work that can be performed in the development of this system.

Chapter 2

Calibration System Components

Several components are required in order to produce the relative measurements used by this calibration system. The selection of each component in the system is based on two conflicting, yet desirable, characteristics that the system should possess. The first system characteristic is that it should provide measurements that are as accurate as are required in order to calibrate the robotic manipulator to which it will be applied. The robot in question is the Thermo CRS A465 and is described further in Section 2.1.1. The second requirement is that the cost of the system remain low relative to that of comparable systems. A baseline design for this specific system was developed in an earlier design iteration. Using this design as a guideline, a list of specific system components is compiled. This list is displayed in Table A.7. This table, along with further analysis of the selection of each component, is available in Appendix A. The selection of several of the components imposes certain limitations on the output of the system. These components, along with their limitations, are discussed in the following sections.

2.1 Equipment

The description of equipment that is used to produce the results in subsequent chapters is divided into two sections. The first section is used to describe the device to which the calibration system is applied: the Thermo CRS A465 articulated robotic manipulator. Several requirements are placed on the extraction of measurements based on the selection of this robot. The second section describes the equipment that has been selected for the purpose of robot calibration. The use of specific components imposes limitations on the best possible result that can be produced by the system. Based on the characteristics of both the robot and the calibration equipment, a geometric region can be visualized. This region is bounded by the maximum possible results and minimum requirements that the calibration system can and must produce. This region is used to assess the performance of the image processing algorithm described in Chapter 3.

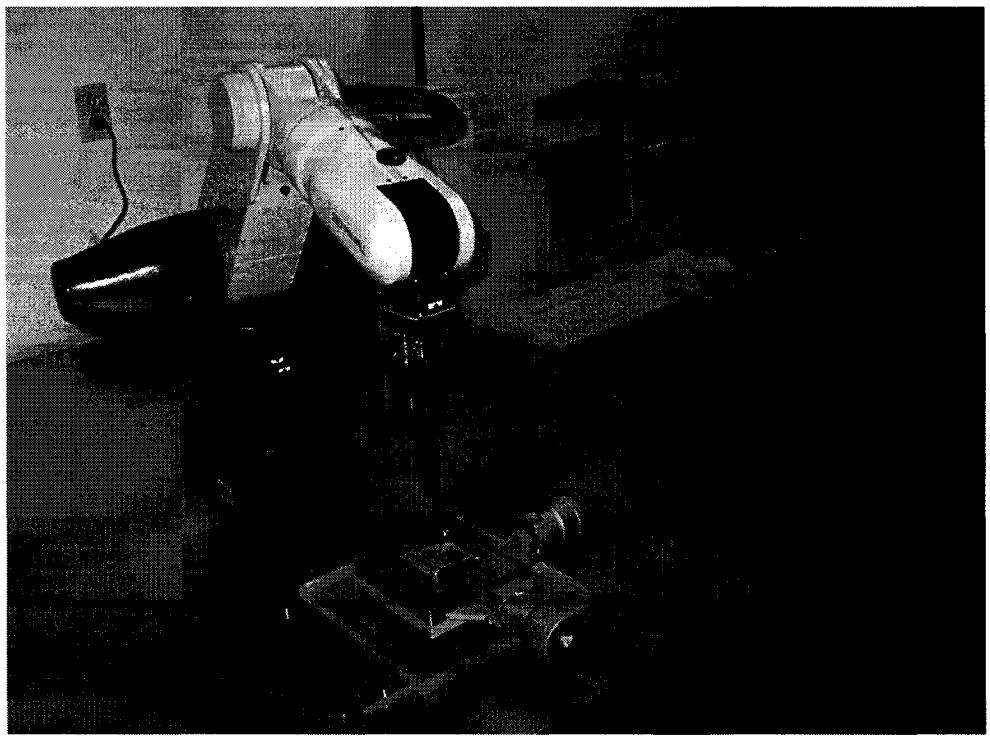

Figure 2.1: Configuration of the robot work area.

2.1.1 Thermo CRS A465 Robotic Manipulator

The Thermo CRS A465 robotic manipulator is an articulated arm consisting of 6 serially connected revolute joints and a total arm span of 710 mm. A robot controller is used to integrate the arm with a standard personal computer used to manipulate the robot. The configuration of this working environment can be viewed in Figure 2.1. The robot is rated as having a positional repeatability of ± 0.050 mm. It has been previously determined that a robot kinematic model can only be calibrated up to a value equal to its repeatability [28]. As a result, any relative measurement used to describe the deviation in position resulting from the movement of the A465 will exhibit a minimum error of ± 0.050 mm. This error cannot be removed. It is desirable to produce relative measurements that have a resolution that is an order of magnitude greater than this repeatability value in order to be able to observe the effects of the robot repeatability and to attempt to accurately calibrate the kinematic model of this robot. Using relative measurements with a high resolution results in an increase in the confidence that any measured deviations between images are mostly a result of contributions from the robot repeatability and error in the robot's kinematic model and not measurement error.

In [1], the repeatability of the A465 manipulator is further characterized using a camera-based calibration system. The result of this characterization is that the value ± 0.050 mm stated by the manufacturer as the repeatability of the manipulator is considered a generous estimate. The actual repeatability of the Thermo CRS A465 is determined to be ± 0.069 mm. The difference between these two estimates will affect the requirements of the calibration system.

2.1.2 Calibration Equipment

The equipment required for this calibration system includes all components used to facilitate the acquisition, processing and application of image data for the purpose of calibrating a robotic manipulator. A cost analysis describing the selection of actual components is presented in Appendix A. As a result of selecting the specific components outlined in Table A.7, several limitations are imposed on the system. In the following paragraphs, a brief introduction to several of these components and their relevant characteristics is presented.

The measurement head is a grouping of components consisting of the camera, lens, illumination, mounting structure and appropriate power/data cabling. This system can be viewed in Figure 2.2.

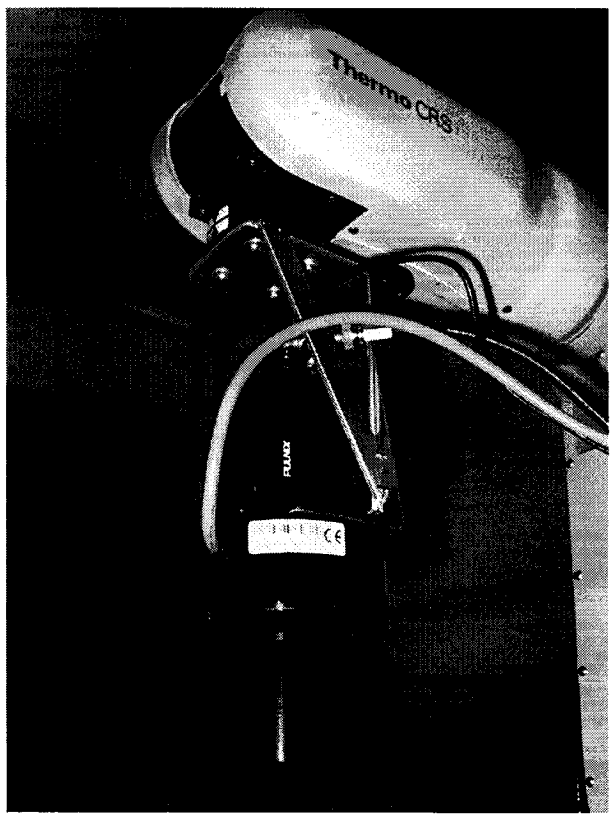

Figure 2.2: Calibration measurement head assembled to the Thermo CRS A456 Robot.

This camera-based calibration system captures digital images using the Pulnix TM-200. This camera is referred to as an analog camera since the image captured within the camera is transferred to a data acquisition card using a modulated analog electrical signal, as opposed to a digital signal. The image is then digitized using the data acquisition card. This camera has horizontal and vertical resolutions of 494 and 768 pixels, respectively, but is limited to a resolution of 480×640 pixels based on the National Instruments PCI-1409 Image Acquisition Card, also known as a frame-grabber card. The active sensing area on the CCD chip is given as 4.8×6.4 mm^2.

Mounted to the camera through a C-mount interface is a Rodenstock Macro 1X magnification lens. The working distance for this lens is given as 90 mm. This implies that the image focused onto the surface of the detector of the camera corresponds to an object situated 90 mm from the outer surface of the lens along its optical axis. The depth of field for this lens is ± 0.3 mm.

The camera and lens are mounted to the robot using the stainless steel structure visible in Figure 2.2. This structure was specifically designed to integrate the calibration hardware with the robot end-effector. A description of this design process is included in Appendix B.

All measurements are performed through the extraction, processing and comparison of images depicting the measurement artifact visible in Figure 2.3. The artifact in question is the PZA stainless steel ruled surface with graduations at 1 mm intervals based on the DIN 685 standard. The surface graduations appear in three lengths. The longest graduations are 10 mm in length and appear at 10 mm increments along the ruler. The second longest graduations are 5 mm in length and indicate half of the distance between each large graduation, 5 mm. The smallest graduations are 3.8 mm in length and appear every millimeter. The accuracy on these dimensions is given as ± 0.002 mm. The graduations, as viewed by the camera using red LED illumination, appear dark in contrast to the

stainless steel surface of the ruler.

Figure 2.3: PZA precision-machined stainless steel ruled surface.

The LabView data acquisition program is used to capture the images and store them on the hard drive of the computer. All processing of images and data is performed in the MATLAB environment using custom developed high-level image processing software and pre-packaged MATLAB library functions. These programs are implemented using a standard personal computer.

The calibration and validation of results is performed using the components described above, excluding the A465 robotic manipulator, and including the Mitutoyo Vernier X-Y Table $0 - 2$ inches, with a resolution of 0.0002 inches.

2.2 System Requirements

The repeatability of the Thermo CRS A465 manipulator is determined to be ± 0.069 mm. A system that is designed around this requirement is able to remain functional when applied to systems with larger suggested repeatability values. The significance of robot repeatability in kinematic calibration has been described in detail [29]. In general, it is

understood that the precision of a manipulator can be improved up to its repeatability [28]. Any improvement beyond this mark is masked by random positional error and is difficult to compensate for through alteration of the kinematic model parameters alone. This repeatability is a function of many non-linear parameters including the temperature of the robot, loading and friction in the robot joints. As a requirement of this calibration system, the value of ± 0.007 mm is established as the maximum possible error that any relative measurement it produces may contain.

The ability of vision-based systems to produce measurements to within sub-pixel accuracy is also well documented [30, 31, 32]. It can be noted that this accuracy is not always easy to achieve. Images that contain sharp, contrasting features are more likely to result in measurements with a higher degree of accuracy. Two images with varying degrees of contrast can be seen in Figure 2.4. On the left side of this figure sits an image of the custom made calibration artifact used to produce the repeatability results discussed in Section 2.1.1. This image is characterized by the sharp contrast between the surface of the artifact and the black paint used to fill in the set of intersecting grooves on its surface. The image on the right side of Figure 2.4 is that of the precision-machined ruled surface that is used for the purpose of this calibration method. The features in this image consist of the

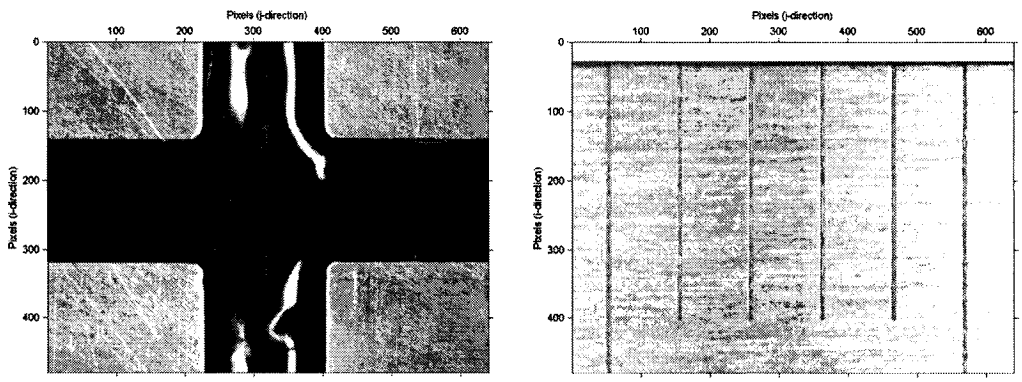

Figure 2.4: Two images captured with calibration equipment with varying degrees of contrast.

horizontal edge of the ruler and the vertical graduations. The feature with the sharpest contrast in this image is the horizontal edge. This contrast results from difference in the intensity of pixels viewing an area located on the surface and off of the surface of the artifact. Several vertical graduations are machined onto the surface of the ruler, but there is a lack in the difference of coloration between the surface of the artifact and the bottom of these machined graduations. This lack of any drastic colour change results in a small contrast between these features and an increase in the likelihood that sub-pixel accuracy can not be achieved. In spite of this limited amount of contrast, a soft requirement is implemented in order to attempt to achieve sub-pixel accuracy in the measurements extracted from the images of the artifact. In the case of this calibration system where each pixel represents an approximate area of 0.0084×0.0098 mm^2, sub-pixel accuracy refers to any measurement achieving an accuracy of less than ± 0.005 mm.

Based on some preliminary experimentation with the Thermo CRS A465 manipulator, it is expected that the maximum positional deviation of the robot end-effector in the $X - Y$ plane of the robot coordinate system will be less than 0.7 mm in the X direction and 0.4 mm in the Y direction. This expectation results in the conservative requirement that the camera-based calibration system be able to measure the displacement of the robot end-effector over a displacement range of at least 0.8 mm in the X direction and 0.5 mm in the Y direction.

The general definition of the depth of field for an optical lens is the range of distance in front of and behind the object that is the focus of the image wherein features will appear suitably sharp. Figure 2.5 illustrates this definition. Features that are not in this distance range appear increasingly blurry with increasing distance from the object plane. The depth of field for the Pulnix TM-200 camera is given as ± 0.3 mm. This characteristic sets a limitation on the range of displacement along the optical axis over which the system can operate. As the robot positions the camera to view the ruled surface, any displacement

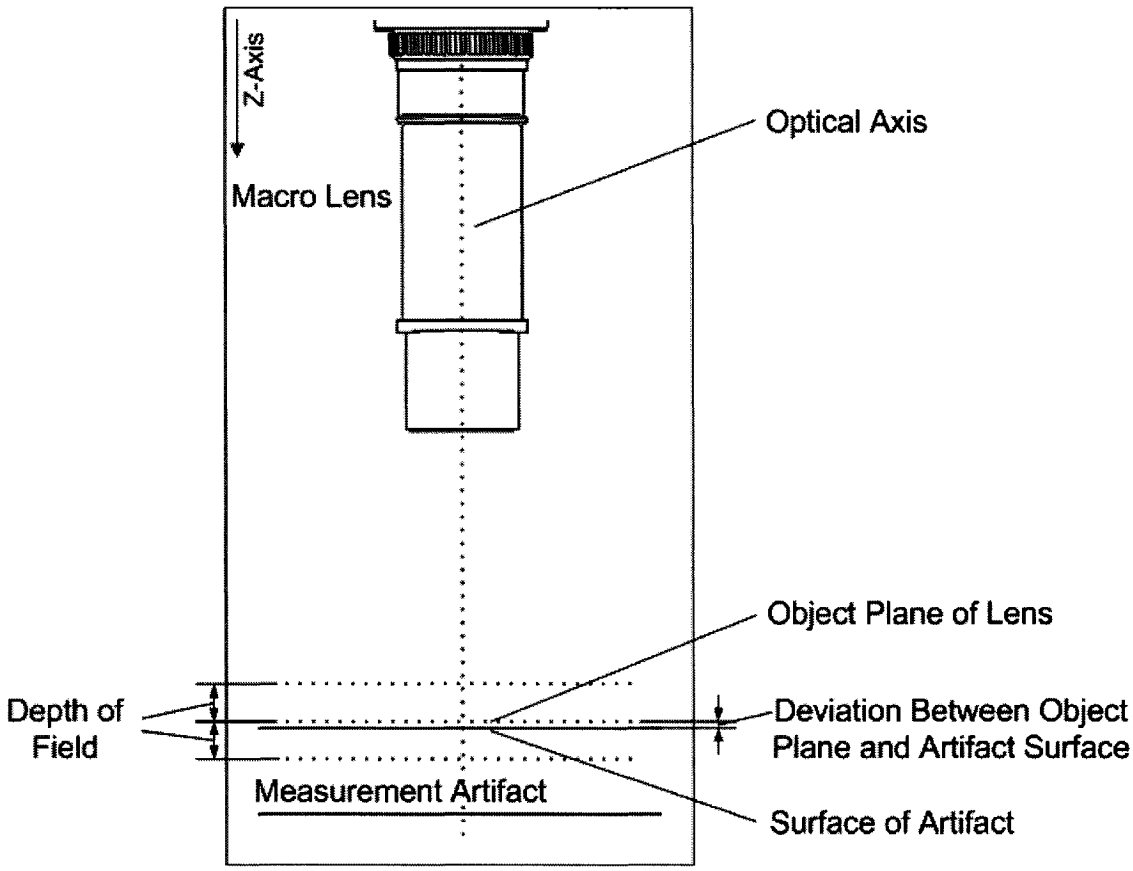

Figure 2.5: Artifact/lens assembly illustrating depth of field.

between the object plane of the camera and the surface of the artifact larger than 0.3 mm will facilitate blur in the resulting image. For displacements near the 0.3 mm mark, this blur may not adversely affect the resulting measurements, but may act as a sort of noise filter. Larger displacements will result in the distortion of image data to the point that accurate relative measurements can no longer be produced. The limitation is placed on the system that ± 0.3 mm is the largest possible deviation between the object plane of the lens and the surface of the ruler for which measurements can be extracted. This phenomenon is discussed further in Chapter 4.

Each relative measurement requires the comparison of two images. These images are captured both before and after a robot motion consisting of a 1 cm displacement in the robot end-effector along the length of the ruler. These two images should appear identical

based on the geometry of the ruled surface, however, they do not. The difference in these two images is a measure of the $X - Y$ positional error. The extraction of displacements in the X direction of the world coordinate system is limited by the position of the horizontal edge of the ruled surface within the image captured before the robot is displaced. If the robot positional error results in the disappearance of this edge in any subsequent image then the X-displacement between these images cannot be measured. This places a limitation on the displacement in the X direction over which a measurement can be taken. The initial position of the horizontal edge in any image set is to 80 pixels from the j axis of the image. This initial position is illustrated in Figure 2.6. It corresponds to a viewable distance of approximately 0.8 mm above the horizontal edge. From this position, an edge displacement of up to 0.8 mm in the $+X$ direction can be extracted from subsequent images. A displacement in the $-X$ direction will result in the horizontal edge positioned below its initial position in subsequent images. A displacement of up to 5.6 mm in the $-X$ direction may be observed.

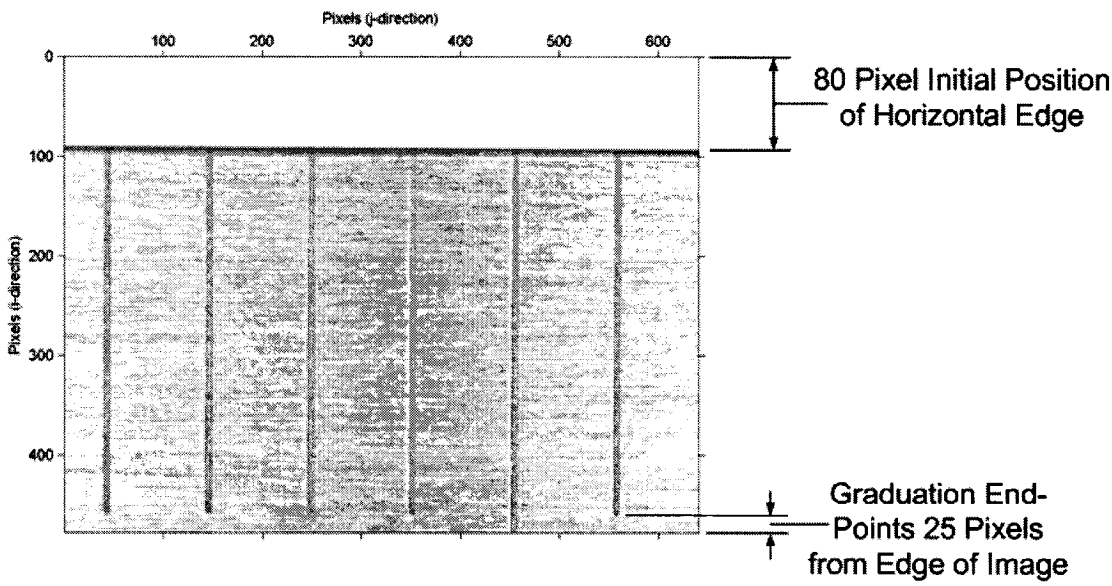

Figure 2.6: Initial position of the horizontal edge of the ruler in an image.

It can be noted that the initial position of the horizontal edge affects the location of the graduation end-points in any image. Given the 80 pixel initial displacement of the horizontal edge of the ruler from the top of the image, the end-points of each graduation are located a distance of approximately 25 pixels from the bottom of the image. A robot displacement of more than 0.25 mm in the $-X$ direction will remove these features from the image and prevent them from being referenced in further calculations. These end-point features are required by the image processing algorithm in order to remove perspective distortion from the images. This concept is further discussed in Section 3.5.1. Since the maximum expected displacement of the robot end-effector in the X direction exceeds 0.25 mm, these features may not appear on any post-motion images. The development of an algorithm that does not require these features for the extraction of measurements from images must be developed. The availability of these graduation end-points for processing allows the algorithm to distinguish between the short and long graduations appearing in each image. These longer graduations are positioned every 5 mm along the length of the ruler and can be used as a reference graduation for the Y displacement. Using these reference graduations, the system should be able to extract measurements up to ± 2.5 mm in the Y direction.

Table 2.1: Design requirements for the camera-based calibration system.

Requirement Name	Value
Measurement Error (Hard Requirement)	± 0.007 mm
Measurement Error (Soft Requirement)	± 0.005 mm
Minimum Required ΔX (Hard Requirement)	± 0.7 mm
Minimum Required ΔY (Hard Requirement)	± 0.4 mm
Maximum Available ΔX (Hard Requirement)	± 0.8 mm
Maximum Available ΔY (Hard Requirement)	± 0.5 mm
Maximum Available ΔZ (Soft Requirement)	± 0.3 mm

A summary of these requirements can be viewed in Table 2.1. Several of these requirements are represented in Figure 2.7 as a three-dimensional boundary. This boundary is a function of the characteristics that define each component of the system. Using the appropriate image processing algorithm, the system should be able to extract relative measurements referencing the central location of this boundary to any other point within its limits. Given the requirement that the system produce measurements of at least 0.7 mm in the X direction and 0.4 mm in the Y direction, this system should be able to satisfy the requirements. The robot displacement in the Z direction is expected to exceed the ± 0.3 mm depth of field of the lens, but is not expected to adversely affect the resulting relative measurements. This phenomenon is further discussed in Section 4.3.

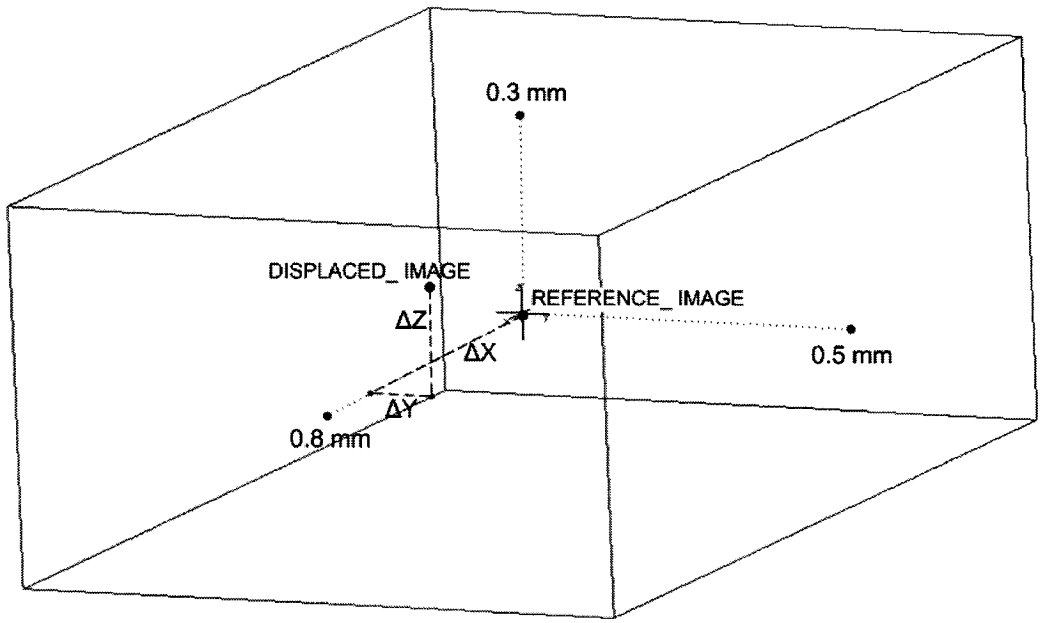

Figure 2.7: Volumetric region defined by the requirements over which relative measurements can be extracted.

Chapter 3

Digital Image Processing

As previously described, many sets of measurements are required in order for the relative measurement concept to be properly implemented. There are a myriad of ways to produce such measurements. Coordinate measuring machines (CCM), lasers, and digital cameras are three examples of such devices. The CCM is a large and expensive machine that will provide, very accurately, the absolute position of a robot end-effector anywhere within the workspace of the machine. When using such a device, it is most likely that the robot under investigation be transported to the CCM as a result of the large weight of this device and the required volume. There are several laser systems that have been developed for extracting the position of a robot end-effector. These systems increase in cost as the required resolution of such measurements increases. Since one of the requirements of the calibration system under development is that the cost of such a system remain relatively low, a digital camera system is used to produce the desired result. This alternative is both low cost and easily portable into the workspace of most robotic manipulators. One possible disadvantage of a camera system is the requirement to develop algorithms to process the resulting images and to extract the desired accurate metric information. This development of image processing algorithms is the focus of this thesis and is described

throughout Chapter 3. The refining of several steps within the algorithm is described in Chapter 4.

3.1 Algorithm Design Requirements

The calibration system should provide measurements that are as accurate as possible. There are several requirements that must be met in order for the algorithm to be considered successful. These requirements are limitations imposed by the hardware used to acquire the images and by the robot that is to be calibrated.

The robot used here is a Thermo CRS A465. As stated in Section 2.1.1, the Thermo CRS A465 is able to achieve a repeatability of ± 0.069 mm. Since ± 0.069 mm of positional deviation can be expected on any measurement as a result of the manipulator, it is required that the algorithm produce measurements that are at least an order of magnitude better than this deviation value.

A calibration system would benefit by being readily adaptable to other robots. Such robots may have repeatability values that are greater or less than that of the A465. In order to increase the number of manipulators to which this system can be applied, it is desirable to increase the resolution of the measurements by decreasing the measurement error as much as possible. There are several image processing algorithms that produce results to a sub-pixel accuracy [30, 31]. These algorithms are limited in resolution by noise and other unwanted image characteristics. Based on the geometry of the measurement head that has been designed, the approximate area viewed from each pixel on the CCD camera is about 0.01 mm^2 on the surface of the measurement artifact. In order to achieve sub-pixel accuracy, the measurement system must produce measurements with an error no greater than ± 0.005 mm. The ability of a system to produce sub-pixel accuracy is limited by several factors including noise, surface irregularities and contrast. These factors will be

discussed in greater detail in Section 3.3.

There are several measurement systems that place a requirement on the amount of time in which a measurement must be extracted. Such systems usually involve measurements to be taken while a body is in motion. The relative measurement concept does not require any measurement to be taken during motion. As a result, there is no hard requirement placed on the duration of the image processing algorithm. As a general guideline, any steps that improve the speed of the algorithm without decreasing the accuracy of the results will be implemented.

3.2 Preprocessing of Digital Images

Image preprocessing takes place before the capture of the digital image. There are several settings that can be adjusted in order maximize the quality of the images to be captured. The CCD charge accumulation type and Analog-to-digital conversion factor are two such parameters and are discussed in the following sections.

3.2.1 Charge Accumulation Type

The charge accumulation type describes the process of determining the intensity value of each pixel across the area of a CCD array. The Pulnix TM-200, known as an interlaced camera, contains a CCD array with two interlaced groupings of pixels as denoted in Figure 3.1. Each of the two fields is read separately from the array and later combined. The electronics inside the camera must be configured in order to determine the method by which these two fields are used to produce a resulting image. There are two standard methods of charge accumulation available on the Pulnix TM-200 CCD camera: field integration and frame integration. These methods are described in the following sections.

Field Integration

Field integration, as depicted in Figure 3.2(a), is a process that requires the value of adjacent pixels from each field to be integrated together, resulting in an approximation of the average of the two pixels. By combining the two fields in this way, the resulting image will exhibit a reduction in the blur of any moving object being captured by the CCD. The odd and even fields can then be displayed sequentially in order to speed up the frame rate of the system. Consequently, the vertical resolution of the resulting images is reduced.

Frame Integration

Frame integration, as depicted in Figure 3.2(b), is a process of integrating each of the two fields separately and then combining the even and odd fields to produce an image of higher resolution. The duration of this process is almost twice that of the field integration ($\frac{1}{30}$ sec compared to $\frac{1}{60}$ sec), but is not an issue for a system where time is not a critical requirement.

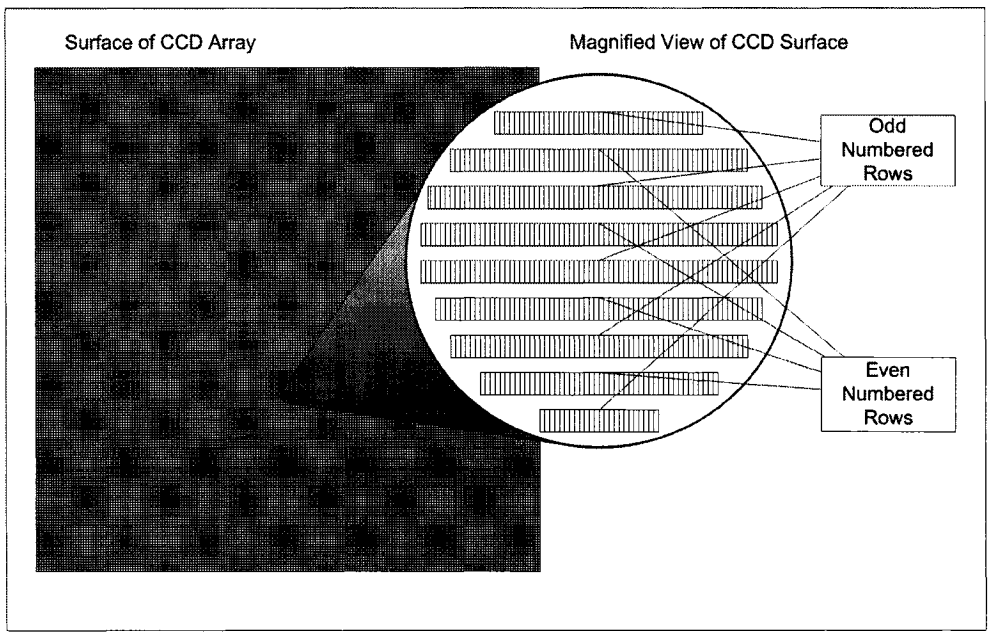

Figure 3.1: Surface of a CCD chip showing two interlaced groupings of pixels.

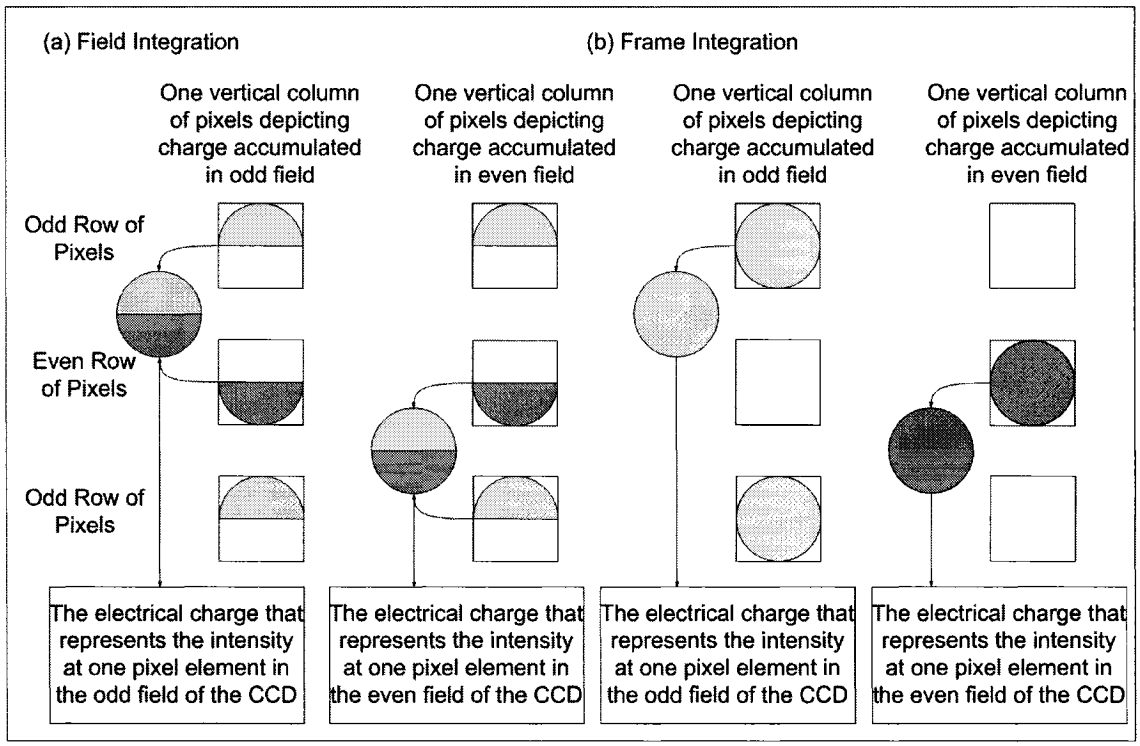

Figure 3.2: Two available types of charge accumulation: (a) field integration and (b) frame integration.

Comparison of Charge Accumulation Types

Figure 3.3 compares two sets of sequential images taken using both the field integration mode and the frame integration mode. The object being imaged is the ruled surface from which the metric information is to be extracted in the subsequent algorithm. Both sets of images are captured without any relative motion between the ruler and camera and so one expects that each set should appear identical.

Using these images, one can observe that images captured using the field integration mode and taken at subsequent time intervals can display a displacement in the location of the horizontal edge. In Figure 3.3(a), the horizontal edge appears to be located 5 or 6 pixels from the top of the image on the left side of the figure. On the right side of this figure, the location of the edge appears to be definitively located 6 pixels from the top of the image because the fifth row of pixels have faded in intensity. The displacement between

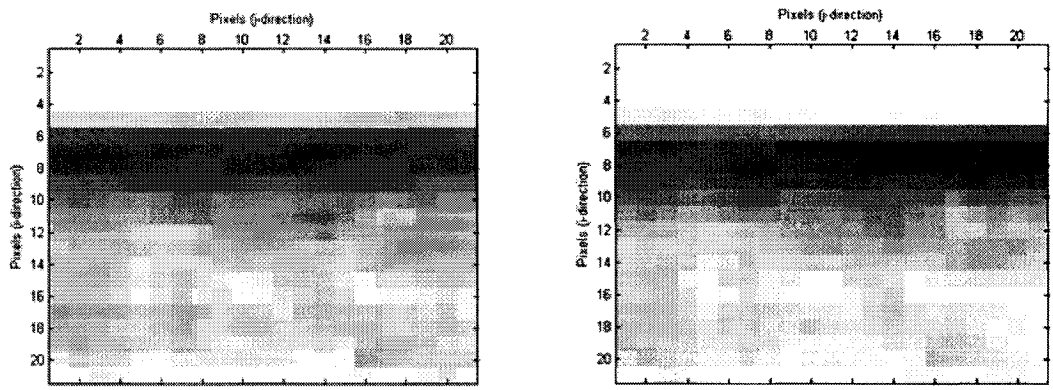

(a) Two images captured using field integration mode

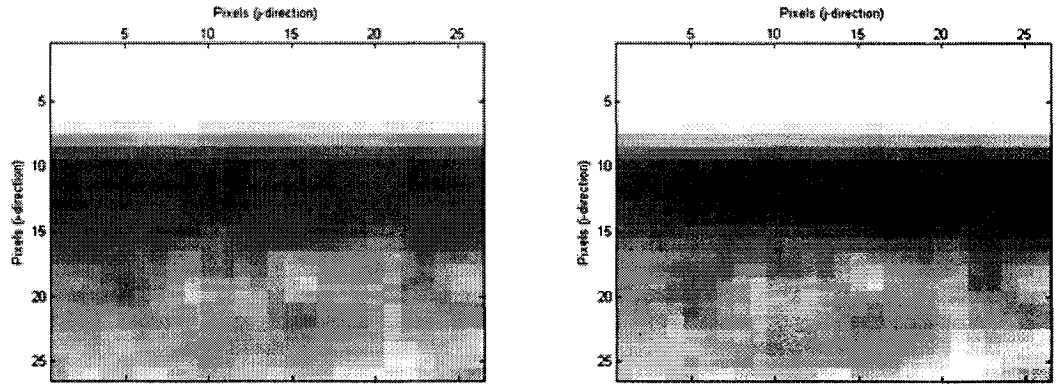

(b) Two images captured using frame integration mode

Figure 3.3: Comparison between sets of images captured using field and frame integration.

these two images is known as pixel jitter. It is the result of poor synchronization between the CCD camera and the framegrabber card and the use of alternating fields of pixels. The observed displacement may result in a 1 pixel change in the location of the edge. Field integration mode reduces the resolution of the image to 1/2 the resolution obtained using frame integration mode, so instead of each pixel-width representing 0.01 mm, each pixel now represents 0.02 mm. A 1 pixel displacement will result in a possible deviation of greater than 0.02 mm and will significantly affect the resulting measurements.

By comparison, the images captured using the frame integration mode displayed in Figure 3.3(b) are approximately identical. These images offer a higher resolution and are

not subject to pixel-jitter. As a result, frame integration mode is chosen to be the charge accumulation type for this system.

3.2.2 Pixel Conversion Factor

The Pulnix TM-200 camera is capable of producing images with an 8-bit resolution on the intensity of each pixel. This resolution refers to the intensity of each pixel across the image array being represented by one 8-bit binary number. There are $2^8 = 256$ different 8-bit binary numbers and so each pixel intensity (PI) will be represented by one of 256 discreet values of intensity between 0 and 1, where the value 0 is associated with absolute black and the value 1 is associated with white. The *Conversion Factor* for the CCD pixels refers to the mapping between the voltage they produce in the presence of light and the resulting digital representation of this intensity in the image. The magnitude of these voltages varies based on the intensity of light reaching each pixel on the surface of the CCD chip. The conversion factor controls the minimum amount of light required to produce a pixel intensity greater than the value 0, as well as the maximum amount of light resulting in a pixel intensity valued less than 1. By adjusting the *Conversion Factor*, one adjusts the resolution of the pixel intensities in order to fill the resulting image with as much salient information as possible. This process may also work to suppress noise within the image data. The lower and upper limits of the conversion range are each represented by a value between 0 V and 1.4 V and are adjusted using the framegrabber software. The resulting resolution of pixel-intensities (RP) can be calculated using Equation 3.1.

$$RP = \frac{Intensity\ Levels(IL)}{Voltage\ Range} = \frac{256}{max.\ voltage - min.\ voltage}. \tag{3.1}$$

Figure 3.4 shows a comparison of several different ranges used in the conversion from *voltage* to digital representation. The first column in this figure depicts the range of

voltage that is used by the system. Each pixel on the CCD is able to produce a voltage signal between 0 V and 1.4 V, although this entire range is not required by the system. By limiting the range observed by the CCD, the resolution of pixel intensity is increased. Using this applied range, all voltages above the maximum voltage limit will result in an intensity value of 255 and all voltages below the minimum voltage limit will result in an intensity value of 0. The representation of this mapping, illustrated in Figure 3.4, uses a controlled range within the minimum and maximum possible voltage values for conversion, 0 V and 1.4 V respectively. The minimum and maximum limitations used in each trial are indicated by the arrows directly on the right side of the column. Also included in this column is the calculated *RP* for each trial. The second column of Figure 3.4 shows the resulting images from the use of each particular *Conversion Factor*. The third column contains a set of graphs showing the intensity of pixels along one diagonal of the image. This graph is used to observe the general concentration of the pixel-intensities in the image.

In the first trial, the gain values were set to the minimum and maximum allowable values. The 8-bit range of the camera is essentially stretched to cover a large range of observable levels of light. As a result, the levels of light that are projected from the object only cover a small portion of this range. This concentration of intensities can be observed in the graph of pixel-intensities in the third column of Figure 3.4. The features in the image exhibit very little contrast from the surface of the measurement artifact. The image, itself, appears dark in colour because the concentration of pixel intensities remains in the darker portion of the spectrum.

In the second and third trials, either the maximum or minimum gain levels are adjusted in order to coincide with the the upper or lower values of the pixel-concentration described in trial 1. In each of these trials, the resulting images display more detail than the image of trial 1 because the actual range of light levels that can be captured by the CCD is reduced. This reduction allows greater resolution in the intensity of each pixel. Since the

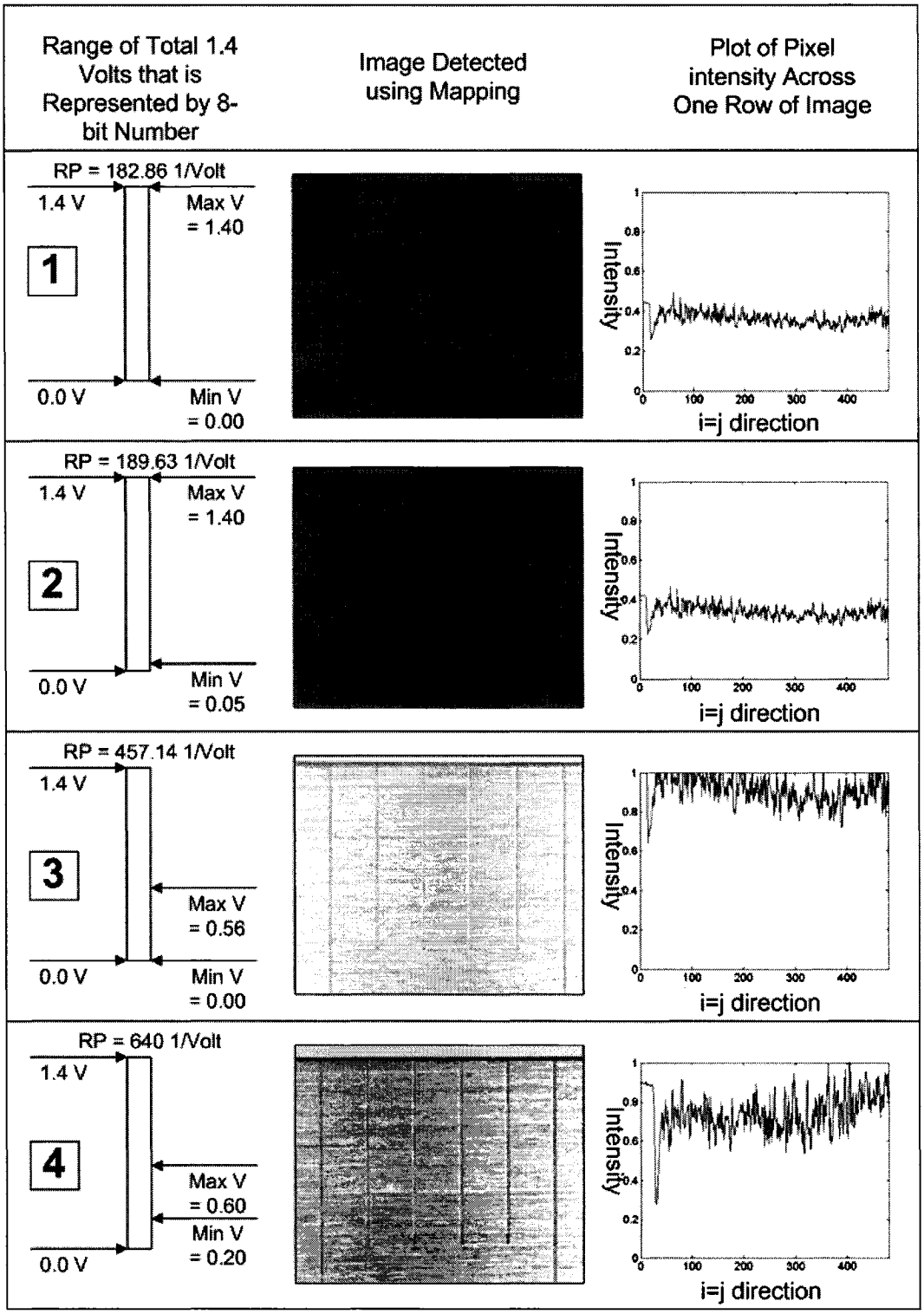

Figure 3.4: Comparison of several analog to digital conversion factors.

range of gain values used in these two trials is centered either below or above the actual concentration of light levels from the object, the resulting image appears lighter or darker than necessary. The data in the fourth trial illustrates the clipping of image data greater than the value 1. The high levels of intensity that are clipped in this trial correspond to the reflection of light off of the surface of the measurement artifact. These high-intensity pixels do not contain metric data that is required for producing relative measurements.

For the fourth trial, both the upper and the lower gain values are adjusted in such a way that the range of intensity values captured by the CCD array correspond to those levels of light that are most prominent from the surface of the ruler being imaged. This configuration provides the best resolution of pixel-intensities visible in the figure. The graph for this trial displays the range of intensities that are used. It can be noted that the range of pixel concentration for this trial covers a larger portion of the 8-bit range.

3.3 Processing of Digital Images

The processing of digital images encompasses the procedure that is used to extract relevant pixel coordinates from each digital image and format these coordinates into a set of data that can be readily manipulated. These coordinates contain metric information regarding the position of the robot end-effector with respect to the measurement artifact and are used in subsequent steps to produce relative measurements. The format that has been selected for this data output is a set of linear equations representing all edges in the image. This output consists of both horizontal and vertical edges. For the horizontal edges, the $Slope/i - Intercept$ [1] representation is implemented. This representation indicates the slope of the line as the change in pixels in the j direction for every unit pixel change in the i direction along the line. The intercept indicates the position in the j direction at which this line crosses the j axis. In order to avoid issues involving infinite slope, the vertical

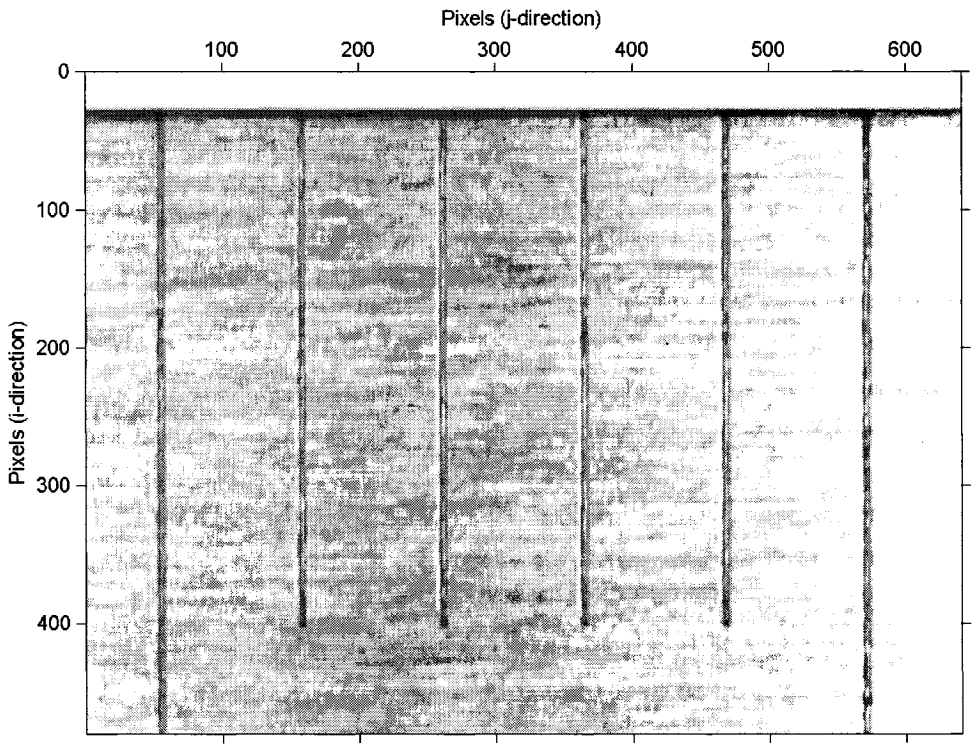

Figure 3.5: Typical image captured by the calibration system to be processed using digital image processing.

lines are represented in the $Slope/j - Intercept$ [1] form. An example of a typical image is displayed in Figure 3.5. The complete extraction of data from this image requires the application of several distinct algorithms. A representation of the overall algorithm can be viewed in Figure 3.6. Each step of the algorithm will be described in subsequent sections.

3.3.1 Image Representation

Each digital image is read into a software environment. Within this environment, any number of algorithms can be developed and applied to the image in order to refine the data contained within. The software package selected for the purpose of processing these images is MATLAB version 6. This package, as well as being familiar to the developer and

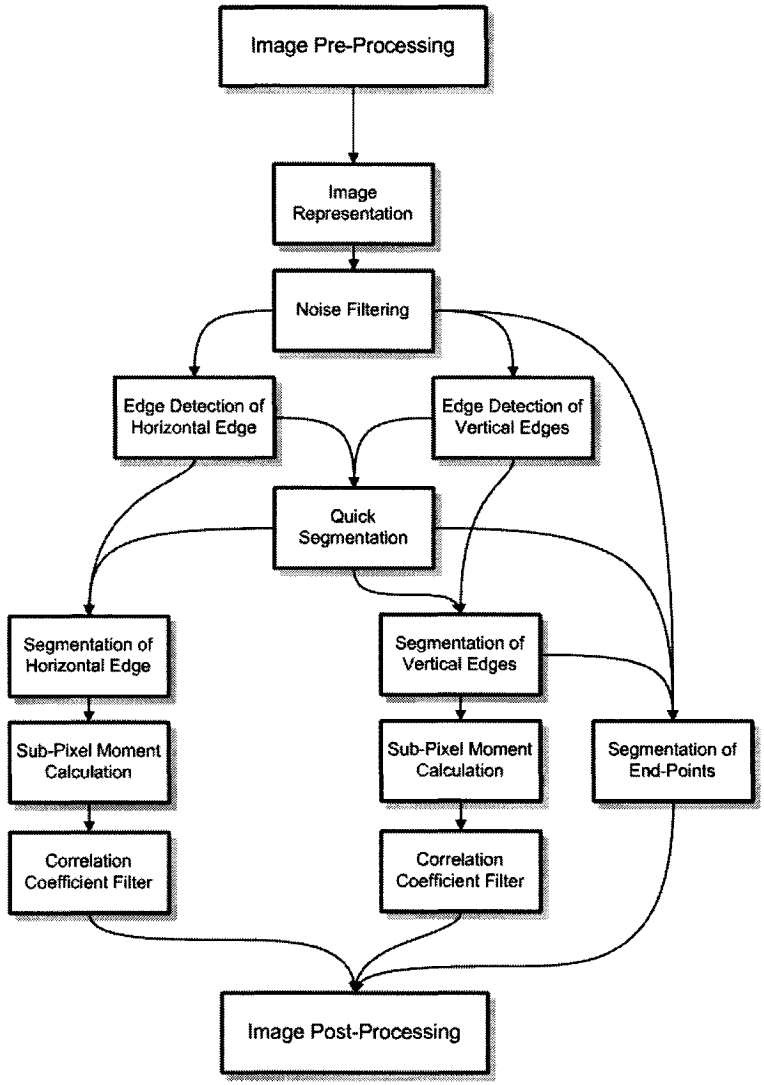

Figure 3.6: Digital image processing algorithm.

readily available, contains many useful high-level mathematical functions that are easily applicable to the manipulation of image data.

The Image Representation algorithm is used to read digital images into the MATLAB environment and represent the image data as an $m \times n$ matrix of pixel intensities, where m and n are the height and width of the image in question. Figure 3.7 shows a comparison between a small portion of one digital image and the representation of this same image within the MATLAB environment. Each element in the matrix is a value between 0 and 1.

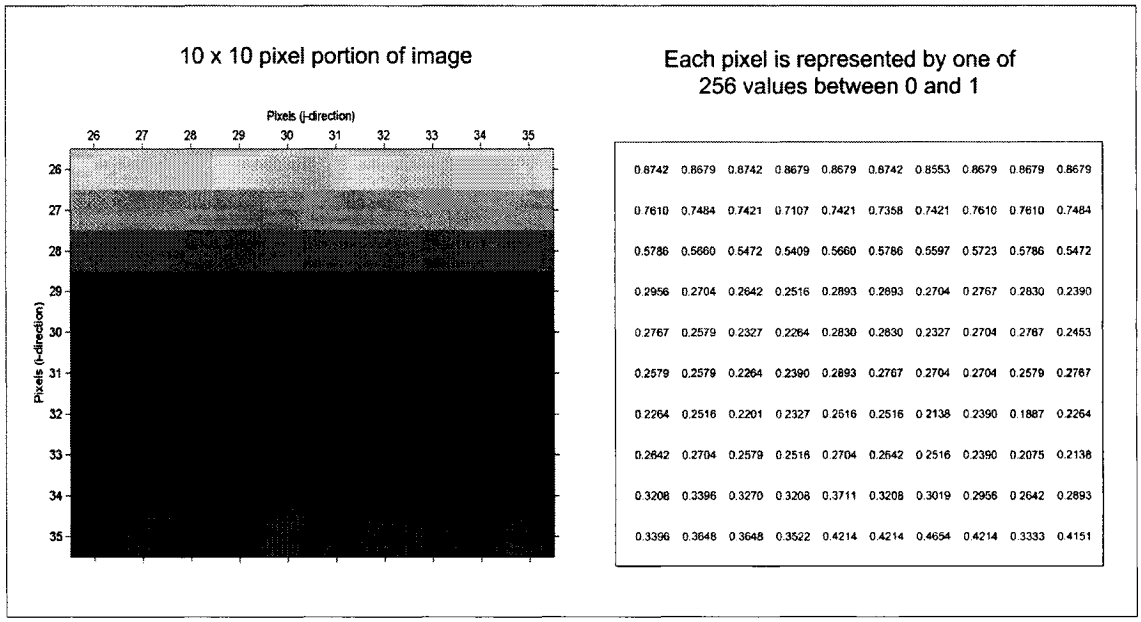

Figure 3.7: Comparison between a typical JPEG image and its representation in the MATLAB environment.

Since these values are taken directly from the image, there are 256 possible values that can be observed. Each value represents one shade of gray within the image. The 2-dimensional matrix representation of the image allows the developer to make use of MATLAB's large library of matrix operations. This representation also allows computations to be performed on the entire matrix, as opposed to operations occurring element by element, which results in a significant reduction in process duration.

3.3.2 Noise Filtering

The image data contains at least two types of noise to various degrees which are inherent in digital CCD cameras. Salt and pepper noise is the random inclusion of peaks and valleys across the image data. These peaks and valleys appear as a distribution of lighter and darker pixels which can skew calculations involving pixel intensities. Gaussian noise affects the intensities of pixels in a manor proportional to the Gaussian distribution. Noise of this nature is less likely to result in a pixel intensity within the neighborhood of the

intensities of its surrounding pixels [26].

The camera that is used in our calibration system provides a signal to noise ratio of greater than 50 dB. It is probable that this ratio is large enough to minimize the affects of electrical noise on the metric data extracted from the images to the point that these affects are considered negligible. However, there are many features visible in each image that work to convolute the image data in a manner similar to noise. One such feature is the surface finish of the measurement artifact. This artifact was machined in such a way that the metal grain on the surface is a prominent feature in the images. Another feature affecting the image data is the inclusion of reflected light from the surface of the artifact. The reflected light provides sharp peaks in pixel intensity when travelling from many of the small reflective areas located in the grain and near each graduation. The use of certain noise filters may reduce the affect that these features have on the metric image data. The application of several distinct noise filters in the form of convolution masks [33] is described in the following paragraphs.

A convolution mask is an $m \times n$ dimensional window that is centred on each element in the image data matrix. The elements in the mask can be weighted, as in the Gaussian filter, or not, as in the Mean filter [26]. The elements in the mask are then combined with the corresponding elements in the image data matrix to produce a weighted or non-weighted sum of the image data which represents the value of the filtered data pixel at that location in the matrix. The calculation of this convolution is the dot product of the elements in the convolution mask with the corresponding elements in the image data divided by the number of elements in the mask. The implementation of this filter is illustrated in Figure 3.8.

The Mean filter implemented in this thesis is a 3×3 matrix with all elements equal to a value of one.

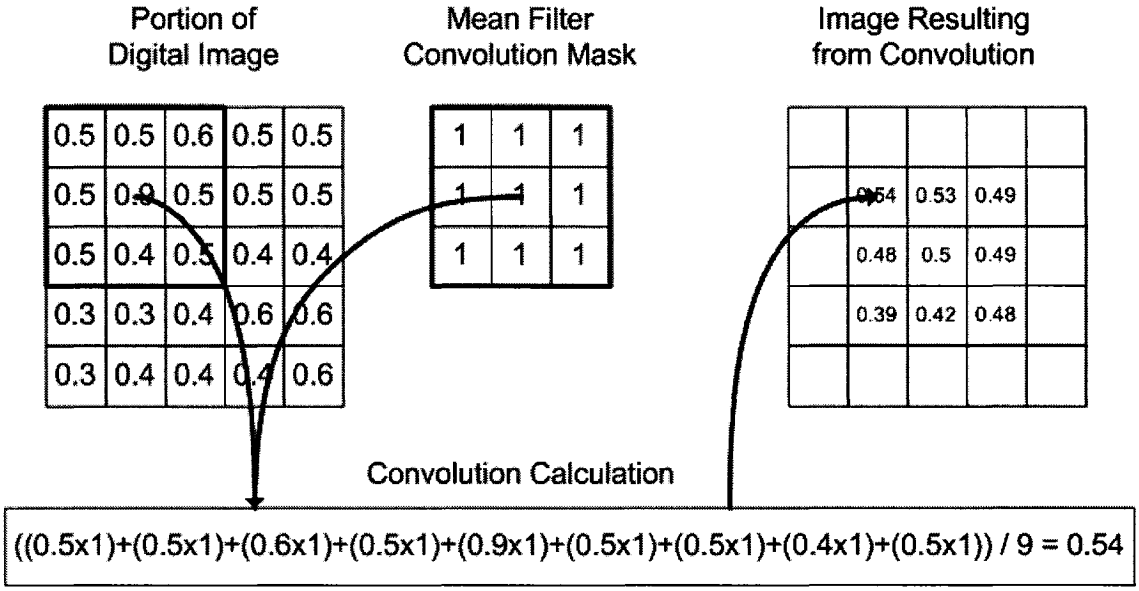

Figure 3.8: Typical convolution operation using the Mean Filter.

$$\text{Mean Convolution Mask} = \begin{bmatrix} 1 & 1 & 1 \\ 1 & 1 & 1 \\ 1 & 1 & 1 \end{bmatrix}. \tag{3.2}$$

This mask sets the value of each element in the data matrix equal to the mean value of its surrounding pixels. The benefit of implementing this filter is that local peaks and valleys in pixel intensity caused by noise will be reduced. One possible problem resulting from the use of this filter is the smoothing of transitions required to locate the position of edges. With the decrease in contrast at an edge location, the accuracy in the detection of the edge may be reduced.

The Gaussian filter implemented in this thesis is a 7×7 Gaussian mask [26] with elements chosen from the two-dimensional zero-mean Gaussian distribution visible in Equation 3.3. A typical convolution mask described by this distribution is used in the development of this algorithm. The benefits of this filter are similar to those of the Mean filter, but the Gaussian filter is suited to filtering out noise with a random distribution of

intensities. The implementation of this filter is similar to that illustrated in Figure 3.8. The differences between these particular filters are the size of the image area considered by each mask and the distribution of the mask elements.

$$g[i,j] = ce^{-\frac{i^2+j^2}{2\sigma^2}}, \tag{3.3}$$

$$\text{Gaussian Convolution Mask} = \begin{bmatrix} 1 & 1 & 2 & 2 & 2 & 1 & 1 \\ 1 & 2 & 2 & 4 & 2 & 2 & 1 \\ 2 & 2 & 4 & 8 & 4 & 2 & 2 \\ 2 & 4 & 8 & 16 & 8 & 4 & 2 \\ 2 & 2 & 4 & 8 & 4 & 2 & 2 \\ 1 & 2 & 2 & 4 & 2 & 2 & 1 \\ 1 & 1 & 2 & 2 & 2 & 1 & 1 \end{bmatrix}. \tag{3.4}$$

A median filter [26] is also used to suppress noise. In image processing, this filter is represented using an $m \times n$ window that defines the neighbourhood around any given pixel. This window is centred on a pixel and the resulting intensity is given as the median intensity located within the neighborhood. This filter works optimally when the distribution of noise on the levels of intensity is centred on the desired intensity.

It can be noted that the surface of the measurement artifact does not appear smooth in texture. This surface exhibits a grainy texture and it appears that the grains have a directional tendency to be oriented in the j direction of the image coordinate system. The direction of these grains and their prominent intensity in certain images suggest that the inclusion of these grains may hinder the extraction of low contrast vertical edges. It is desirable that the effects of these grains be reduced through the use of a filter. In the previous paragraphs, an explanation is presented for the mean filter. This filter is nominally sized in order to provide equal weight in both the i and j directions. Using

the same concept as the mean filter, one can design filters with directional bias in order to suppress features with directional tendencies. An example of one of these directional filters is represented using a convolution mask in Equation 3.5. This filter is a 5×1 convolution mask that is applied to an area of 5×1 pixels in the image. It can be noted that the typical width of one grain in an image is roughly five to ten pixels. The use of this filter should work to suppress these horizontal grains, but not blur the vertical location of vertical graduations.

$$\text{Directional Convolution Mask} = \begin{bmatrix} 1 \\ 1 \\ 1 \\ 1 \\ 1 \end{bmatrix}. \tag{3.5}$$

The partial processing of one image using *Mean*, *Gaussian*, *Median* and *Directional* filtering can be viewed in Figure 3.9. A further comparison between these filters is presented in Section 4.2.1.

3.3.3 Edge Detection

After filtering, the image contains data with most of the noise-related spikes in pixel intensity removed. The next step of the processing is the accentuation of possible edge pixels through the use of an edge detection operator. An edge detection operator is another type of convolution mask with its elements weighted in such a way that the weighted sum of the elements in the data matrix produce larger intensities in the proximity of sharp transitions between adjacent pixels. The elements of these convolution masks can be weighted in such a way as to accentuate pixels containing horizontal or vertical edges with transitions from high to low or low to high intensity. The edge detection mask implemented

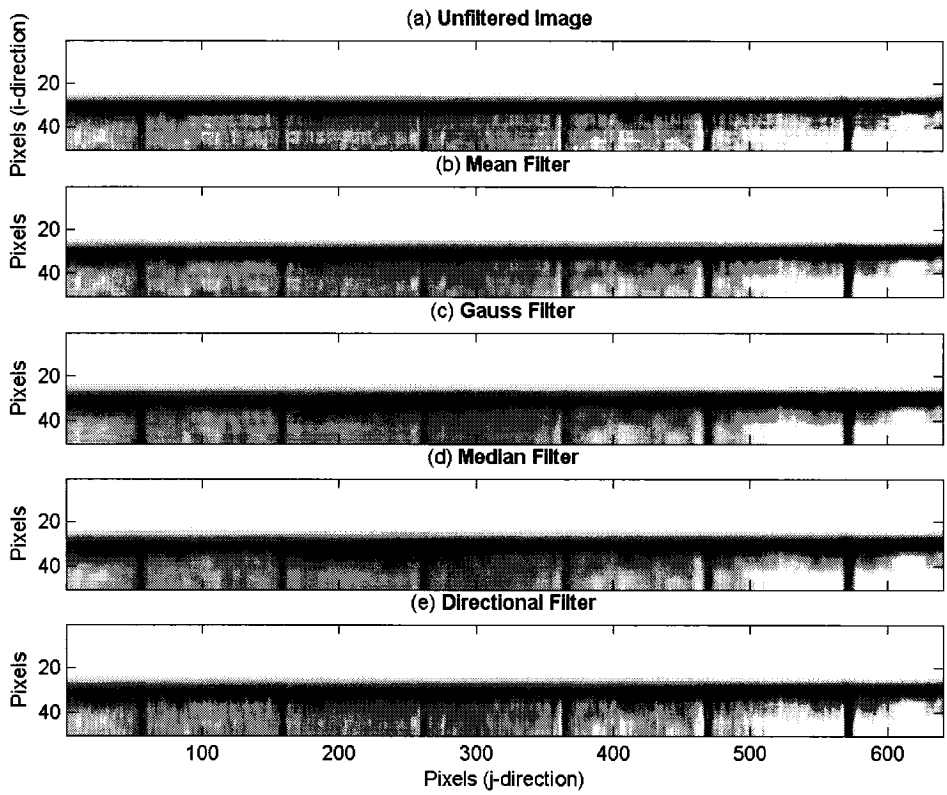

Figure 3.9: Comparison between a raw image, a mean-filtered image, gauss-filtered image, median-filtered image and an image filtered with a directional bias.

in this algorithm is known as the Prewitt operator [26].

This operator is a 3×3 element convolution mask that uses pixels in the two columns adjacent to the current pixel under investigation and along the length of the edge being detected to determine whether or not an edge is present. Figure 3.10 shows a graphic description of the implementation of such an operator. As the Prewitt operator passes over pixels of equal intensity, the resulting pixels are nearly unchanged. When the operator passes over a sharp transition from high to low or low to high intensity, the calculated resulting pixel is either attenuated or accentuated depending on the bias of the operator being used. Four distinctly weighted Prewitt operators are required to distinguish between the two possible horizontal transitions and two possible vertical transitions. The mask

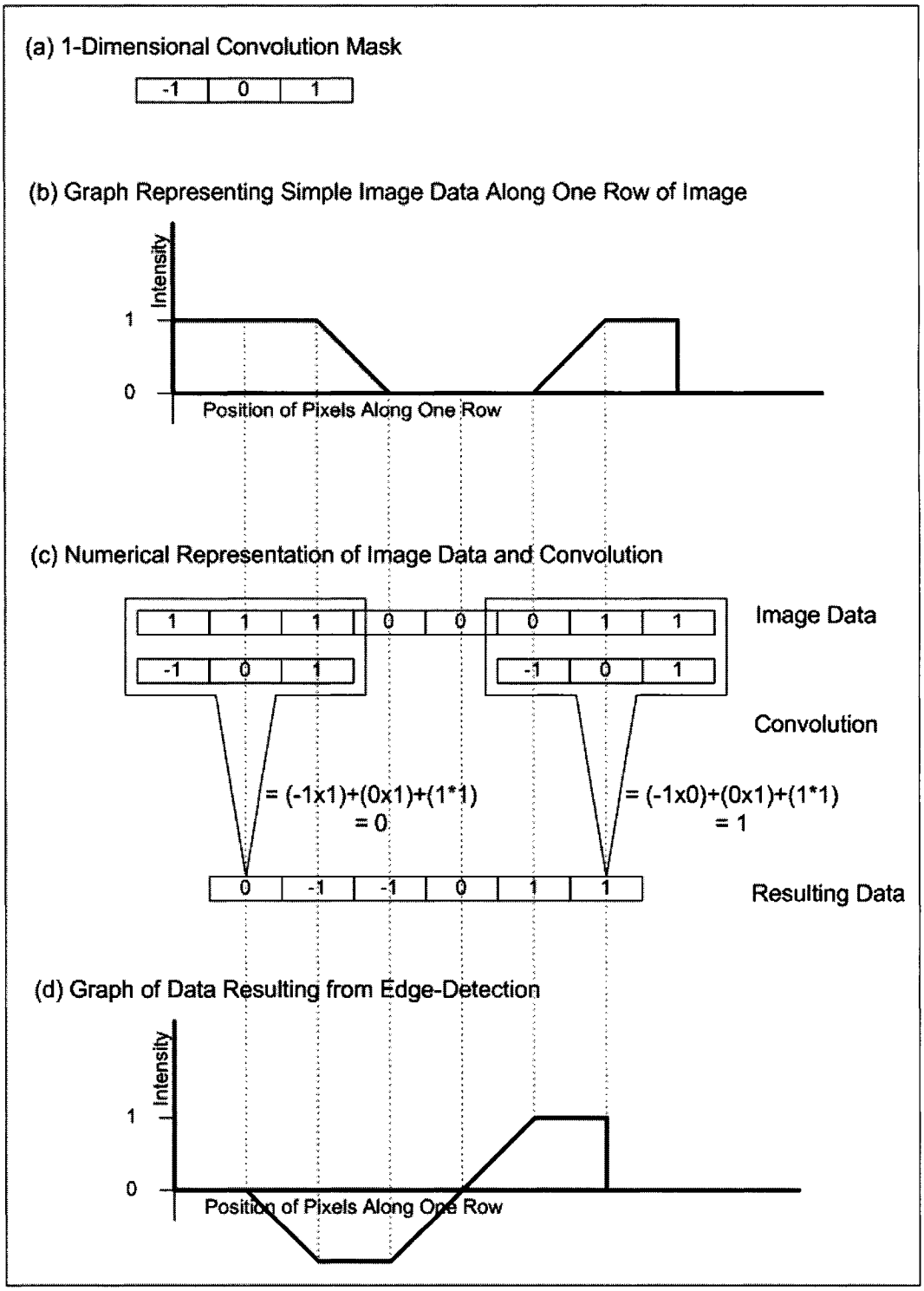

Figure 3.10: Example of the edge-detection operation.

shown in Equation 3.6 is used to reveal vertical edges that transition from high-intensity pixels located to the left of the edge to low-intensity pixels to the right of the edge. The 3-dimensional inverted view of the filtered image is shown in Figure 3.11. This figure illustrates how the transition in the j-direction from pixels of high intensity to pixels of low intensity is accentuated using the Prewitt operator of Equation 3.6. The three other Prewitt operators will have a similar effect on the other three edges. In the case of this algorithm, each of the four edges is processed separately.

$$\text{Prewitt Operator} = \begin{bmatrix} 1 & 0 & -1 \\ 1 & 0 & -1 \\ 1 & 0 & -1 \end{bmatrix}. \tag{3.6}$$

One possible benefit to using the Prewitt edge-detector is that this operator also acts as a partial noise filter by including a 3×3 pixel area in all calculations. Using the pixels located in adjacent rows will reduce the effect of noise in the calculation. This reduces the necessity of using a separate noise filter.

3.3.4 Quick Segmentation

The quick segmentation of an image is the division of the image into discreet sections based on the position of objects of interest within the image. The objects of interest are the edges of the graduations and the edge of the ruled surface on the measurement artifact. The theory behind this step is that if the location of only one horizontal and one vertical edge are known in a particular image, then the locations of all remaining features in the image can be estimated and a set of regions are defined. The estimations are based on the geometry of the artifact and the expected pose of the robot end-effector. These regions split the image into discreet segments that each contain one of the features that are to be extracted. Figure 3.12 illustrates a typical image that has been divided into regions.

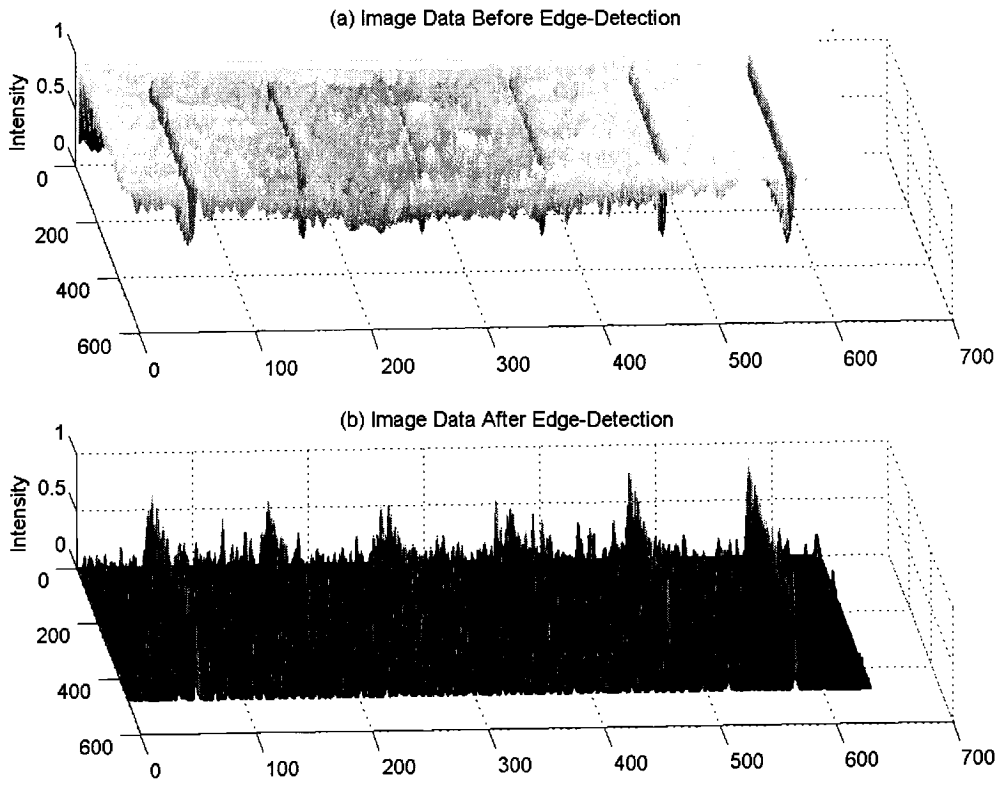

Figure 3.11: 3-dimensional representation of image data using pixel-intensity as the basis direction perpendicular to the i-j plane.

By pre-defining the width and relative position of each of these regions, this step requires that the orientation of the robot end-effector remain near vertical and relatively unchanged throughout the image capture procedure.

There are three purposes for using these regions. First, by only searching in a discreet region of the image to segment each edge, the duration of the segmentation is significantly reduced. Each image contains 480×640 pixels. By performing operations on all of these pixels during the detection of each edge, many unnecessary operations are performed. These operations are eliminated by dividing up the image. Secondly, by defining and labelling each of these regions, each edge can be easily given a label based on its location in the image. These labels can be used in subsequent calculations for comparing displaced

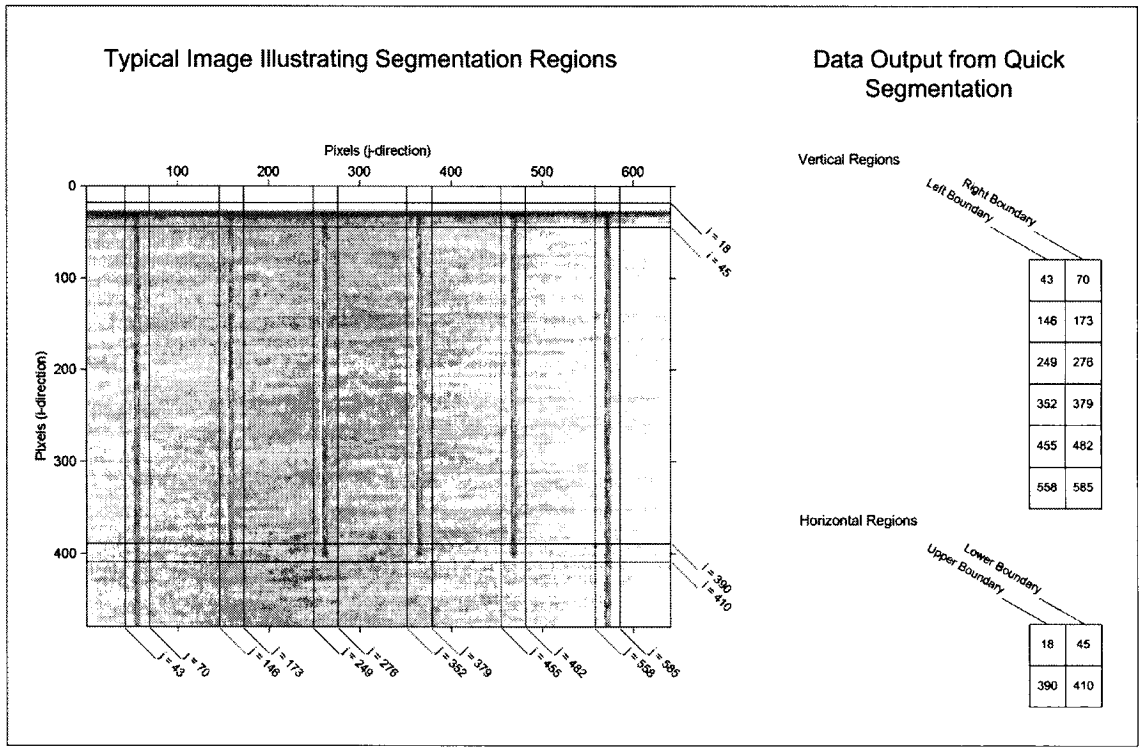

Figure 3.12: Image that has been segmented into smaller regions.

edges and identifying and eliminating edges that are deemed to be poor representation of the actual edges and unusable. Finally, the use of a search region guarantees that pixels selected to belong on an edge are at least within a certain distance of the actual edge being segmented. Without the use of these regions, it would be possible for outlier pixels to skew the results of further processing. Additional steps would have to be implemented in order to prevent this skewing. The three benefits of defining these regions are time reduction, organization, and simplicity.

3.3.5 Segmentation of Edges

The line-segmentation algorithm makes use of both the processed and unprocessed image data in determining the most likely location of the artifact edge currently being processed. The result of this segmentation is a *Slope/Intercept* form of the equation that best de-

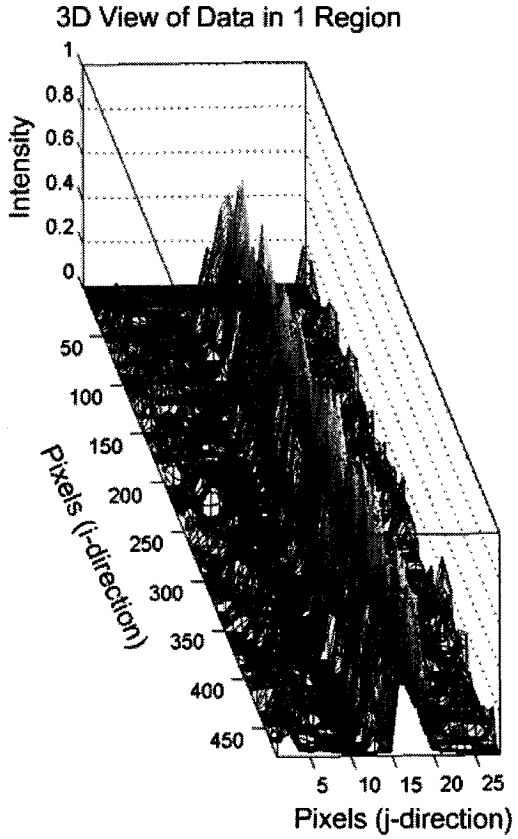

Figure 3.13: 3-dimensional image data depicting the edge located in one region of image defined by *Quick Segmentation.*

scribes the edge (i.e. $y = mx + b$). Several considerations must be made in order to achieve this result.

The processed data at this point in the algorithm is a matrix containing elements whose intensity values are larger at coordinates where a certain transition in a certain direction (an edge) is located. Figure 3.13 illustrates the portion of data from Figure 3.11 that is bounded by one of the regions described in the previous section. The edge under segmentation is oriented primarily parallel to the i direction defined by the image coordinate system. The pixels along this edge must be extracted so that they can be used in determining the location of the edge. The algorithm is able to focus on extracting a maximum of one pixel for each row of pixels perpendicular to the edges length. This

results in a maximum of 640 pixels used in the computation of any horizontal edge and 480 pixels used in the computation of any vertical edge. These values represent the maximum possible number of elements used for each edge computation, but in practice there are certain classifications of pixel which are intentionally excluded from any computations. These pixels are located in the neighborhood of any intersecting features. Two cases are illustrated in Figure 3.14. Figure 3.14(a) shows a typical illustration of the location where the horizontal edge of the ruled surface intersects any of the vertical graduations. This is considered an intersection between two features. The pixels extracted from such a location are not considered to belong to either the vertical graduation or the horizontal edge. It is unlikely that such a transition occurs at a perfect right angle as would be required in order to ignore this transition. Instead, the two perpendicular edges are connected by a round. Figure 3.14(b) is a depiction of a typical end-point of one vertical graduation. These end-points are considered as separate features from the linear regions of the graduations and are segmented in a separate process described in Section 3.4. The pixels located on the edge of an end-point comprise a round transition between the binding edges of the graduation. Most pixels located on such a transition are not collinear with the edge being segmented. Special consideration is given to the removal of these pixels from the data.

The segmentation of the edge is performed as a series of scans across the width of the artifact edge with a window referred to as the **Test Box**. This window starts from one corner of the bounding region and travels across it in search of pixels belonging to the edge in question. When the window detects a pixel belonging to this edge, the location of this pixel is recorded, the window shifts along the edge by a set distance and shifts several pixels back towards the boundary from which it began scanning. The scanning then continues until another pixel is recorded. The scanning stops when, row by row, the entire length of the edge has been scanned.

The window, illustrated in Figure 3.15, is used to extract pixels that meet a predefined

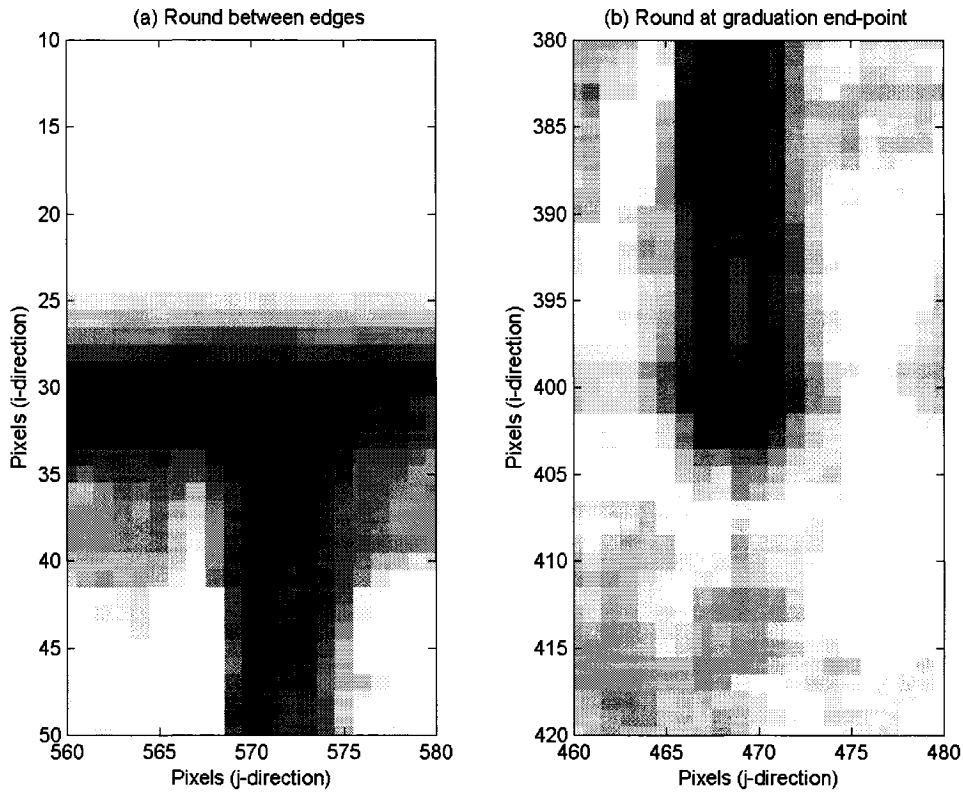

Figure 3.14: Two cases of intersecting features within an image.

set of requirements. As the window scans the processed image, point C is centred over the pixel under investigation. There are several requirements that must be met in order for this pixel to be considered part of the edge. First, the pixel must have an intensity greater then zero. All pixels that contain intensity levels below this threshold limit are not considered to belong to an edge. This requirement insures that they are not considered. Second, the intensity at pixel C must be the maximum intensity of all the pixels in the $n \times 1$ column referred to in Figure 3.15 as column A. This requirement insures that pixel C is the most likely pixel in column A to belong to the edge. The length of column A is a variable defined as n=$(2 \times TESTHEIGHT)$+1, where $TESTHEIGHT$ is the number of pixels above or below the pixel under consideration that should be used in determining its edge-worthiness. An image containing lines located closer together might use a smaller $TESTHEIGHT$

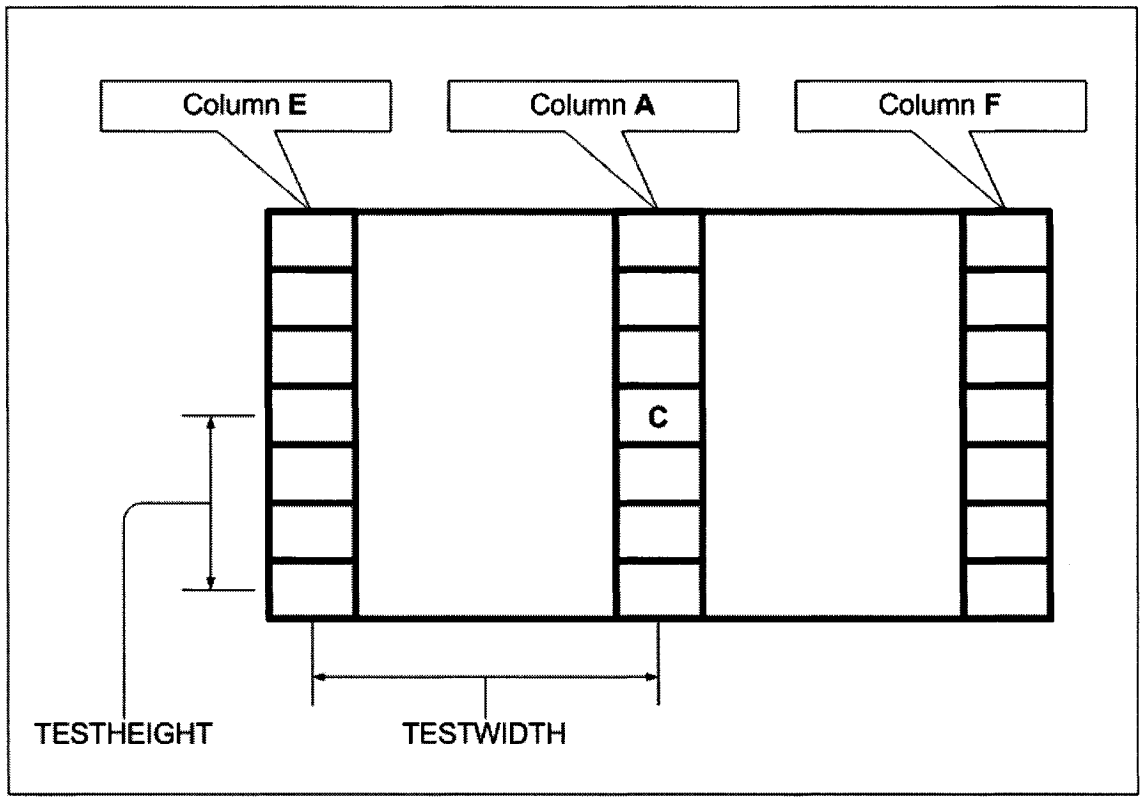

Figure 3.15: *TestBox* region used for segmenting edges.

value to be able to distinguish between adjacent lines. The third requirement is that the two $n \times 1$ matrices referred to in Figure 3.15 as columns E and F must both contain at least one non-zero element. These two columns, spaced a distance defined by m = $(2 \times TESTWIDTH)$+1 pixels, are used to exclude the pixel at C if it is located close to any edges perpendicular to the edge being segmented. Figure 3.16 shows the two cases of Figure 3.14 after the Prewitt edge detection algorithm and a threshold are applied. This algorithm is used to suppress the intensity of data not belonging to a specifically oriented edge. The rounded transitions between the intersecting features illustrated in Figure 3.14 are still present, but by scanning a distance $TESTWIDTH$ both in front of and behind the pixel under consideration and searching for the empty region that exists beyond these features. Pixels located on the rounded transitions can be excluded. With these three requirements met, the pixel located at C is added to a data matrix containing all pixels

considered part of the edge.

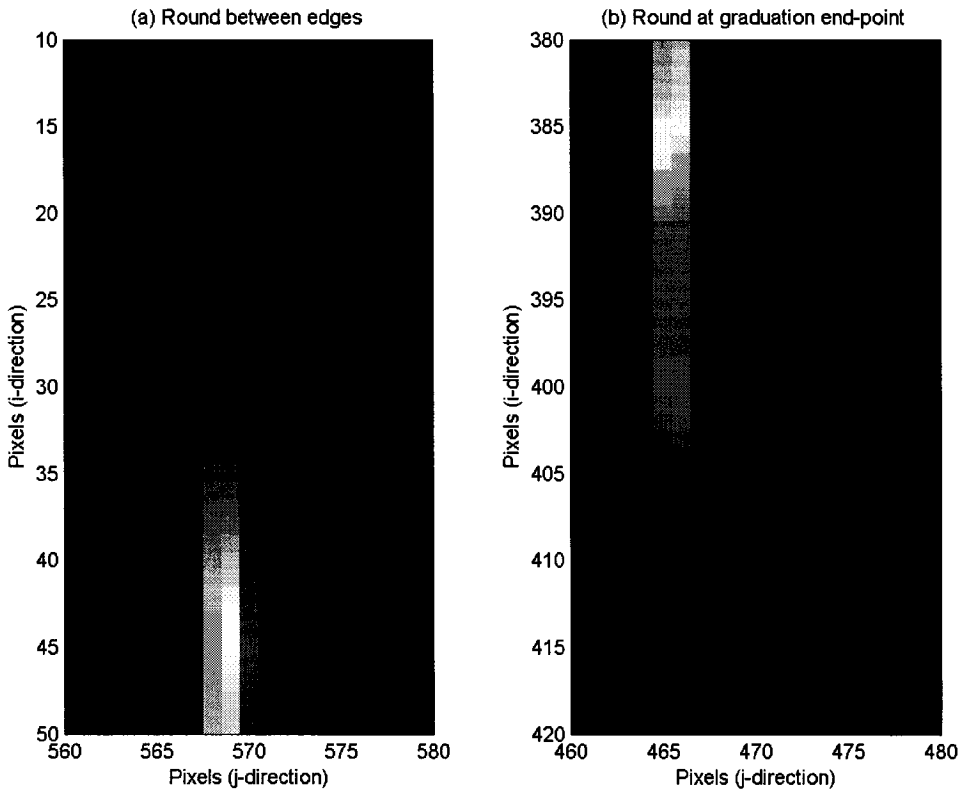

Figure 3.16: Off-edge pixels located near vertices.

The edges extracted from each image are generally oriented horizontally or vertically. The aforementioned algorithm describes the extraction of pixels from a horizontal edge. When dealing with a vertical edge, the entire image is transposed (transposition is defined as the interchanging of elements a_{ij} with elements a_{ji} where a_{ij} is the element at position (i,j) in the image). This transposition allows the vertical edges to be treated as horizontal edges. The same segmentation algorithm can then be applied. The i and j coordinates that are output from this segmentation must be exchanged at the output in order to reflect this transposition.

Upon completion of the image segmentation, the remaining data consists of an array containing the i and j coordinates of all pixels in the image that are considered to belong

to the edge. Since each pixel views an area of approximately 10 μm on the surface of the artifact, the best resolution that can be achieved using these coordinates is ± 0.005 mm error in both the i and j directions. This resolution is improved by the following.

3.3.6 Sub-Pixel Moment Calculation

The location of each pixel coordinate used to describe an edge is given to a resolution defined by the size of each pixel. In the case of this system, each pixel has a resolution of ± 0.005 mm. The resolution of the location of these coordinates can be increased through the use of a moment calculation about two directions [25]. Figure 3.17 presents the pixelated representation of a line in an image. By applying the moment calculation, one observes that the coordinates are effectively shifted based on the intensities of the surrounding pixels and a sub-pixel accuracy is achieved. The moment calculations are implemented using Equations 3.7 and 3.8 and a convolution mask. This mask is implemented in the same manner as that of Figure 3.8, with the following exception. Equations 3.7 and 3.8 are used to determine the weights of each element in the mask.

$$i = \frac{\sum\sum i \times I^P(i,j)}{\sum\sum I^P(i,i)}, \tag{3.7}$$

$$j = \frac{\sum\sum j \times I^P(i,j)}{\sum\sum I^P(i,j)}. \tag{3.8}$$

$I^P(i,j)$ is the intensity of the pixel at the location (i,j). These values are summed over a 3×3 pixel area. The pixel intensity I^P is taken from the raw image data so that any bias introduced by the subsequent processing is removed. A calculation is performed for each of the two coordinates at the location specified by the coordinates in the segmented data array.

Figure 3.18 illustrates the application of the moment calculation to one set of data. In this figure, one can observe the linear correlation coefficient for the i and j coordinates

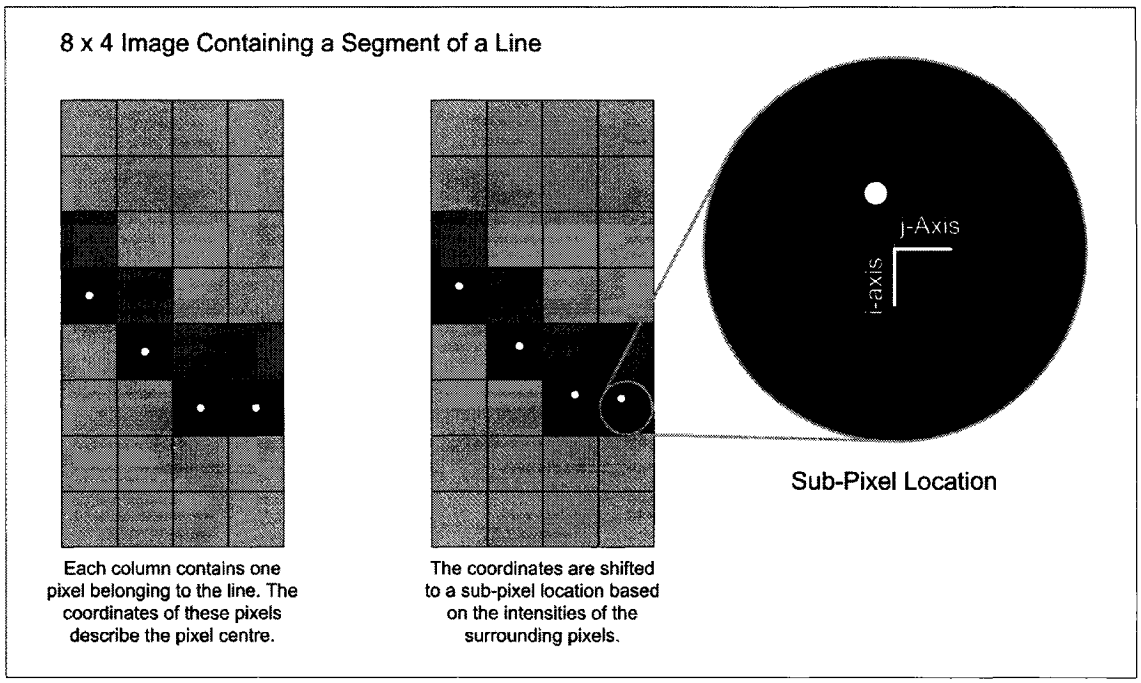

Figure 3.17: Example of the spacial shift resulting from the *Sub-Pixel Moment Calculation.*

both before and after this calculation is performed. The data output from the previous step is a set of coordinates describing an edge in the image. Since the coordinates of each of these edges are expected to rest on straight lines, one would expect that a linear correlation coefficient (LCC) representing the relationship between the i and j coordinates of any edge in this image would indicate the confidence in this data. The closer this value is to one, the more linear the relationship between the coordinates. In this figure, the moment calculation results in a 0.1522 increase in the LCC and a supposed improvement in the data. The physical improvement in the position of these pixels is observed in Figure 3.18. As the calculation is performed, each pixel appears to shift in direction towards the theoretical centre of the line that best fits the data.

After the moment calculation, the segmented data array contains a list of pixel coordinates specified to sub-pixel accuracy. These coordinates are expected to offer a better description of the edge-feature that has been segmented.

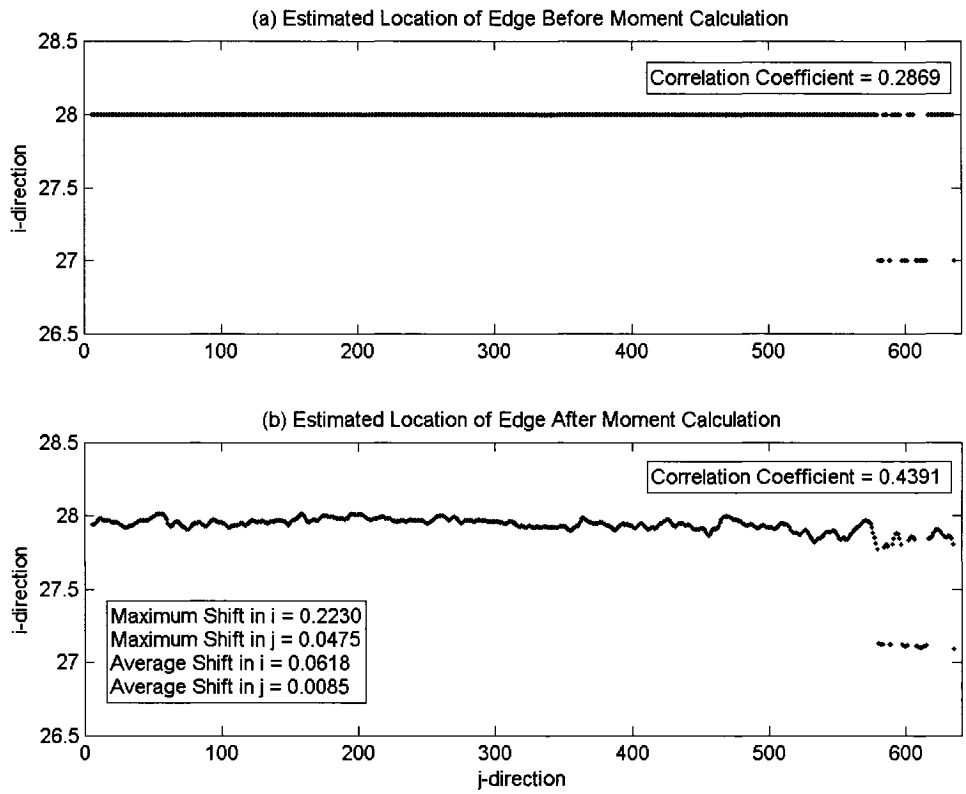

Figure 3.18: Actual spacial shift of image data resulting from the *Sub-Pixel Moment Calculation.*

3.3.7 Correlation Coefficient Filter

Linear regression is the process of selecting a line that best represents the relationship between the coordinates of the data in the segmented data array. Ideally, all of the coordinates in this array should rest in a perfectly straight line. This result is not possible in practical applications because of limitations imposed by the system that is used to extract the data and the design tolerances on the artifact from which this data is extracted. In order to achieve the best possible measurements, an attempt is made to optimize the linearity of this data set using a recursive function.

The pseudo-code for this recursive function is displayed in Figure 3.19. Initially, a $P \times 2$ data array is sent to the recursive function. This array consists of a quantity, P, of

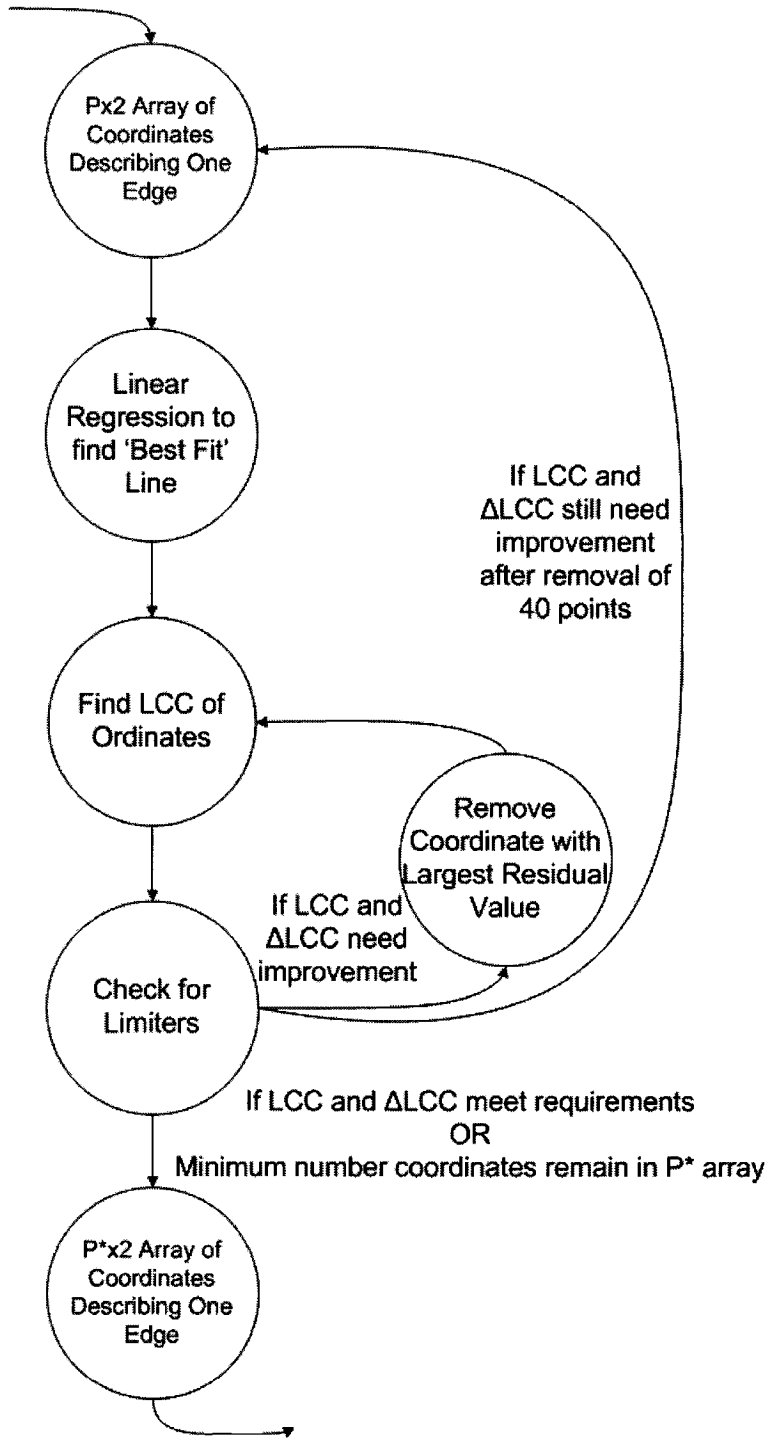

Figure 3.19: Pseudo-code for recursive coordinate elimination.

coordinates that represent one edge extracted from an image. A linear regression function is used to find the *best fit* line through the data. Using this *best-fit* line, a residual is calculated for each coordinate set. This residual is actually the perpendicular distance between the *best fit* line and each of the coordinates. At this point in the algorithm, the linear correlation coefficient (LCC) between the i and j coordinates is calculated. This LCC is used to determine whether or not the data can be improved. A set of *limiters* denoted by $LCCmin$, $\Delta LCCmin$, $Recurse$ and $PointsMin$ are used to determine the outcome of the program. The values $LCCmin$ and $\Delta LCCmin$ indicate that the function will attempt to improve the data until the LCC between ordinates reaches the lower bound of $LCCmin$ and any subsequent improvement in the data will be a value less than $\Delta LCCmin$. The value $Recurse$ is used to recurse the function in the event that at least 40 coordinates have been removed and the resulting LCC still does not meet the previously described requirements. After the removal of approximately 40 points, it is assumed that the *best fit* line computed in the first step of the function no longer describes the data. By recursing the function, this line is refit to the data and the function continues execution. The value $PointsMin$ is used to set the minimum number of coordinates that each array of data must contain in order to be considered valid. It is understood that the continuous removal of coordinates will eventually result in only two coordinates resting on a straight line. It is not likely that this straight line properly represents any edge in the image. The parameter $PointsMin$ imposes the requirement that any valid set of coordinates must possess a minimum amount of data. If the data cannot meet the requirements of this function it is considered invalid and is not directly used in any further computation. The final result of this function is the calculation of the $Slope/Intercept$ form of the *best fit* line through the optimized data.

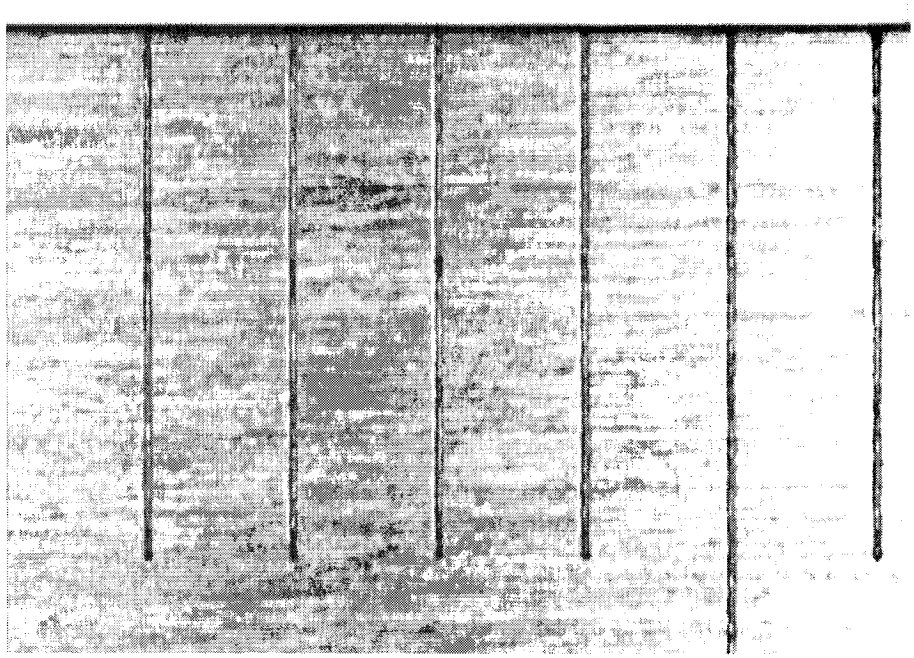

Figure 3.20: Image of the ruled surface captured by the relative measurement system and demonstrating the maximum number of five visible graduation end-points.

3.4 Segmentation of End-Points

The segmentation of the end-point location of each vertical graduation in an image is a task that must be performed separate from other tasks. There are several different types of graduations that appear in any image. Only one of these types of graduation allows the entire length of the graduation to be captured in the image. The remaining two types of graduations are too long for their image to fit across the width of the detector. The length of these fully captured graduations is given as 3.8 mm. Figure 3.20 illustrates that a maximum of five graduation end-points are visible in any image, while Figure 3.21 shows a minimum of four. The equation of the line that passes through these graduations must be extracted in order to facilitate the removal of perspective distortion from the image. This removal of perspective distortion is discussed further in Section 3.5.1.

In the world coordinate system, the line connecting the graduation end-points is ori-

ented parallel to the horizontal edge of the ruler. Unlike the horizontal edge, the line through these points is not represented by a linear feature in the image and, thus, cannot be segmented in the same manner as the horizontal edge. The segmentation of the graduation end-points requires a combination of several of the previously described algorithms.

It is understood that the position of the end-point of each graduation is located at some position along the centreline of the graduation. The linear equation representing this centreline is produced by combining the equations of both bounding edges. Each vertical graduation consists of a left and right bounding edge. The procedure used to extract these edges is described in Sections 3.3.5, 3.3.6 and 3.3.7. Figure 3.21 is a typical plot of each of these lines superimposed over an image. For each possible i value along

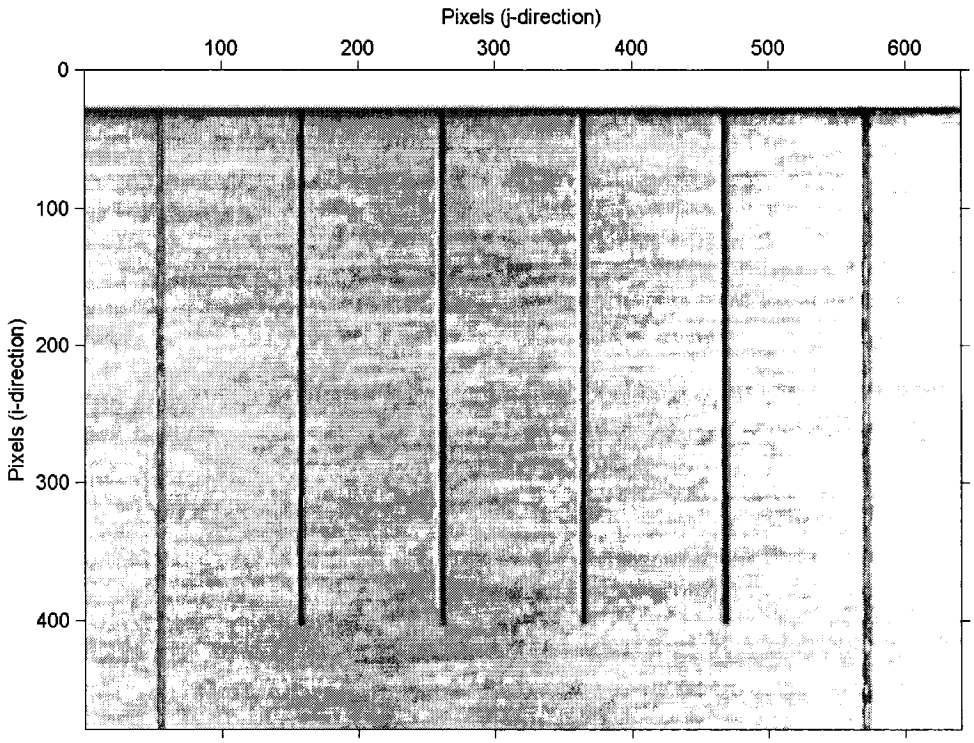

Figure 3.21: Ruled surface of the measurement artifact with plotted graduation centerlines.

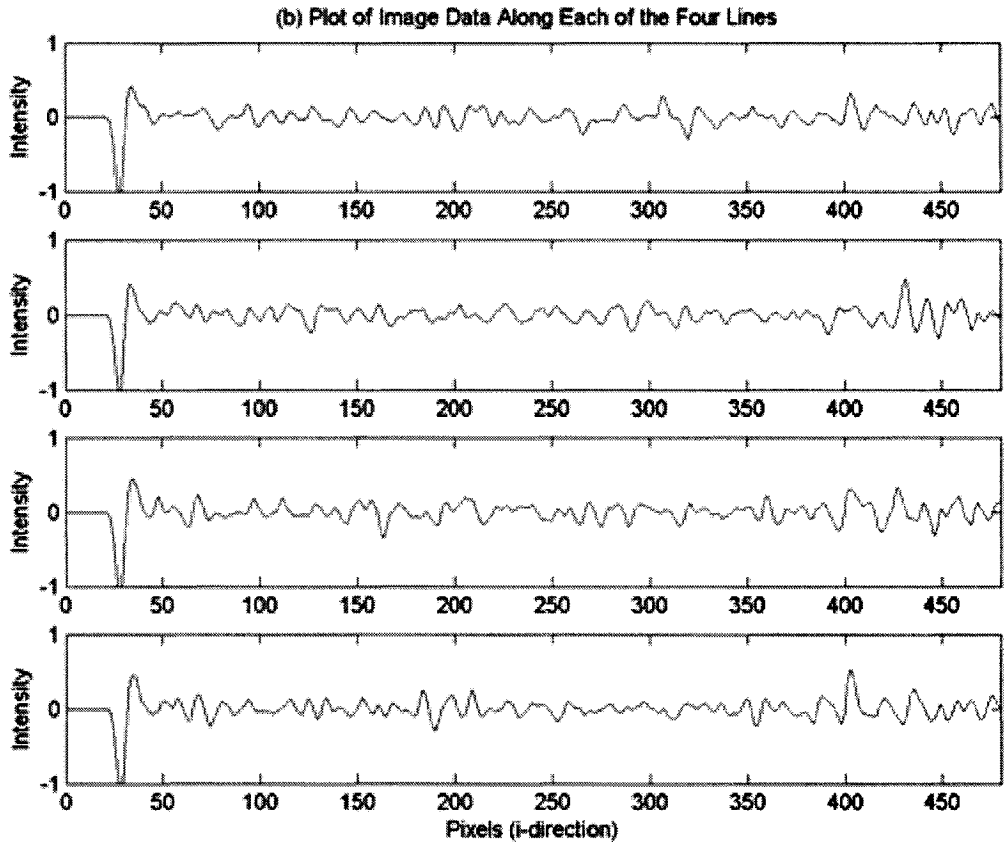

Figure 3.22: Pixel-intensities along each of the four vertical graduations in the image.

the length of a graduation, these centreline equations are used to produce an ordinate in the j direction that is rounded off to the nearest pixel value. The result of this process is a series of N sets of pixel coordinates, where N is the number of graduations in each image. One coordinate from each of these sets is the coordinate that best represents the location of the end-point of that graduation. A plot of the intensities at each pixel along these lines, Figure 3.22, reveals that the end-point of each graduation is represented by an abrupt change in the intensity of the data. This abrupt change is further revealed using the application of the Prewitt edge-detector described in Section 3.3.3. The plot of image data after edge detection is displayed in Figure 3.23. By using the search limits described in Section 3.3.4, only the local peak of this edge is detected. The coordinate in each set

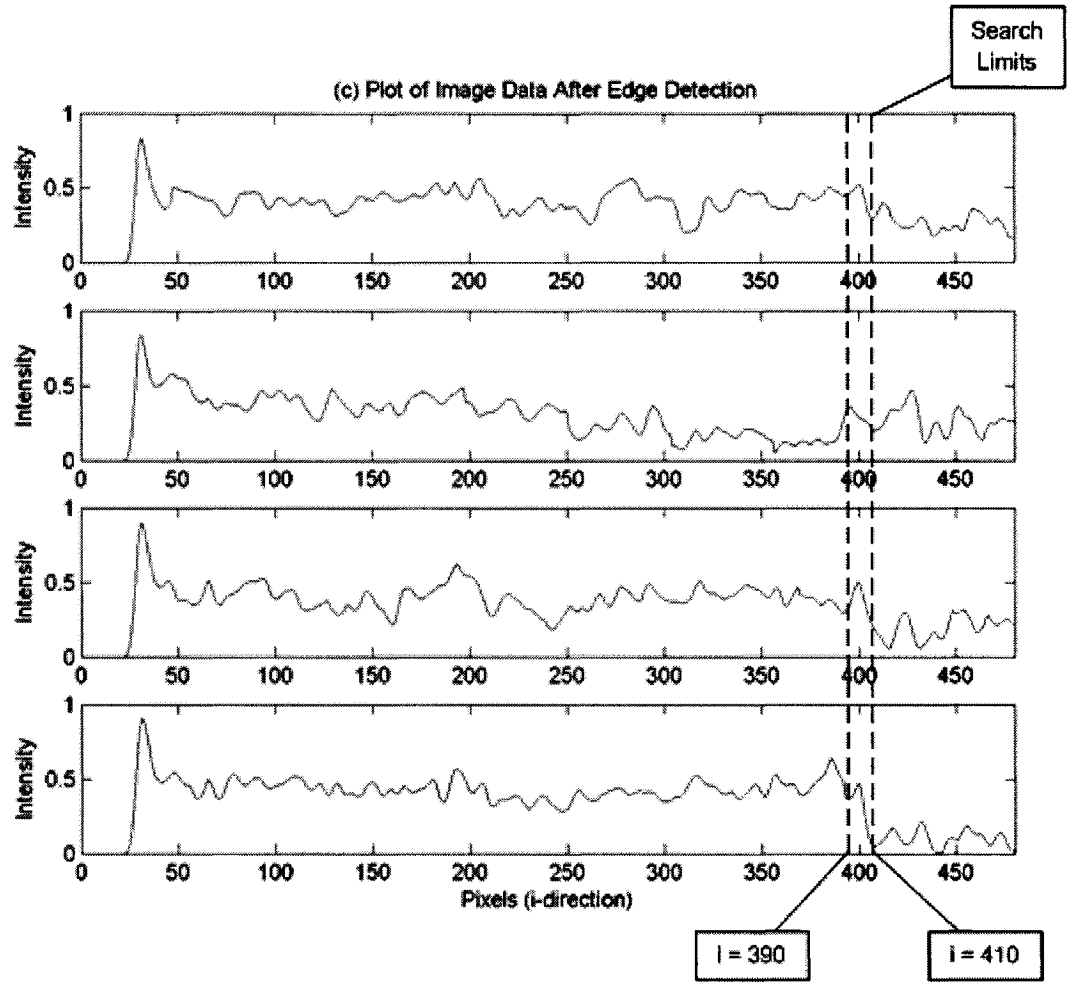

Figure 3.23: Pixel-intensities along each graduation after the application of edge-detection.

of data with the largest magnitude is used as the pixel that best represents the location of the end-point for that graduation.

The algorithm described in Section 3.3.6 is then applied at that location in order to provide the sub-pixel coordinate of each end-point. Linear regression is used to fit a line through the set of graduation end-points. This regression results in the *Slope/Intercept* form of the equation that fits through these points.

3.5 Post-Processing of Results

Digital images are captured both before and after a robot motion. The geometry of each motion is such that the images captured before and after the motion should appear identical in the absence of robot positional error. In a practical application, these images do not appear identical because there is error in the position of the robot based on its desired position. This positional error causes differences in the data extracted from each image. The procedure for post-processing involves the manipulation of multiple sets of data resulting in the displacement between sets of images. The data that undergoes manipulation consists of the linear equations representing the position of artifact features within the images. These equations are all given in the coordinate system of the image using the unit pixel-width. Figure 3.24 illustrates the labelling of these elements of data in a typical image taken by the calibration system.

The third type of equation visible in Figure 3.24 might also be available for post-processing. The equation representing the line that is created by connecting the end-points of all vertical graduations can be viewed at the bottom of Figure 3.24. In Chapter 5, it will be demonstrated that the maximum error that the robot end-effector incurs in its $X - direction$ (the $X - direction$ of the robot is intentionally aligned closely with the $i - direction$ of the CCD) corresponds to a value slightly less than 0.8 mm, which is a measure of the robot positioning accuracy in this direction. The horizontal edge of the ruled surface is a prominent feature in the images. The dramatic contrast between the surface of the ruler and the off-ruler void provides data that is much more reliable than that provided by the graduations and so it is desirable to guarantee its extraction. By positioning the horizontal edge of the ruled surface in the image a distance of 80 pixels in the $i - direction$ from the top of the image, the horizontal edge of the ruled surface is always visible within any image. A displacement of 80 pixels corresponds to an approximate displacement of

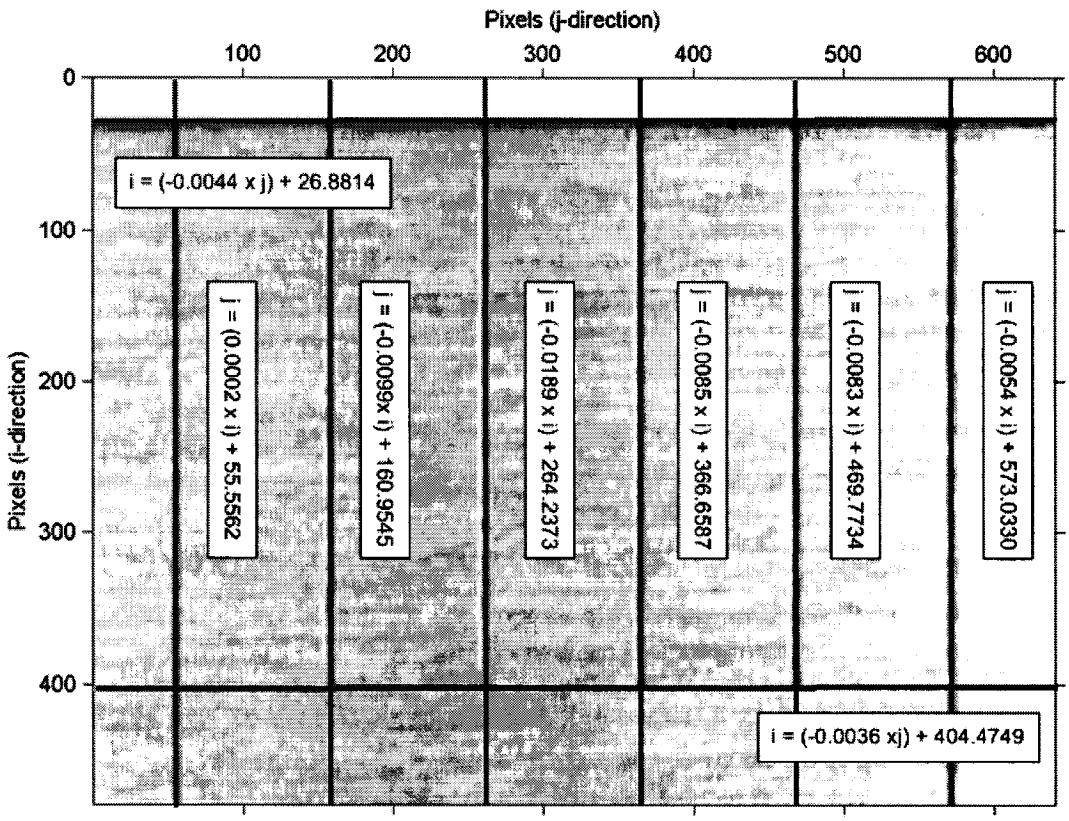

Figure 3.24: Ruled surface of the measurement artifact with labelled image features.

800 μm. As a result of this initial displacement, the end-points of the vertical graduations are not always visible. This case is demonstrated in Figure 3.25.

The image of Figure 3.25(a) shows the typical vertical initial position of the horizontal edge of the ruled surface within an image. Both the horizontal edge and the graduation end-points are visible. In Figure 3.25(b), the displacement of the robot end-effector has resulted in the disappearance of the graduation end-points from the image.

There are two possible cases that arise based on the location of these graduation end-points within the image and a conditional statement is added to the post-processing algorithm to distinguish them. This conditional statement is based on the location of the

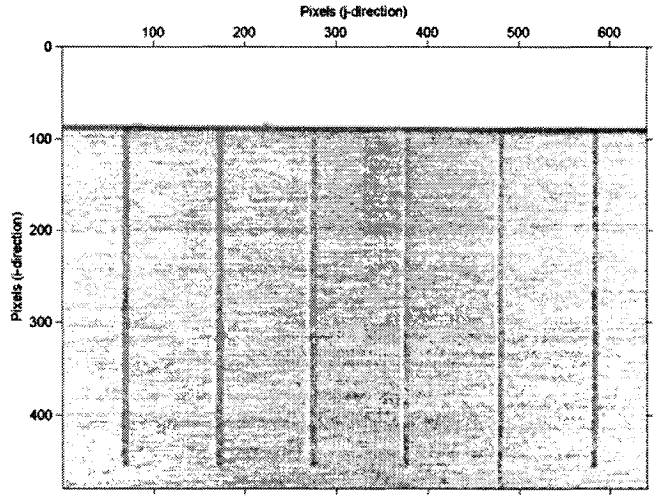

(a) Image displaying 6 vertical graduations with visible end-points

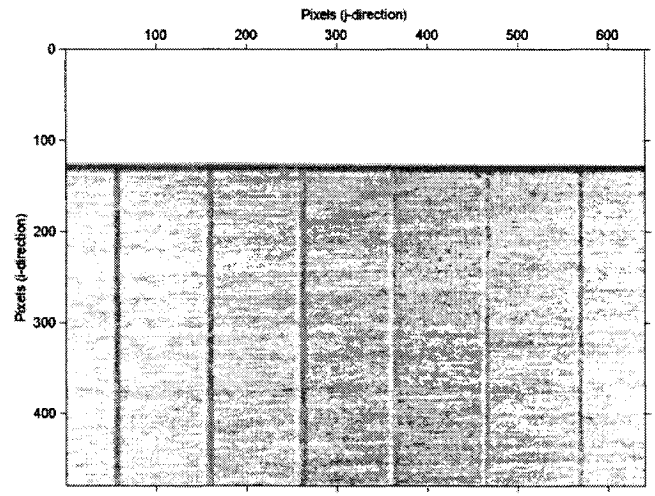

(b) Image displaying 6 vertical graduations without visible end-points

Figure 3.25: Vertical displacement of the ruler resulting in a disappearance of graduation end-points.

horizontal edge of the ruler because the horizontal edge is always visible within the image and, for small variations in camera orientation, the location of the graduation end-points with respect to the horizontal edge of the ruled surface can be estimated. A simple study of several digital images of the ruled surface resulted in an i direction threshold for the location of the horizontal edge. This threshold is a function of the resolution of the CCD, the magnification of the camera lens, the geometry of the camera/lens/ruler system and

the geometry of the measurement artifact. If the locations of all points along the horizontal edge of the ruler are less than 100 pixels in the i direction from the origin of the image then the end-points of the vertical graduations are expected to be visible within the image. The use of these data points in the post-processing of the image facilitates a post-processing algorithm involving the removal of perspective distortion from the image data. If this threshold is exceeded then the perspective distortion in the image cannot be quantified and an alternate method of post-processing is required. Sections 3.5.1 and 3.5.2 describe each of these two post-processing algorithms in detail.

3.5.1 Relative Measurement with Removal of Perspective Distortion

Perspective distortion is the phenomenon that causes lines that are known to be oriented in a parallel configuration to appear to converge. An exaggerated example of perspective distortion is illustrated in Figure 3.26. Using the *train tracks* analogy, one notes that the rails of the tracks are parallel to each other. When viewed at an angle that is not normal to the plane in which the tracks are located, the relative orientation of the tracks no longer appears to be parallel. Any attempt at extracting metric data from an image containing large amounts of perspective distortion results in potentially large errors.

For the calibration system described in this thesis, an initial attempt is made to orient the camera normal to the ruled surface of the measurement artifact. This attempt involves commanding the robot controller to orient the camera in the vertical direction. Such an orientation works to minimize the distortion resulting from perspective projection in the images of the ruler captured by the camera. The controlled orientation of the camera is limited by the repeatability of the robot end-effector. An attempt can be made to align the optical axis of the camera with the Z direction using the robot controller, but the repeatability of the robot will result in some small deviation from this alignment and so

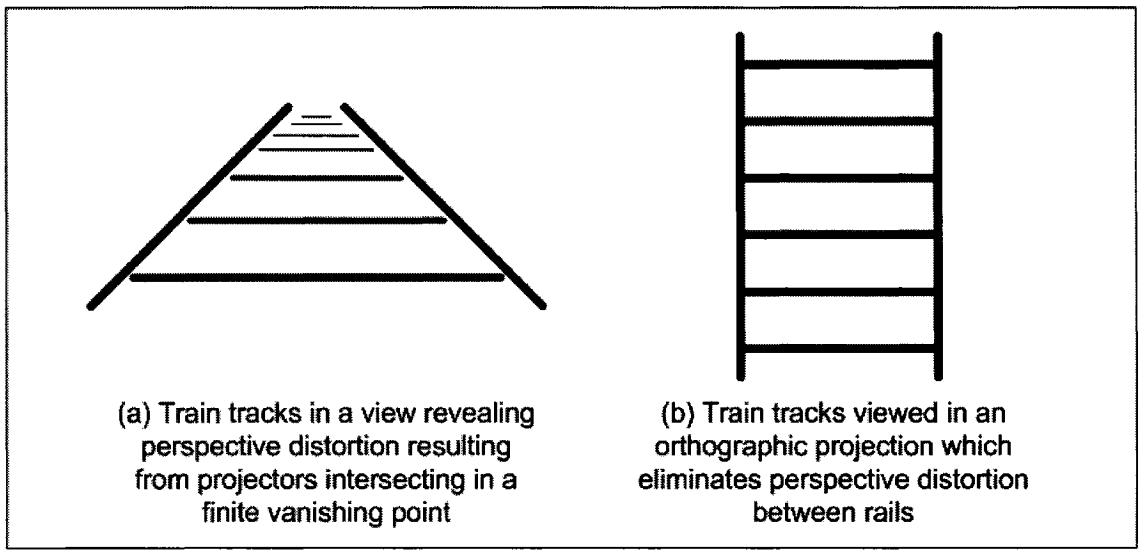

Figure 3.26: Example of perspective distortion.

it is possible that perspective distortion will be present in the image data. This distortion can be removed from the data through the use of a projective transformation [34, 35, 27, 36]. An algorithm is developed for the purpose of implementing this transformation and removing perspective distortion from the image data. This algorithm also transfers the image data from the image coordinate system into the world coordinate system.

A homogeneous transformation is used to transform homogeneous coordinate position vectors from one plane to another. It can be observed that through the use of such a transformation, collinear points in one plane will remain collinear in the resultant projected plane. This projection is illustrated in Figure 3.27.

Another feature of the homogeneous transformation is its ability to transform points representing the vertices of any arbitrary quadrilateral on one plane into the vertices of a perfect square on a second plane. The plane on which this perfect square exists is known as the affine plane for this set of vertices. By transforming the image data onto the affine plane, one is able to remove the distortion cause by the perspective of the camera. The result of this transformation is used to compute each relative measurement. The transformation of one coordinate, $\mathbf{p}$, is represented in the forms of Equations 3.9 and 3.10.

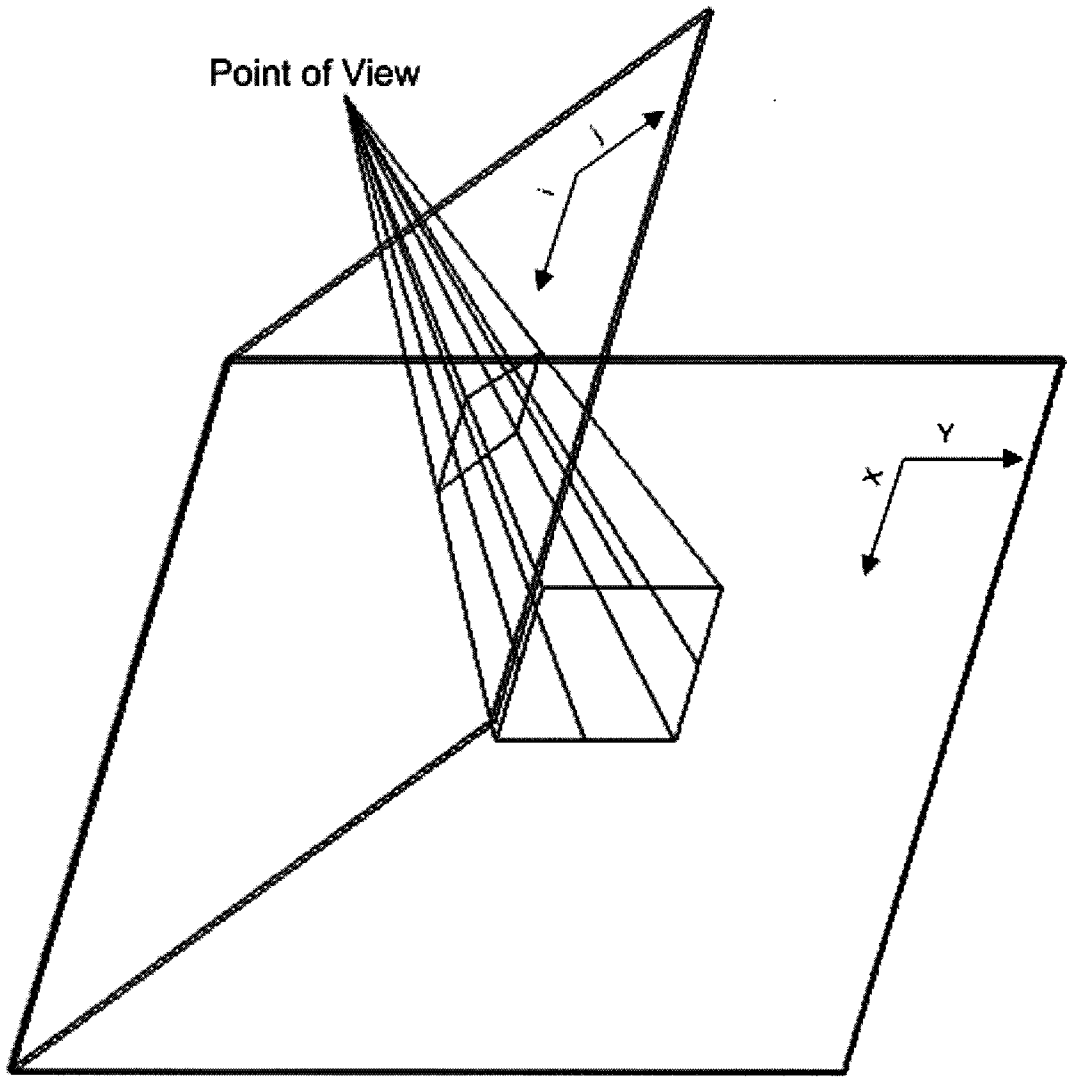

Figure 3.27: Projection of an arbitrary quadrilateral situated on one plane into a quadrilateral containing 4 right angles on another plane.

$$\rho_p \mathbf{q} = \mathbf{T}\mathbf{p}, \tag{3.9}$$

$$\rho_p \begin{bmatrix} 1 \\ q_x \\ q_y \end{bmatrix} = \begin{bmatrix} 1 & t_1 & t_2 \\ t_3 & t_4 & t_5 \\ t_6 & t_7 & t_8 \end{bmatrix} \begin{bmatrix} 1 \\ p_i \\ p_j \end{bmatrix}. \tag{3.10}$$

The variable **p** is a vector indicating the coordinates of the point on the image plane. **q** is a vector indicating the resulting coordinates of the point **p** projected on the affine plane. The matrix **T** is the 3×3 homogeneous transformation. It is a matrix operator that contains eight independent elements and transforms vector **p** in the image coordinate system to vector **q** in the world coordinate system. The value ρ_p is a scaling factor that is unique to each transformed point.

The transformation matrix, **T**, is unique for each image because the robot end-effector moves from one image location to the next and incurs variable positional error. As a result, the transformation matrix, **T**, is uniquely determined by the geometry in each image and used to remove the perspective distortion from that image. Solving for the elements of the

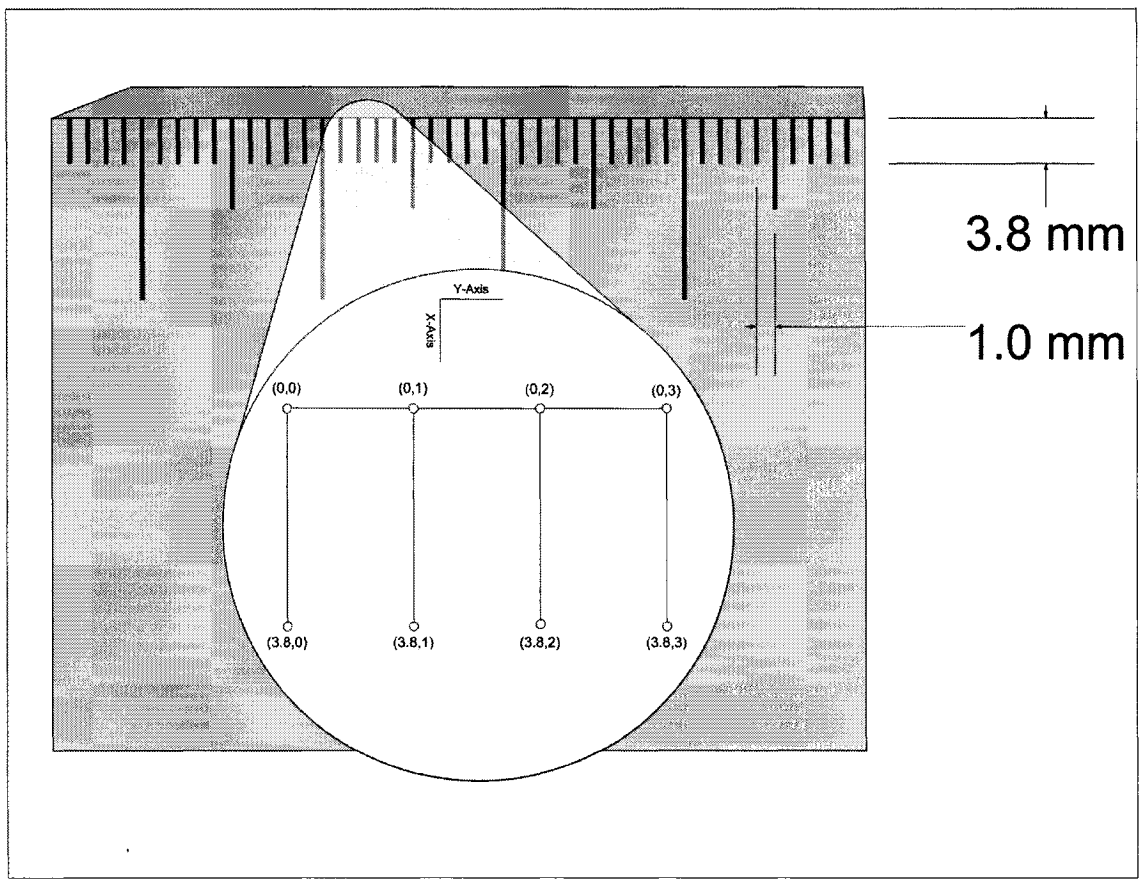

Figure 3.28: Illustration of measurement artifact with coordinates of points of intersection.

transformation matrix requires the calculation of the 8 variable matrix elements, $t_1 ... t_8$, in Equation 3.10.

A description of the measurement artifact is illustrated in Figure 3.28. This figure shows that the features on the artifact can be labelled by coordinates in the world coordinate system using specific information obtained from the manufacturer of the artifact. The graduations of the artifact are separated by a distance of precisely 1 ± 0.0015 mm. The length of these graduations is given as 3.8 mm. Using these relative dimensions, several points are labelled on the artifact. These known points represent the coordinates of the features on the measurement artifact projected onto the affine plane.

The data that has been extracted from the images in the previous steps of the algorithm consists of several equations of lines. Sets of these equations are solved together resulting in several points of intersection in the image coordinate system, as is displayed in Figure 3.24. Using a homogeneous transformation, each of these points are projected onto the affine plane, which effectively removes the effects of distortion induced by projection onto the CCD chip through the camera focal point and the relative position of the points. It can be noted that each point of intersection in the image coordinate system corresponds to one of the labelled points on the affine plane. This is the basis for solving this system of equations.

A minimum of four points must be extracted from the image in order to solve the set of 12 linear equations in 12 unknowns in Equations 3.11.

$$\begin{aligned} \rho_w \mathbf{W} &= \mathbf{Tw}, \\ \rho_x \mathbf{X} &= \mathbf{Tx}, \\ \rho_y \mathbf{Y} &= \mathbf{Ty}, \\ \rho_z \mathbf{Z} &= \mathbf{Tz}. \end{aligned}$$

(3.11)

The vectors **W**, **X**, **Y**, and **Z** are each one of the four sets of coordinates of the artifact in the world coordinate system and **w**, **x**, **y**, and **z** are the corresponding coordinates in the image coordinate system. ρ is a scaling factor that is unique to the transformation of each point. The solution to these equations, a transformation matrix **T**, can be constructed to transform points from the image space to a scaled world coordinate system. These four equations are also represented in component form in Equations 3.12.

$$\begin{aligned}
\rho_w &= 1 + t_1 w_x + t_2 w_y, \\
\rho_w W_x &= t_3 + t_4 w_x + t_5 w_y, \\
\rho_w W_y &= t_6 + t_7 w_x + t_8 w_y, \\
\rho_x &= 1 + t_1 x_x + t_2 x_y, \\
\rho_x X_x &= t_3 + t_4 x_x + t_5 x_y, \\
\rho_x X_y &= t_6 + t_7 x_x + t_8 x_y, \\
\rho_y &= 1 + t_1 y_x + t_2 y_y, \\
\rho_y Y_x &= t_3 + t_4 y_x + t_5 y_y, \\
\rho_y Y_y &= t_6 + t_7 y_x + t_8 y_y, \\
\rho_z &= 1 + t_1 z_x + t_2 z_y, \\
\rho_z Z_x &= t_3 + t_4 z_x + t_5 z_y, \\
\rho_z Z_y &= t_6 + t_7 z_x + t_8 z_y.
\end{aligned}$$

(3.12)

Using this system of 12 equations, it can be noted that there are 12 unknown variables,

including the eight elements of the transformation matrix, $t_1 ... t_8$, and the four scaling factors, ρ_w, ρ_x, ρ_y, ρ_z. This is a determinate system and is solved using a function available in the MATLAB library. The resulting transformation matrix is used to project the origin pixel of the image ($pixel(1,1)$) onto the affine plane and into the world coordinate system. This origin pixel is used as the reference origin between images. Figure 3.29 illustrates a typical image before and after this transformation occurs. In Figure 3.29(a), the coordinates of all points of interest are listed in the image coordinate system in units of pixels. Figure 3.29(b) illustrates the coordinates of the same points after the transformation. These points are listed in the world coordinate system and positioned relative to the projected location of the image origin pixel on the affine plane. These transformed points are the basis of the comparison between images.

In order to solve system 3.11, the coordinate sets of four points spanning both dimensions of an image must be determined. Figure 3.29(a) illustrates the fact that a maximum of 12 points of intersection might be extracted from each image. In the case of the extraction of more than four points from any image, the system of equations in 3.11 is generalized to the form of Equations 3.13.

$$\rho_{p_i} \mathbf{q}_i = \mathbf{T} \mathbf{p}_i. \tag{3.13}$$

Using this general form, the vector $\mathbf{p}$ represents the 3×1 coordinate vector of one point in the image coordinate system. The vector $\mathbf{q}$ is the 3×1 coordinate vector of that same point projected onto the affine plane. ρ_p is the scaler value associated with point i. The value of i is the set of numbers $1...N$, where N is the total number of points of intersection extracted from the image in question. N is a value between the minimum number of points required to solve for the transformation matrix elements and the maximum number of points that might be extracted from any image, 4 and 12. In the case where N is greater than 4, the resulting system of equations becomes over-determined and a least-

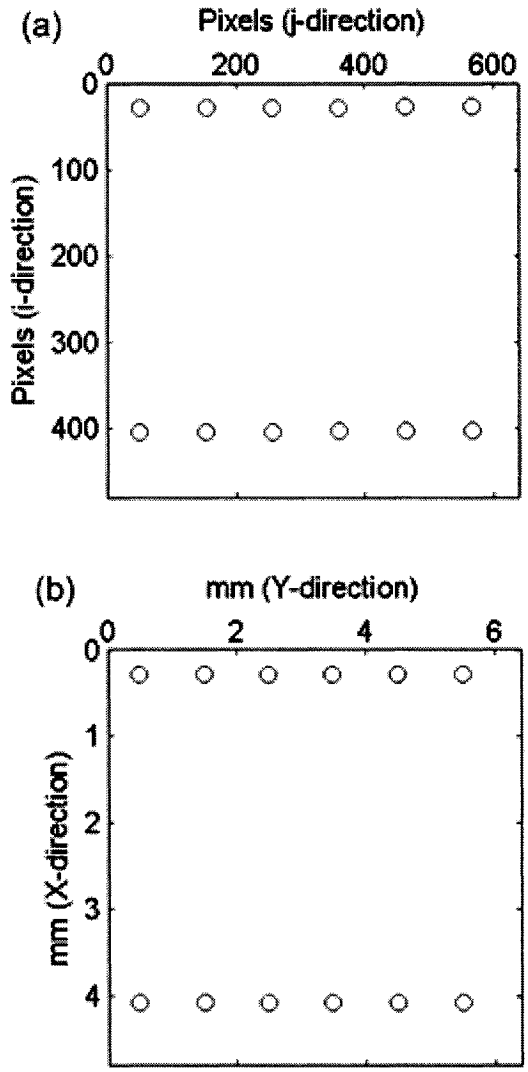

Figure 3.29: Typical image data points (a)before and (b)after projective transformation.

squares approach is used to solve system 3.13. The function (lsqnonlin.m) that implements this least squares solution is available in the MATLAB library.

The data from each image consists of a set of N coordinates in the world coordinate system representing the locations of N features of the measurement artifact projected onto the affine plane. Figure 3.30 displays the superposition of data extracted from two sets of images. In order to determine the relative displacement between these two sets of data, a

series of calculations are performed.

The relative displacement between features in any two images is then calculated. The lines connecting corresponding points in Figure 3.30 represent displacements produced using only one reference point in the image. The actual calculation of these displacements requires the calculation of separate displacement values in both the X and Y directions. Since the geometry of the measurement artifact is given, the length of each of these lines between two identical sets of data would already be known. Any deviation from the set of known lengths using any two non-identical images represents the relative displacement between these two images. All available displacement values for each image are used to compute the average displacement across the entire image. This method of computing the relative displacement results in anywhere between 16 and 144 possible displacements used in calculating this average and is discussed further in Section 4.2.4.

3.5.2 Relative Measurement Using Image Scaling

The process of image scaling uses features visible within an image to provide a scale factor and appropriate X and Y directions used in extracting displacements from a digital image in the world coordinate system. The scale factor is computed using the distance between adjacent points of intersection along the horizontal edge of the measurement artifact. The X and Y directions are determined by the orientation of the horizontal edge and the vertical graduation at each point of intersection. The limitation of this algorithm is a tolerance that is placed on the orientation of the camera, with respect to the plane of displacement. Figure 3.31 illustrates the reason for this limitation. In Figure 3.31(a), an illustration of a plate with a perfectly square face is visible. The image of this face is captured at a camera orientation that can be described by placing the optical axis of the camera perpendicular to the plane of displacement of the object. From the point of view of the camera, this displacement is not noticeably distorted by perspective projection. The

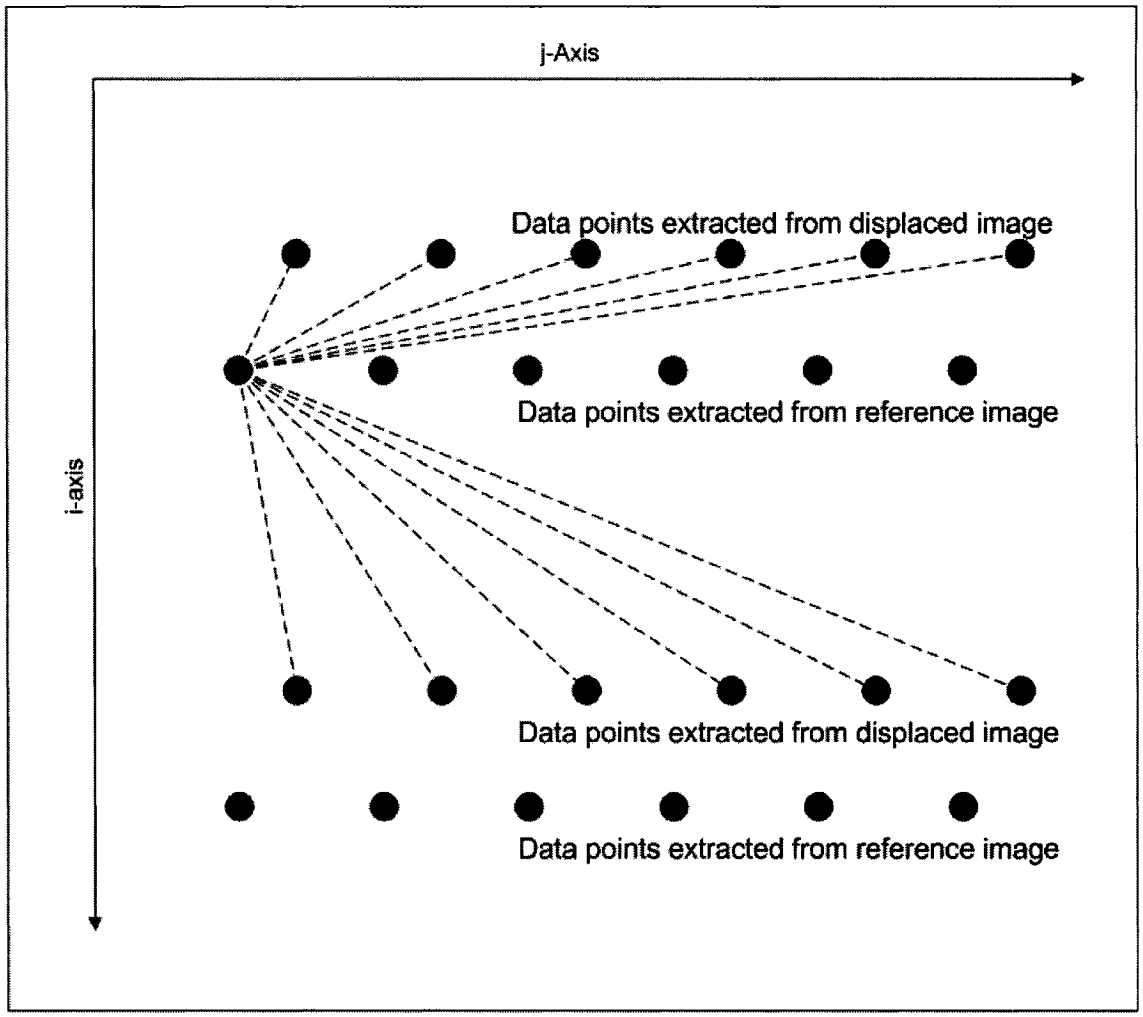

Figure 3.30: Measured displacements using one point in the reference image.

only requirement for determining the displacement of the plate is the scaler conversion factor relating pixels to millimeters (camera rotation in the Z direction is not illustrated in Figure 3.31). In Figure 3.31(b), an angle is introduced between the normal of the plane of displacement and the optical axis of the camera. As a result, perspective distortion is visibly present. The figure illustrates that as the plate is repositioned by an equal amount in both the X and Y directions of the world coordinate system, both the direction and magnitude of the displacement captured by the camera in the image coordinate system are skewed with respect to the image coordinate system. This distortion is difficult to remove

and requires a procedure similar to that described in Section 3.5.1.

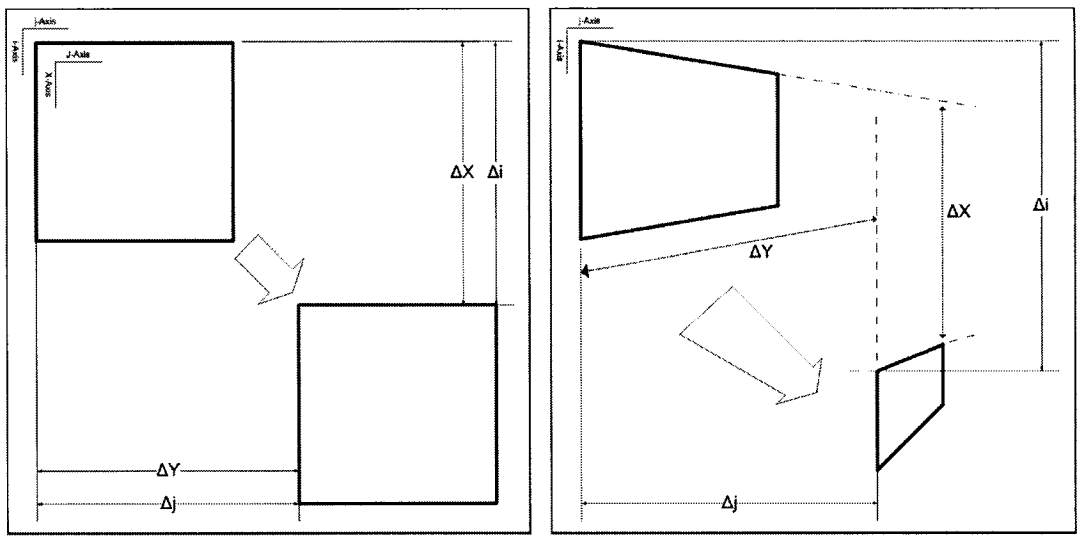

(a) Object is displaced – the plane of displacement is orthogonal to the optical axis of the camera

(b) Object is displaced – the plane of displacement is not orthogonal to the optical axis of the camera

Figure 3.31: Effects of perspective distortion on extracting measurements from a digital image.

If the plane of the image capture device and that of the face of the measurement artifact are parallel, then the only two situations that need to be addressed are the scale conversion factors between the two coordinate systems and the rotational offset of these coordinate systems in the Z/k direction. An algorithm developed for this purpose is now described.

Each relative measurement requires two images. The first image is referred to as the reference image. This image is used as the reference to the location of the robot before any movement has occurred. The second image is referred to as the displaced image and it represents the location of the robot after any movement. In order to determine the

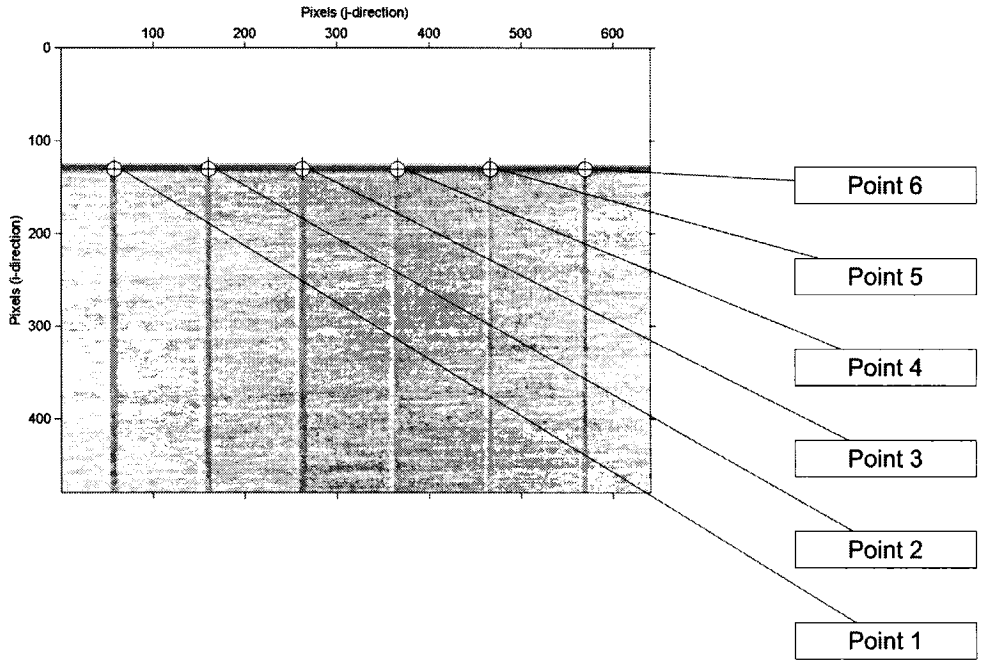

Figure 3.32: Image data extracted from a typical image consists of equations representing both horizontal and vertical lines.

deviation between these two images, several scaling factors and several coordinate axis directions must first be extracted. These values are extracted from the reference image.

The first step of the algorithm is used to determine the scale factors. The reference image data consists of the equations of two to six vertical lines and one horizontal line that are visible in each image. At least two vertical lines must be extracted from the image in order to produce a scale factor since the scale factor is essentially the distance between any two graduations. A maximum of six vertical graduations may be present in any image. The points of intersection between all features described by the image data are determined by equating the lines representing each vertical graduation with the horizontal edge. This process results in two to six possible points of intersection. A case where six points are visible can be viewed in Figure 3.32 with each point given a label.

Using the information describing the geometry of the measurement artifact, it is de-

termined that the distance between each adjacent point in the world coordinate system is 1 mm. A simple scale factor can be extracted by computing the length between any two adjacent points in the image using the coordinates of the points in the image coordinate system. This length is the denominator of the scale factor (SF). The numerator of the scale factor is the 1 mm distance between these points. This is illustrated using Equation 3.14, where $SF_{P_1P_2}$ is the scale factor between points P_1 and P_2, and i and j are the coordinates of each point in the image coordinate system.

$$SF_{P_1P_2} = \frac{1}{\sqrt{(i_{P_1} - i_{P_2})^2 + (j_{P_1} - j_{P_2})^2}} \left[\frac{mm}{pixel}\right]. \tag{3.14}$$

A distinct scale factor is produced for each point of intersection of the image data. These multiple scale factors insure that the measured displacement at a point is based on the scale that is determined in the immediate vicinity of that point. This procedure also reduces the effects of perspective distortion in the direction of the horizontal edge. There are three possible cases for the calculation of a scale factor. These cases can be observed in Figure 3.33.

In the first case, the scale factor is calculated at a point that is situated directly between a set of adjacent points. This case is illustrated in Figure 3.33(a). When the coordinates of both adjacent points are available, the scale factor at the point in question is simply the average of the scale factors on both sides of the point. The second possible case arises if an adjacent point only exists on one side of the point in question. This case is illustrated in Figure 3.33(b). The scale factor in this case is determined using only one adjacent point. The third case occurs when the points on either side of the points in question are not considered to be adjacent. This case is illustrated in Figure 3.33(c). A scale factor is calculated on either side of the point in question and these two factors are averaged. Equation 3.15 is used to calculate the scale between two points that are not adjacent. The

value AD is the actual distance between these two points in the world coordinate system. This distance will be an integer value between $2mm$ and $5mm$ and for near vertical camera orientation can be easily estimated based on the pixel-distance between these two points in the image coordinate system.

$$SF_{P_1P_2} = \frac{AD}{\sqrt{(i_{P_1} - i_{P_2})^2 + (j_{P_1} - j_{P_2})^2}} \left[\frac{mm}{pixel}\right]. \tag{3.15}$$

The second step of the algorithm is used to produce a set of directional vectors at each point of intersection. It is understood that the directions of the i and j unit vectors do not necessarily align with the directions of the X and Y unit vectors, although an attempt is made to do so. Relative measurements must be taken in the world coordinate system defined using the ruled surface of the measurement artifact and so the directions of displacement are defined using the slopes of the features in the image data. The Y direction is defined by the slope of the equation representing the horizontal edge of the artifact. There is only one such equation available and it is used for all points of intersection since it describes the horizontal edge passing through all of these points. The X direction is defined by the slope of the vertical graduation that passes through each point of intersection in the image. One set of X and Y directions is defined for each point of intersection as illustrated in Figure 3.34(a). These directional coordinates are used to convert the displacement at each point of intersection into an X component and a Y component. An example of this conversion is illustrated in Figure 3.34(b).

One displacement in both the X and Y directions is calculated using the scale factors and directional coordinates. Perspective distortion has not been removed from this data and so a procedure unique to that described in Section 3.5.1 is used to produce these displacements. This process begins with the computation of the point that defines the intersection of the line that travels through the point in the reference image (Image 1)

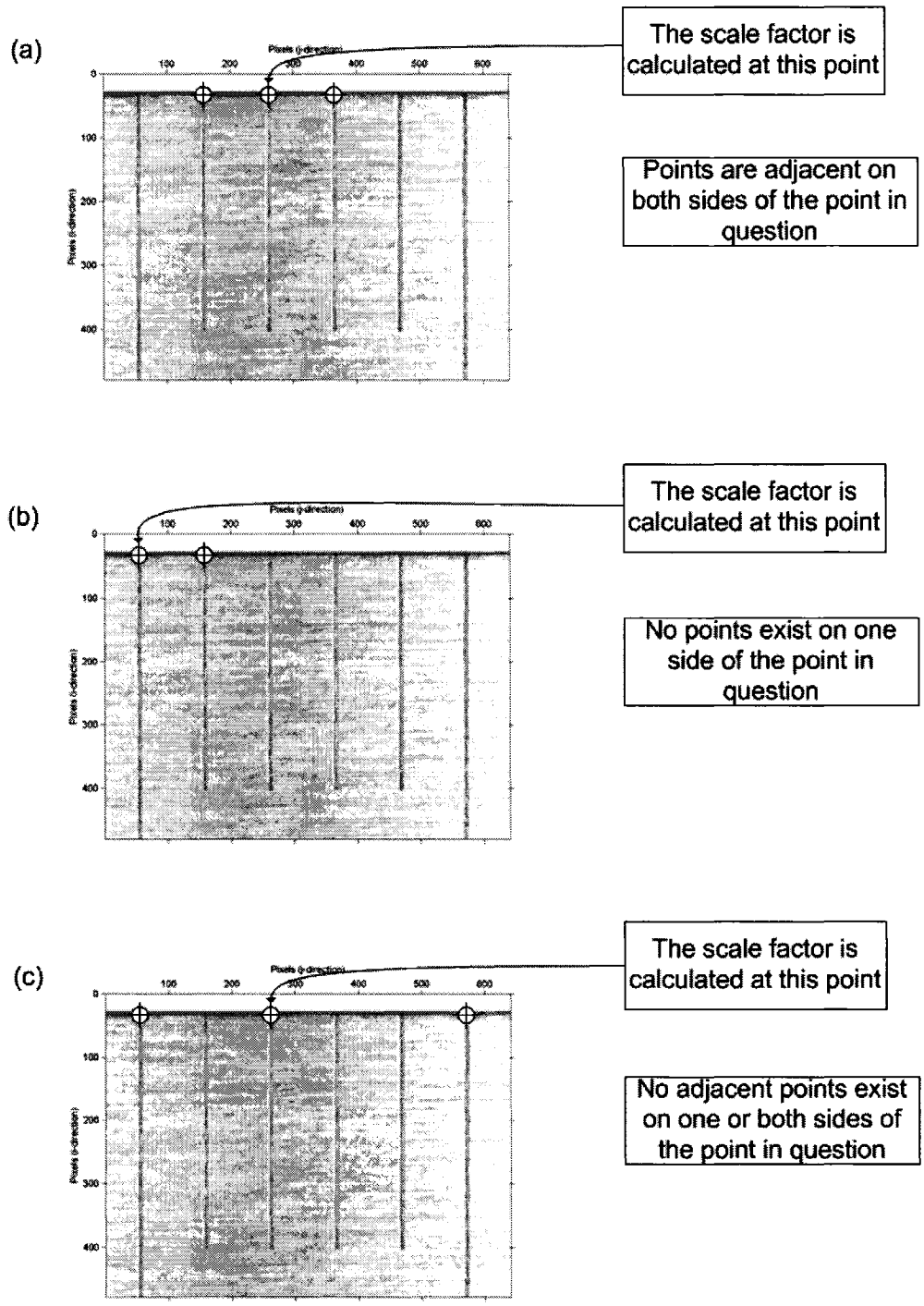

Figure 3.33: Three cases for the calculation of image scale factors.

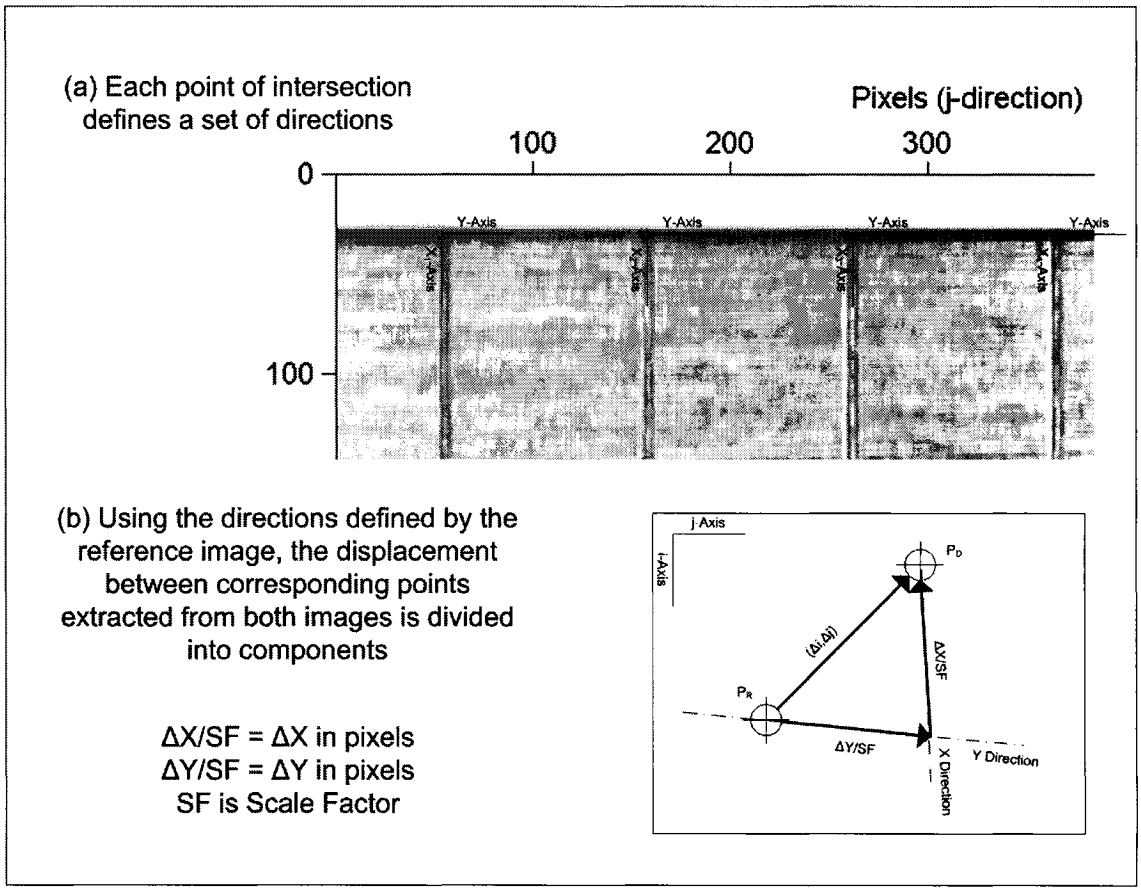

Figure 3.34: One set of directional coordinates defined at each point of intersection in an image.

parallel to the Y axis of the world coordinate system and the line that travels through the point in image two, parallel to the X direction of the world coordinate system. This point of intersection is computed by rearranging Equations 3.16 and 3.17 into Equations 3.18 and 3.19. The X and Y directions are each defined by a slope given with respect to the i or j axis. These slopes are denoted by η_{VERT} and η_{HOR} for the X and Y directions, respectively.

$$y - y_1 = \eta_{HOR}(x - x_1), \tag{3.16}$$

$$x - x_2 = \eta_{VERT}(y - y_2), \tag{3.17}$$

$$y_{int} = \frac{y_1 + \eta_{HOR}((x_2 - x_1) - \eta_{VERT}\eta_{HOR})}{1 - \eta_{VERT}\eta_{HOR}}, \tag{3.18}$$

$$x_{int} = x_2 + \eta_{VERT}(y_{int} - y_2). \tag{3.19}$$

The displacement in the X direction is defined in Equation 3.20 as the distance between the point extracted from the reference image and the point of intersection given by x_{int} and y_{int}. The displacement in the Y direction is defined in Equation 3.21 as the distance between the point extracted from the displaced image and the same point of intersection. It can be noted that these two directions may not appear to be orthogonal in the image coordinate system as a result of small amounts of perspective projection, but the calculation of displacements in these directions results in estimations of displacement along the orthogonal X and Y directions of the world coordinate system.

$$\Delta X = \sqrt{(x_{int} - x_1)^2 + (y_{int} - y_1)^2}, \tag{3.20}$$

$$\Delta Y = \sqrt{(x_{int} - x_2)^2 + (y_{int} - y_2)^2}. \tag{3.21}$$

This displacement calculation is applied to each point in the reference image that has a corresponding point in the displaced image. It is possible for an image to contain a point that has no corresponding point in the other image. The data corresponding to the missing point is not used in the calculation of any displacement. Instead, this data is discarded. The resulting two to six coordinate displacements are averaged in order to produce a robust average displacement for the entire image.

Table 3.1: Summary of image processing algorithm and data output.

Algorithm Name	Type of Output	Description of Output
Pre-Processing Algorithm	336 KB JPEG image	Data stored on computer drive
Image Representation	$m \times n$ data array	m and n are the dimensions of the captured images
Noise Filter Algorithm	$m \times n$ data array	
Edge Detection Algorithm	$m \times n$ data array	
Quick Segmentation Algorithm	N sets of j coordinates M sets of i coordinates	N is number of visible graduations M depends on visibility of end-points
Segmentation of Edges	$N+1$ arrays containing $P \times 2$ elements	$N+1$ is number of extracted lines P is number of coordinates per line
Sub-Pixel Moment Calculation	$N+1$ arrays containing $P \times 2$ elements	
Correlation Coefficient Filter	N^*+1 equations in form $[b\ m]$	N^* is number of valid lines $[b\ m]$ is slope/intercept form of line
Segmentation of End-Points	$[b\ m]$	b is axis intercept m is slope of line through end-points
Post-Processing	ΔX and ΔY	displacements of EE in the plane of the ruled surface

3.6 Summary of DIP Algorithm

Table 3.6 provides the name of each step in the algorithm, the type of data that each step produces and a description of the output data.

Chapter 4

Experimental Results and Discussion

The digital image processing algorithm is able to extract measurements characterizing the position of the robot end-effector, in the $X - Y$ plane with respect to the location of the measurement artifact. Since the position of the measurement artifact remains unchanged as the robot is displaced, a comparison of images taken before and after the robot movement results in a measurement of the relative displacement of the robot end-effector. The resolution of these measurements is difficult to determine based on the dissection of the image processing algorithm. A procedure described in Section 4.1 is used to test the validity of the algorithm and to determine the amount of error that these measurements contain. Using the results of this procedure, the effects of altering several parameters within the algorithm are observed in Section 4.2 and an improvement in the resolution of the measurements is achieved. A full characterization of the resulting relative measurements is presented in Section 4.3.

4.1 Measurement Validation

A procedure is developed to be used in the quantification of the resolution of these image measurements in order to determine if the algorithm meets its design requirements. This

validation procedure requires that the pose of the robot end-effector remain unchanged throughout the procedure. It is expected that the resolution of these measurements is somewhat better than the stated repeatability of the Thermo CRS A465 manipulator. Any motion of the manipulator will introduce a maximum possible error of ± 0.069 mm into each measurement. The introduction of this error is avoided if the manipulator remains fixed. Instead, a precision external displacement device is used to reposition the measurement artifact. This device allows the precise magnitude of the displacements within the $X - Y$ plane to be controlled. The controlled displacement values are compared with the displacement values measured by the digital image processing algorithm. Based on this comparison, the resolution of the image processing algorithm can be determined.

The Vernier X-Y table is a displacement device that controls the position of an object in the $X - Y$ plane. The device, displayed in Figure 4.1, has two perpendicular axes. The displacement along each axis is manipulated by one manually controlled actuator

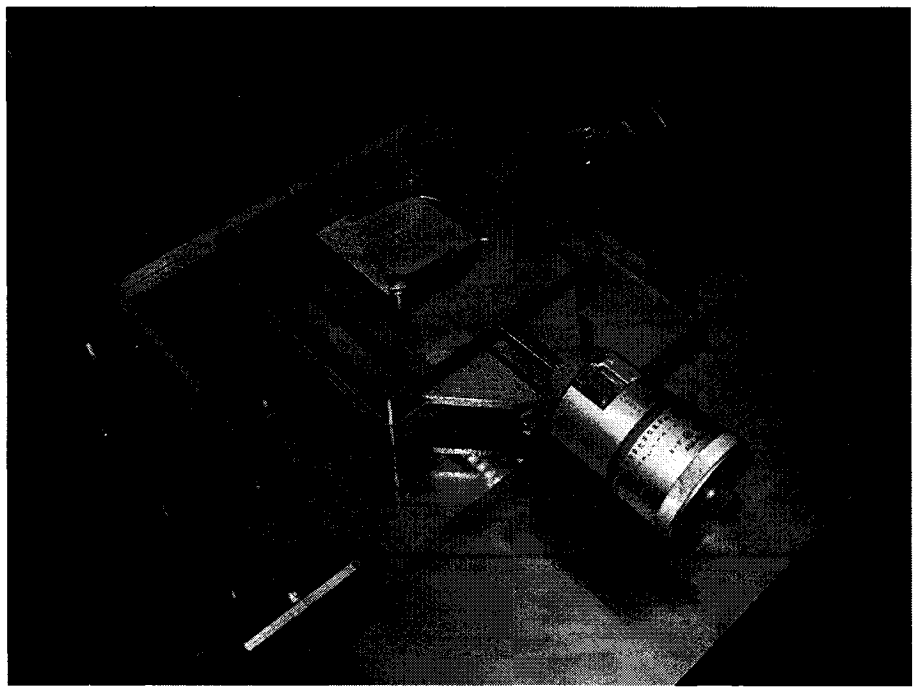

Figure 4.1: Mitotoyo Vernier X-Y table.

with a minimum possible increment of 5.08 μm (0.0002 inch). The precision in these increments is estimated as ± 0.00254 mm (1/2 the smallest increment [37]) based on the visual extraction of measurements from these actuators. The validation procedure uses this device to determine the resolution of the image processing output. In Figure 4.1, one can note that a small measurement artifact is fixed onto the controlled surface of the $X - Y$ table. This artifact is used to characterize the repeatability of the manipulator [1].

The precision-machined ruled surface is fixed onto the Vernier $X - Y$ table in the same manner as the artifact of Figure 4.1 and placed into the robot workspace. The robot end-effector is positioned such that the camera can clearly extract images from the designated $X - Y$ plane defined by the surface of the ruler. The robot remains stationary for the entire calibration procedure. The Vernier $X - Y$ table is used to displace the measurement artifact within the field of view of the camera, into 300 positions. At each position, an image of the artifact is extracted and processed. These 300 positions construct a rectangular pattern of dimensions 558.8×203.2 μm. This pattern can be viewed in Figure

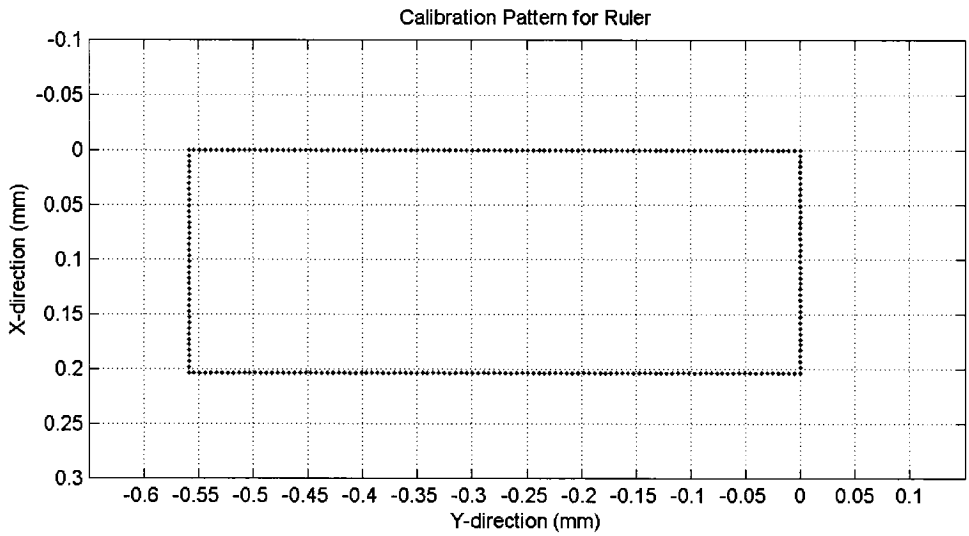

Figure 4.2: Displacement pattern plotted using the X-Y table.

4.2. The position from each image in the set of 300 is compared with that of a reference image (indicated in Figure 4.3) in order to produce the relative displacement of the ruler. By comparing these displacement values produced using the image processing algorithm with those controlled using the Vernier $X-Y$ table, a reasonable estimate of the resolution of the image processing algorithm is obtained.

The selection of the calibration pattern is based on the design requirements described in Chapter 2. This pattern depicts a displacement of 558.8 μm in the Y direction. The hard requirement of the system is to be able to measure displacements of greater than 400 μm in the Y direction and this requirement is exceeded using this pattern. Displacement in the Y direction is slightly more complicated to calculate than that of the X direction since any image may contain a number of graduations and these graduations can disappear off of the edge of the image as the artifact is displaced. This calibration pattern illustrates the effects of removing a graduation from one side of the image and adding a graduation to the other side. This pattern also requires that multiple reference graduations be used in the calculation of artifact displacement. Figure 4.3 illustrates the maximum displacement of the artifact in both directions. These four images represent the four corners of the calibration pattern. It can be noted that the displacement in the Y direction results in the removal of the reference graduation on the left side of the image and the addition of another graduation on the right side of the image. The use of these reference graduations allow the system to extract measurements over a distance of up to 2.5 mm in the Y direction. This is discussed further in Section 4.3.

The initial image captured during this process will contain some measurement of the position of the end-effector relative to the $X-Y$ table. Included in this measurement will be a small error, as is the case for all measurements. By using this point as the zero-error origin of the calibration pattern, the error inherent in this measurement will adversely affect all subsequent measurements. This concept is illustrated in Figure 4.4. In Figure 4.4(a),

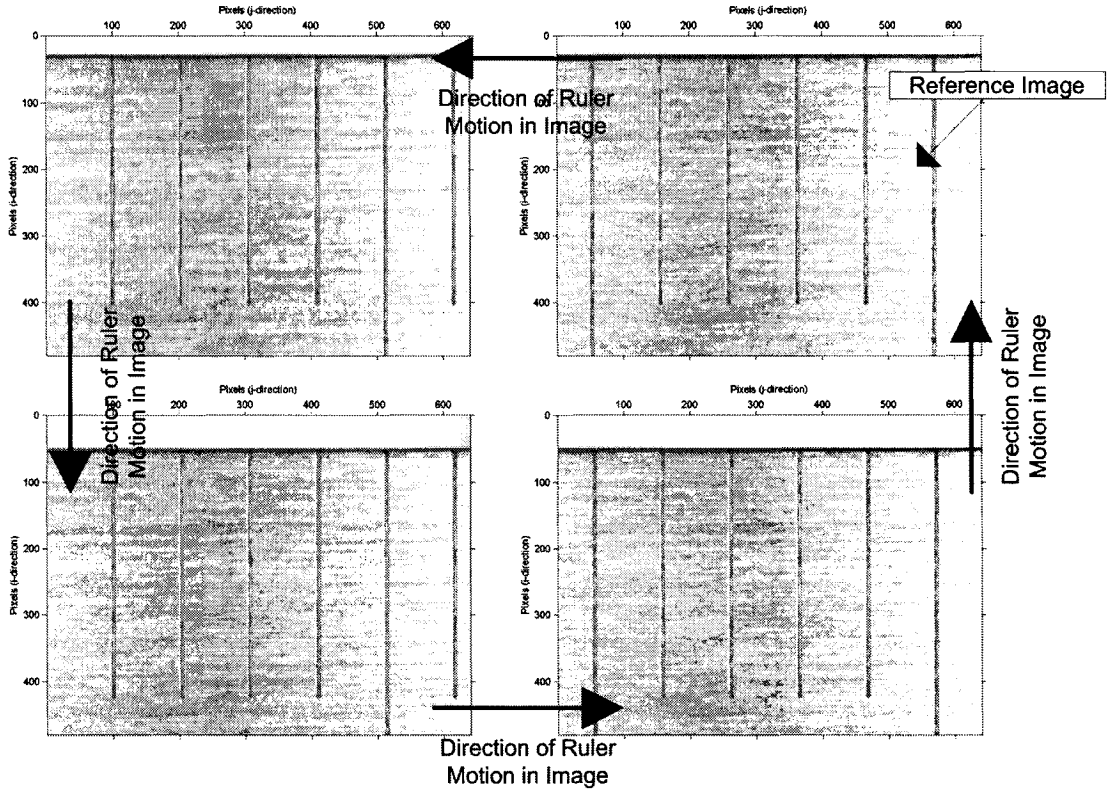

Figure 4.3: Four images illustrating the maximum displacement of the calibration pattern.

the error in the initial measurement is not properly considered and the representative measurement point is made to be the origin for all subsequent measurements. It can be noted that the error between subsequently computed actual and theoretical data points is large. In Figure 4.4(b), it is assumed that this initial measurement contains error. The location of the reference image origin is fit to the data in a way that reduces this error. This origin fitting offers a more accurate measure of the error incurred by all measurements.

The process of fitting an origin to the measured data begins by dividing the measured data into four discrete segments. These four sets of data points represent the four sides of the rectangular calibration pattern. It can be noted that two of these sets correspond to vertical lines and two of the sets represent horizontal lines. The first consideration is given to the data representing vertical segments. These two segments generally represent

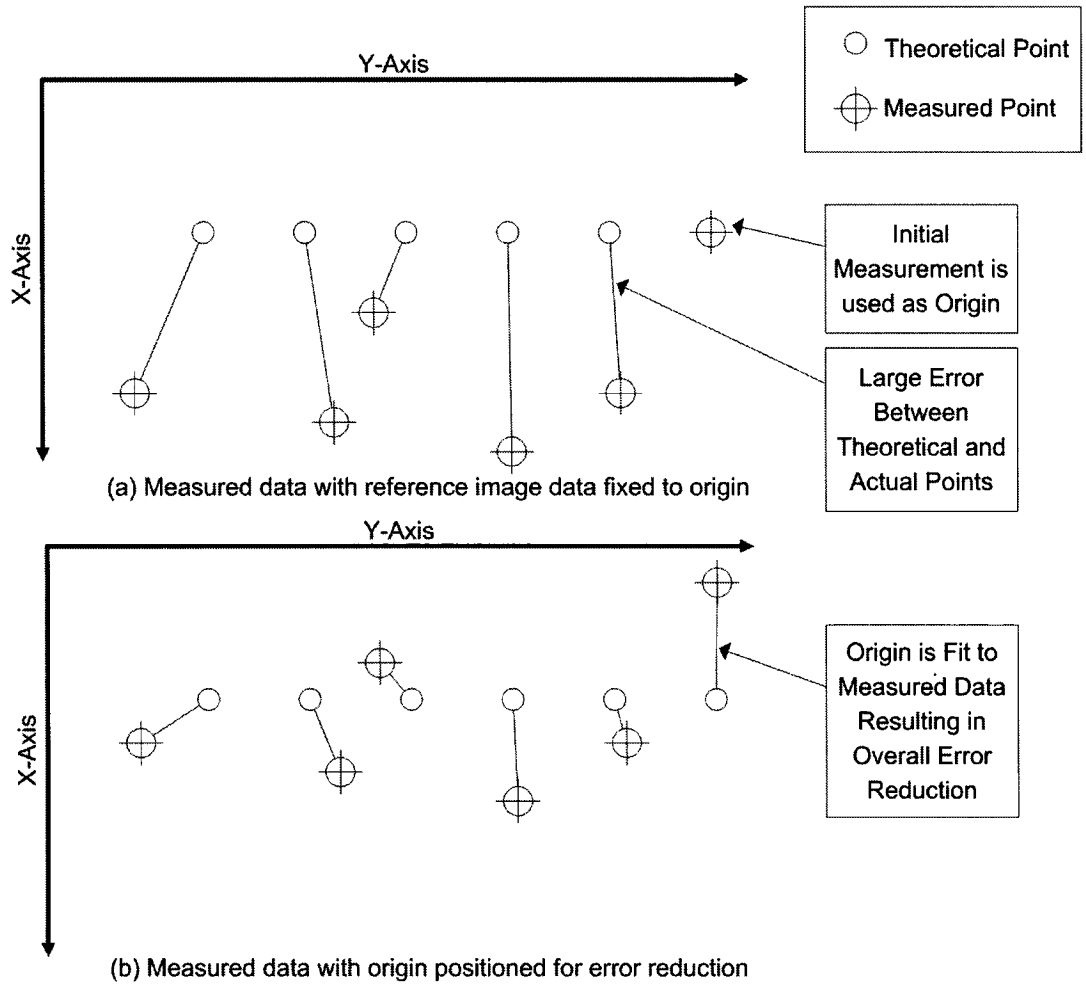

Figure 4.4: Effect of using measured data in determining the origin of relative measurements.

the horizontal displacement of the measurement artifact. One set of data passes vertically through the origin point of the calibration pattern and the other set represents a vertical line expected to be positioned 558.8 μm in the $-Y$ direction. In order to obtain a good estimate of the position of the origin, both of these sets of data must be included. The horizontal displacement of this second set of data prevents this combination. By re-positioning each point in the second set of data by a magnitude of 558.8 μm in the $+Y$ direction, these two sets of data points represent lines that are now collinear. These two sets of data are combined and a line of *best fit* is applied to the data using linear regression. The equation

of this line represents the line that passes through the origin of the calibration pattern as determined by the vertical data. A similar procedure is then performed using the two sets of horizontal data. One set is shifted by 203.2 μm in the $-X$ direction and combined with the other set using linear regression. This combination results in the line that passes through the origin of the calibration pattern as determined by the horizontal data. The system of equations consisting of the two aforementioned lines is solved. The resulting point of intersection is used as the origin point of the calibration pattern.

A diagram of a typical comparison of image data to actual data can be viewed in Figure 4.5. In this figure, data points extracted using image processing are marked with a plus (+) sign. The points, as measured using the Vernier $X - Y$ table, are marked with small circles (o). The lines between the markers represent the error between each image point and the actual point. The lengths of these lines are used in determining the resolution of the measurements. There are a number of other significant pieces of information that can be used to describe the measurements that this measurement system produces. This information is described in Section 4.2 in order to optimize the algorithm.

4.2 Parametric Study of Image Processing Algorithm

The discrepancy in values between the image data points and Vernier Table points is partially a result of the resolution of the Vernier Table, but mostly a result of poor optimization of the image processing algorithm. There are several parameters within the body of the algorithm that must be properly selected in order to increase the measurement resolution of the algorithm. A measure of the resolution of the algorithm was presented in the Section 4.1. Using this procedure, the algorithm can now be improved through the use of an algorithm calibration procedure. This calibration procedure consists of altering one parameter in the algorithm at a time and then performing the validation procedure

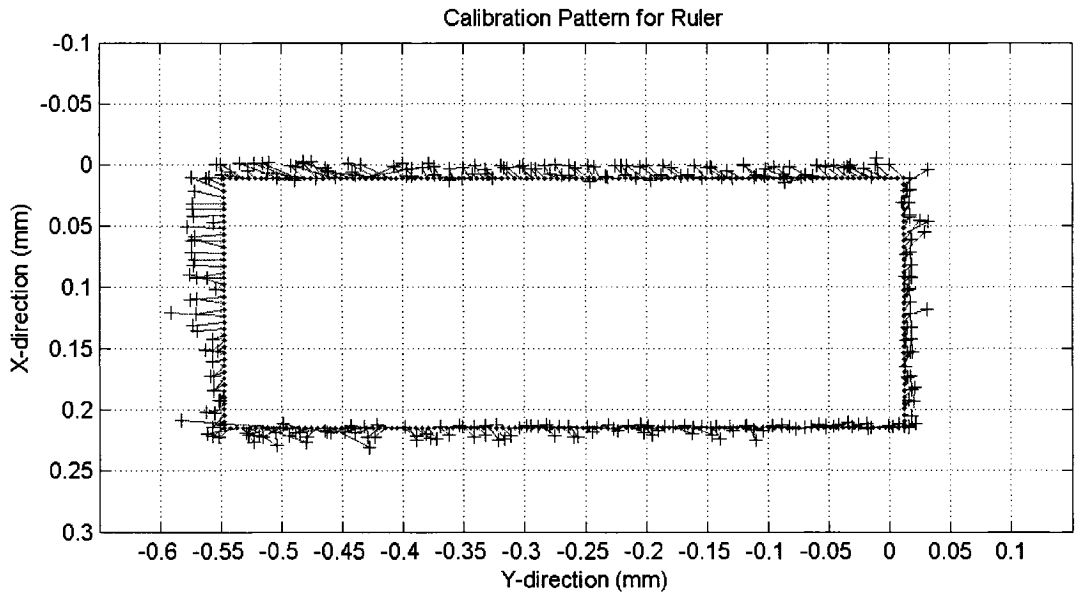

Figure 4.5: Typical comparison between actual and measured data.

to establish the effects of this alteration. The end result is an observed increase or decrease in the mean and maximum error produced by the readings. Based on all of the information describing the algorithm, parameters are selected. The actual effects of altering the parameters associated with the several steps in the algorithm are discussed in the following sections. The measurements produced using each of the two post-processing algorithms are observed. Relative measurements characterized by the removal of perspective distortion are described in Section 3.5.1. The measurements resulting from this type of post-processing are referred to as PT data. The second type of post-processing, described in Section 3.5.2, is characterized by the use of features within each image to directly scale and orient the data and provide relative measurements. The measurements resulting from this type of post-processing are referred to as IS data.

4.2.1 Noise Filter Selection

There are four types of filters that are considered for use in this image processing algorithm. The theory behind each of these four filters is described in Section 3.3.2. Using the validation process outlined in Section 4.1, many sets of data are generated for the purpose of comparing these four filters. The data sets are generated using both of the post-processing algorithms described in Section 3.5 and so two sets of data are generated for comparison of each filter. Figure 4.6 illustrates the validation of PT data resulting from the absence of any noise filter. This data consists of the locations of theoretical data points, the locations of measured data points and a set of lines indicating the distance between these points. There are several qualitative observations that can made from this figure. First, one can observe the typical error between measured data points and theoretical data points. It appears that this error is less than ± 0.069 mm, which is a measure of the success of the image processing algorithm. The actual design requirement is significantly less. Secondly, it appears that the measured data points have a definite directional bias in their deviation from the actual points. Considering the Y direction, the measured data points appear to clump together in groups at every 0.05 mm increment in the controlled displacement. The amount of deviation in the X direction appears to be related to that of the Y direction. For all measured points located in the $-Y$ direction from the actual point, the error in the X direction is positive. The X deviation is negative for all measured points located in the $+Y$ direction from the actual point.

Figure 4.6 can be compared with Figure 4.7. This figure contains the data resulting from the same validation process, but using the IS data. Upon comparison of these two figures, one can observe that the clumps of data points no longer exist. The measured points are evenly spread along the theoretical data points. This comparison suggests that the data clumping is a result of some portion of the PT post-processing procedure. Figure 4.7 also illustrates that a small directional bias still exists in the measured data.

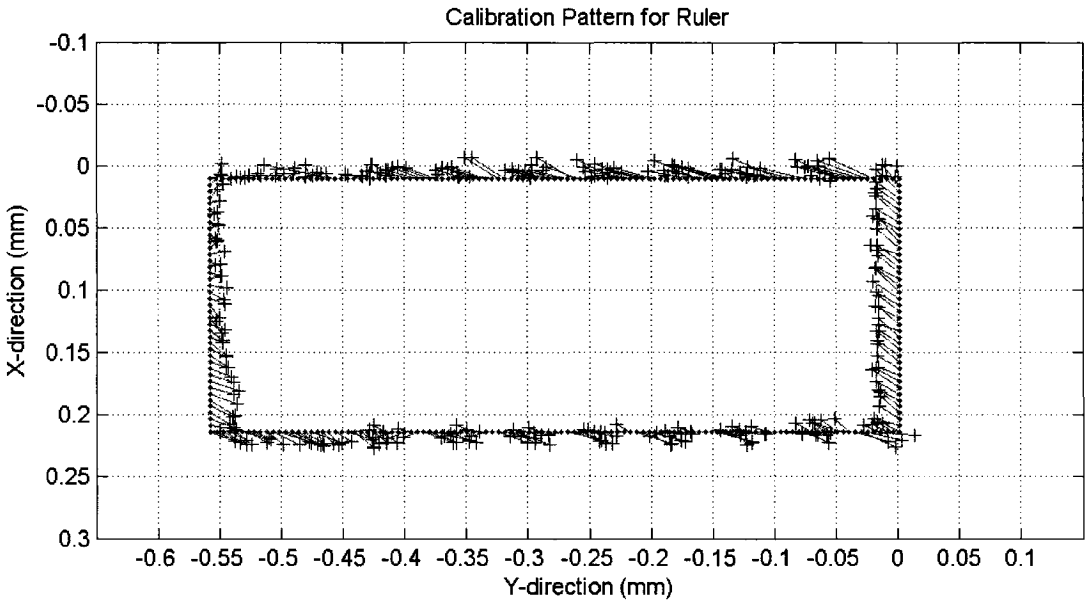

Figure 4.6: Measurement validation using PT post-processing.

A comparison between the effects of using each of the four filters is generated by substituting each filter into the image processing algorithm and then using this modified algorithm in the validation procedure. This comparison is represented qualitatively in

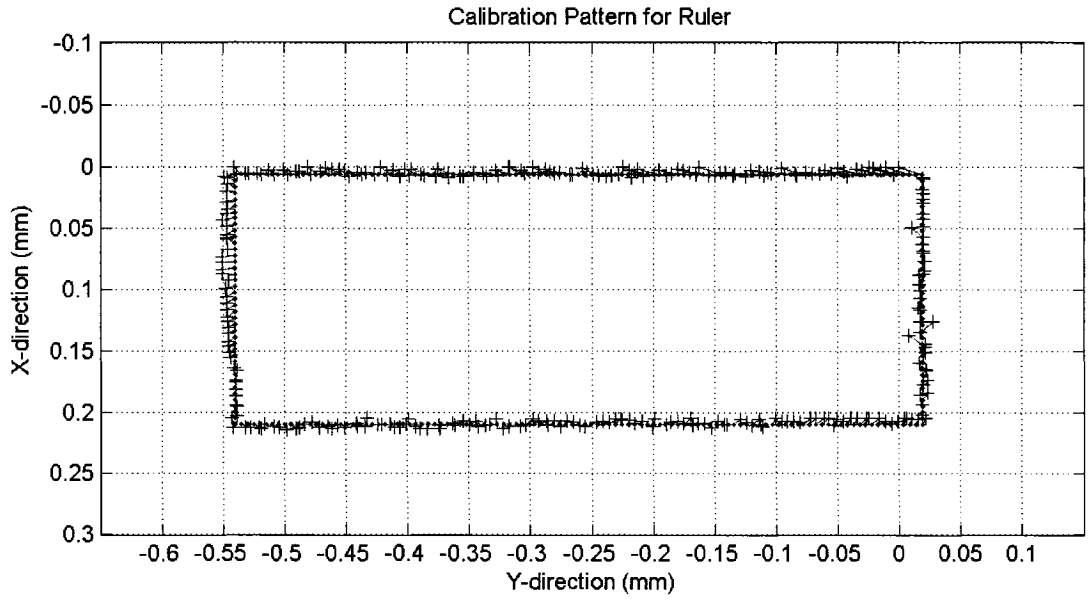

Figure 4.7: Measurement validation using IS post-processing.

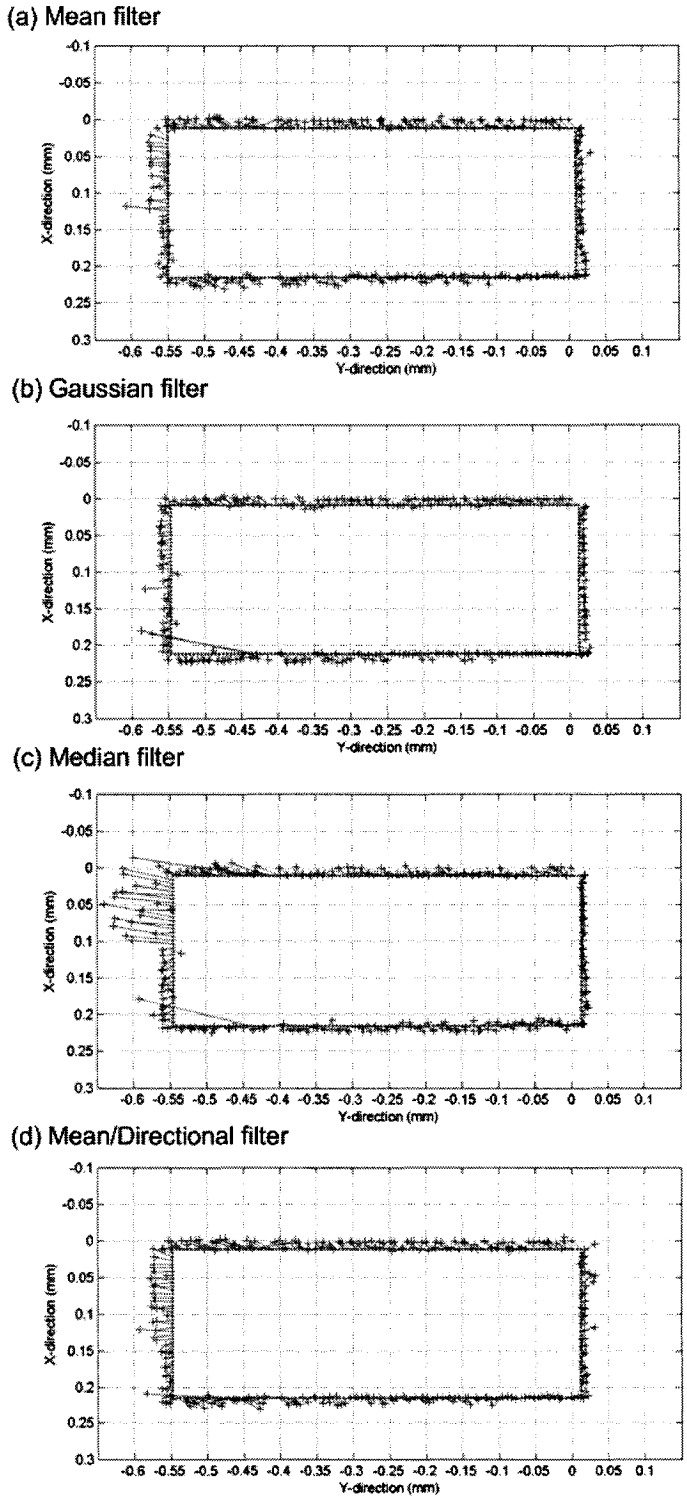

Figure 4.8: Measurement validation comparing the four noise filters using PT data.

Figure 4.8 using the PT data. In this figure, it appears that several of the filters allow fairly poor measurements to be magnified through the use of PT post-processing. The poorest result from these filters is illustrated in Figure 4.8(c). The median filter allows numerous larger measurements to propagate through the algorithm and degrade the result achieved through the use of this filter. This result can be compared to the plots displayed in Figures 4.8(b) and 4.8(d). Both of the filters used to generate these figures offer an improvement in the average and maximum measurement error over the median filter, although some erroneous measurements are still present. It can be noted that the actual implementation of the directional filter requires the use of both the mean filter and the directional filter. The mean filter is used to filter data to be used in the processing of the horizontal edge and the directional filter is used to filter data to be used in the processing of the vertical graduations. Both filters are required since the grain on the surface of the measurement artifact is horizontally biased. The best result of this comparison is visible in Figure 4.8(a). The mean filter provides both a low average error and a low maximum error in the measured data. For this reason, the mean filter is selected as the noise filter to be implemented in this image processing algorithm.

The same four filters can be compared using IS data. Based on the results displayed in Figure 4.9, it can be noted that all of the measurements produced using the IS data offer an improvement over the results produced using the PT data. There are small differences in the results produced by each individual filter using the IS data, but these differences are not enough to drive the selection of a different filter. A summary of the data used in the selection of a noise filter is available in Appendix C.

4.2.2 Segmentation Parameters

There are two parameters listed in Section 3.3.5 that are used to describe the segmentation of features from an image. These parameters control the width ($TestWidth$) and height

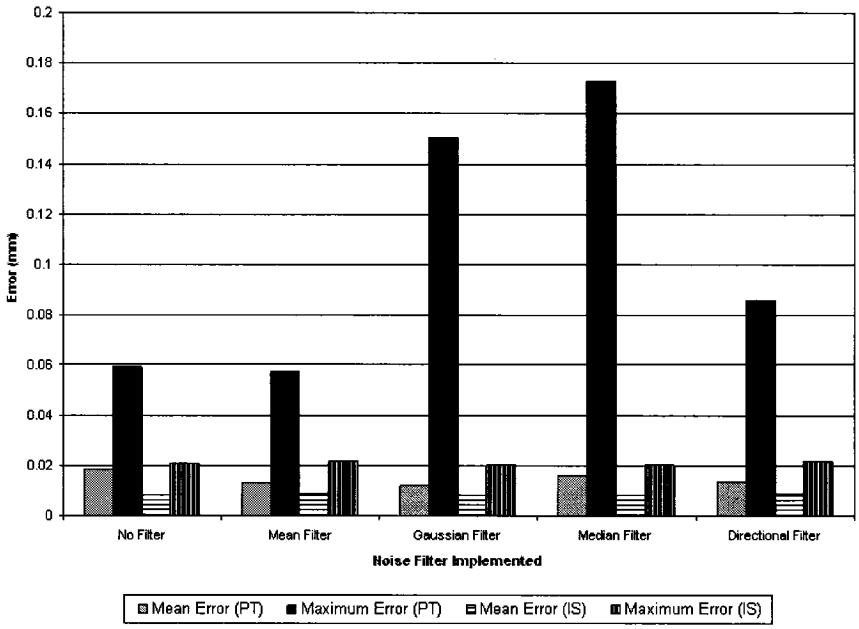

Figure 4.9: Direct comparison between error resulting from the use of each noise filter.

($TestHeight$) of the segmentation window referred to as the **Test Box**. This window is used to define an area in which pixels are able to contribute to the selection or elimination of a central pixel to the feature under segmentation.

By increasing the parameter $TestHeight$, pixels located a greater distance off of the feature under segmentation will influence the selection of pixels. Many pixels that surround an edge can be used to provide relevant information required for the selection of edge-pixels. The off-pixel distance that should be used for pixel selection is determined through this parametric study. Figure 4.10 summarizes the effect that altering this parameter has on the measured data points. The data used to produce this figure is available in Appendix C. The results displayed in Figure 4.10 indicate that distant off-edge pixels should not be used in the segmentation of features. As the parameter $TestHeight$ is reduced from a value of 20 pixels to 2 pixels, both the average and maximum measurement error for the IS and PT data is improved. Based on these results, 2 pixels is selected as the $TestHeight$ parameter.

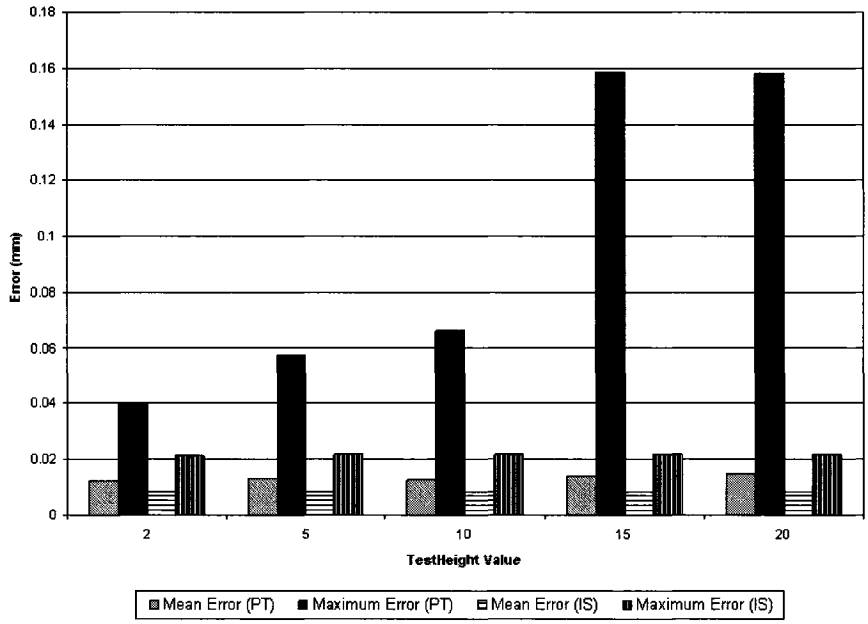

Figure 4.10: Direct comparison between error resulting from the use of different *TestHeight* parameter values.

The parameter *TestWidth* is used to control width of the *TestBox* window. The width of this window is generally aligned with the length of the edge under segmentation. By controlling this width, one can expand the window along the length of the edge. The significance of this expansion is that the segmentation procedure is able to use the pixels located further along the edge in determining if a pixel should be captured as part of the edge. If the *TestBox* window considers pixels located a value *TestWidth* to the right of the pixel under consideration and observes some irregularities in these pixels, perhaps the pixel currently under consideration is not a good representation of the edge and should not be selected. The window is also able to look to the left of the pixel under consideration. This *pixel foresight* is used to avoid irregularities, graduation end-points and the intersection between the vertical graduations and the horizontal edge. The actual distance that the segmentation should be looking is determined with a parametric study. Figure 4.11 illustrates the results of such a study. The data contained in this figure is also

available in Appendix C.

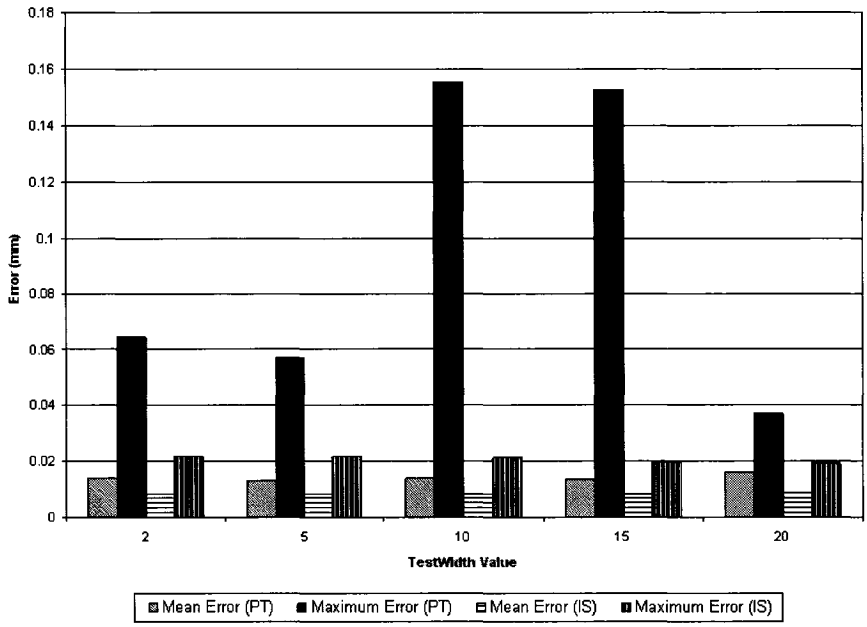

Figure 4.11: Direct comparison between error resulting from the use of different *TestWidth* parameter values.

The data in Figure 4.11 indicates that the relationship between the measurement error and the parameter *TestWidth* is fairly complicated. Considering only the maximum error values, a *TestWidth* parameter of 20 results in the lowest value for both the *PT* data and the *IS* data. This is an indication that a *TestWidth* parameter of 20 results in the best suppression of large erroneous measurements. Considering only the average error values, a *TestWidth* parameter of 5 results in the lowest average measurement error for the *PT* data and a parameter value of 2 results in the lowest average measurement error for the *IS* data. This relationship further is complicated by the large maximum error values for the parameters that lay in between. These maximum error values are used to indicate the worst possible case of an error measurement, but the average error value is a better indicator of the overall quality of the data. As a result, the parameter *TestWidth* will be set to a value 5 for the final image processing algorithm. The errors resulting from setting

TestWidth equal to a value of 5 are better than those resulting from the parameter 2 in three of the four categories, although all errors are similar. Setting this parameter should have the best overall effect on the algorithm.

4.2.3 Correlation Coefficient Parameter

The linear correlation coefficient for a set of data is determined after each individual line is extracted from an image. The set of data for a line consists of one array of i and j coordinates. A sub-pixel moment calculation is used to increase the resolution of these coordinates. The next step in the algorithm is to filter out a number of these coordinates in order to straighten each line. The segmentation procedure selects pixels that are supposed to belong on each vertical graduation of the image. The actual selection of these pixels can be hindered as a result of image noise and surface irregularities. Since each set of edge data is supposed to describe a precision-machined straight edge, this linear expectation is used in order to filter out coordinates that are less likely to belong on the edge. Each line is corrected up to a minimum linear correlation coefficient that is controlled by the parameter *LCCMin*. Initial testing indicates that this parameter can be set to a minimum value of 0.8 and allow the algorithm to process images. A parameter value set below 0.8 results in extremely large errors propagating through the algorithm. Figure 4.12 illustrates the results of increasing this parameter beyond the nominal value of 0.8. The data contained in this figure are also available in Appendix C.

The most notable result of this comparison is the change in the value of maximum error using *PT* data between parameter values 0.8 and 0.82. These results indicate that lines that are filtered to a minimum linear correlation coefficient of greater than 0.8 offer a poor representation of the actual edge when compared to those resulting from a minimum coefficient value of 0.8. Based on this comparison, the parameter value 0.8 is set as the value of *LCCMin* for use in this image processing algorithm.

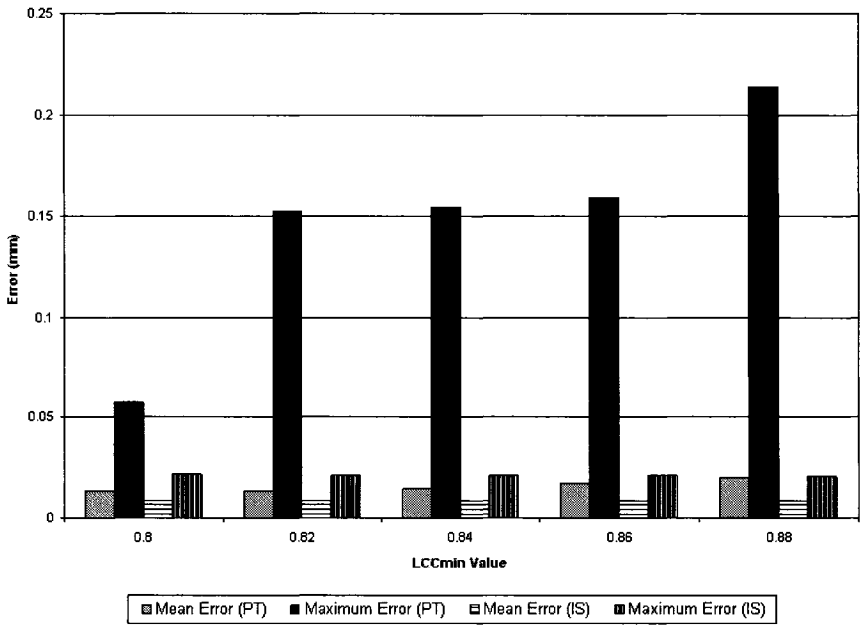

Figure 4.12: Direct comparison between error resulting from the use of different *LCCmin* parameters values.

4.2.4 Post-Processing Calculations

There are two methods of post-processing that must be considered. The first method uses the calculation of a homogeneous transformation matrix in order to eliminate linear projective distortion from the images. After the calculation of all transformed coordinates in a set of two images, these two sets of data are compared and the displacement is computed. The process of comparison between two sets of image data is described in Section 3.5.1. In general, the displacements measured between two images are distributed as shown in Figure 4.13. Both sets of data appear to cover a large range of displacements. The magnitude of these displacements appears to depend on the theoretical distance between each set of points. Using the calculation described in Section 3.5.1, a point along the horizontal edge of the ruler can be compared with a point located on one of the vertical graduations in order to produce a relative displacement. As the distance between these two points increases, the measured displacement appears to increase.

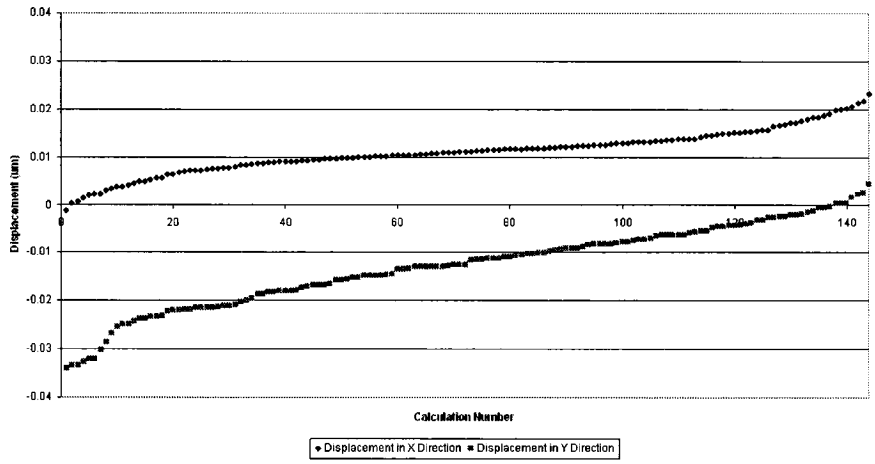

Figure 4.13: Spectrum of displacement measurements in both the X and Y directions resulting from the comparison of two images.

It can be noted that the average displacement in the X direction as indicated by this data is a value of 0.00504 mm and the average displacement in the Y direction is -0.00615 mm. The theoretical displacement values are 0.005 mm and -0.005 mm in the X and Y directions, respectively. It is possible to improve these displacement estimations by eliminating the displacements that exist at either end of the spectrum of displacements. For example, ten percent of the largest displacements and ten percent of the smallest displacements can be eliminated from the data of Figure 4.13 resulting in the average displacements of 0.00472 mm and -0.00530 mm in the X and Y directions, respectively. The measure of error in one direction improves, while the measurement of error in the other direction worsens. This example only considers the displacement of one point. A large set of points must be considered in order to obtain a better indication of the effect of altering this parameter. Figure 4.14 illustrates the overall effect of altering the percentage of data eliminated from each image comparison using the procedure of Section 4.1. The data presented in this figure is also available in Appendix C. A percentage is used for the purpose of indicating the amount of eliminated data because each image can contain varying numbers of points of calculation and, therefore, varying amounts of data.

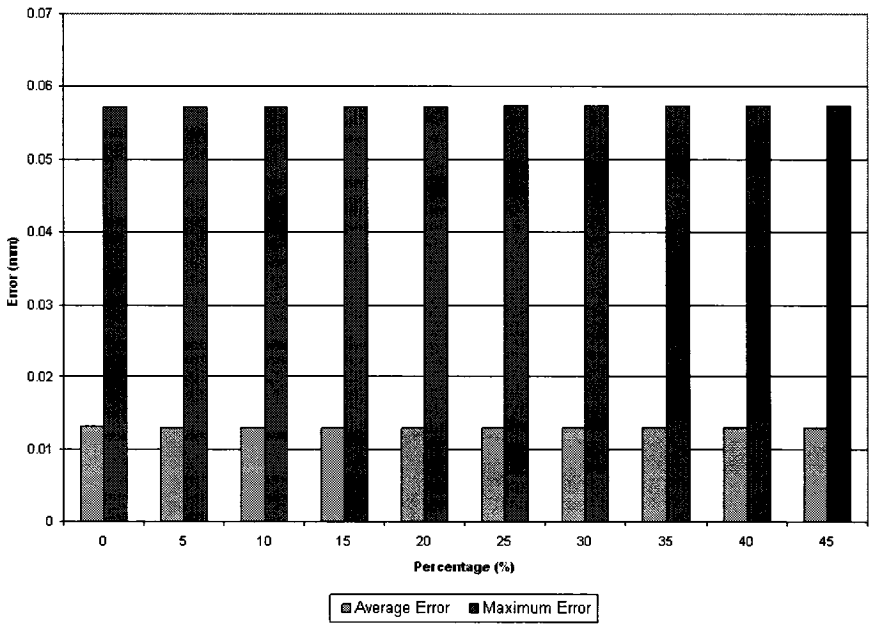

Figure 4.14: Comparison of error resulting from the use of different quantities of data.

It is difficult to visually determine the best percentage of eliminated data from Figure 4.14 because the effects on the measurement error are subtle. According to the data in Table C.5, the measurement error is reduced the most when ten percent of the largest and smallest displacement measurements are eliminated from the calculation of the displacement between two images. This value is selected as the parameter to be used in this image processing algorithm.

4.2.5 Summary of Final Parameters

Table 4.1 lists all of the parameters discussed in Section 4.2 along with the value selected for each. It can also be noted that the resolution of the measurements provided by the IS data are generally better the resolution of the measurements provided by the PT data. It is recommended that the IS post-processing algorithm be implemented in this relative measurement system.

Table 4.1: Summary of all parameters selected for use in this image processing algorithm.

Name of Parameter	Final Value
Noise Filter	Mean Filter
$TestHeight$	2
$TestWidth$	5
$LCCMin$	0.8
Percentage Data Removed	10

4.3 Characterization of Relative Measurements

The success of this image processing algorithm is determined by comparing the resulting relative measurements with the design requirements discussed in Section 2. These requirements judge the algorithm based on both its accuracy and its functionality because these are the characteristics that are required in order for this algorithm to apply to the camera-based calibration system for which it was designed.

The first requirement of this system is the resolution of the measurements. The requirement states that this error should be an order of magnitude less than the repeatability of the robot end-effector. This repeatability is stated in Section 2.1.1 as being ± 0.069 mm. Based on the parameters described in the previous section, the maximum error that any relative measurement will produce is ± 0.057 mm using the PT data. The average error in measurements is stated as ± 0.013 mm using the PT data. The measurement error resulting from the use of IS data is considerably smaller. This data results in a maximum and average error of ± 0.022 mm and ± 0.008 mm, respectively. Using both methods of post-processing, the characteristics of these relative measurements do not meet the design requirements. In the case of the IS data, the resultant mean error is extremely close to this requirement. A plot of the validation test applied with both types of post-processing can be seen in Figure 4.15. The soft requirement for the resolution of measurements is

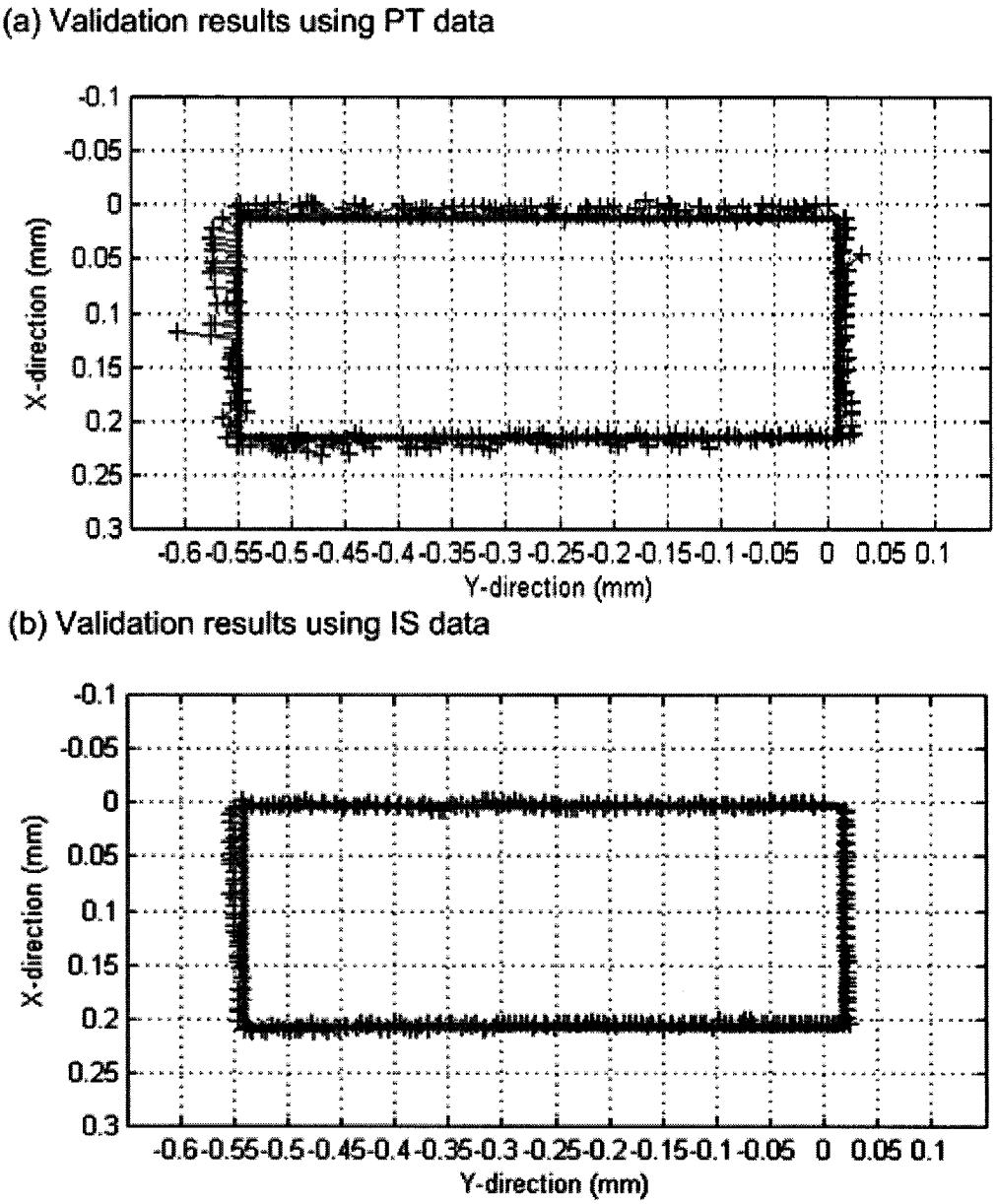

Figure 4.15: Measurement validation using the final image processing algorithm.

stated as ± 0.005 mm. It can be noted that the average error using the IS data is the closest value to this requirement. It is believed that, based on the selection of system components, this system should be able to reach the high resolution in relative measurements that are required in order to apply these measurements to the camera-based robot calibration scheme outlined in Section 1, although some further testing regarding the ac-

tual calibration process is required in order validate this hypothesis. Some suggestions for improving the resolution of these measurements are presented in Chapter 5.

The functionality of the algorithm describes the environment over which this system can be applied. In Section 2.2, several requirements for the functionality of this algorithm are presented.

The first requirement of the functionality of the system is its ability to produce relative measurements in the X direction up to a maximum displacement value of ± 0.7 mm. Figure 4.16 illustrates the measurement of the displacement of the measurement artifact in both the $+X$ and $-X$ directions. This figure illustrates that this algorithm is able to extract measurements that are greater than those required by the system. The artifact is displaced a maximum value of ± 0.8 mm.

The second requirement of the functionality of the system is its ability to extract measurements in the Y direction up to a maximum displacement value of ± 0.4 mm.

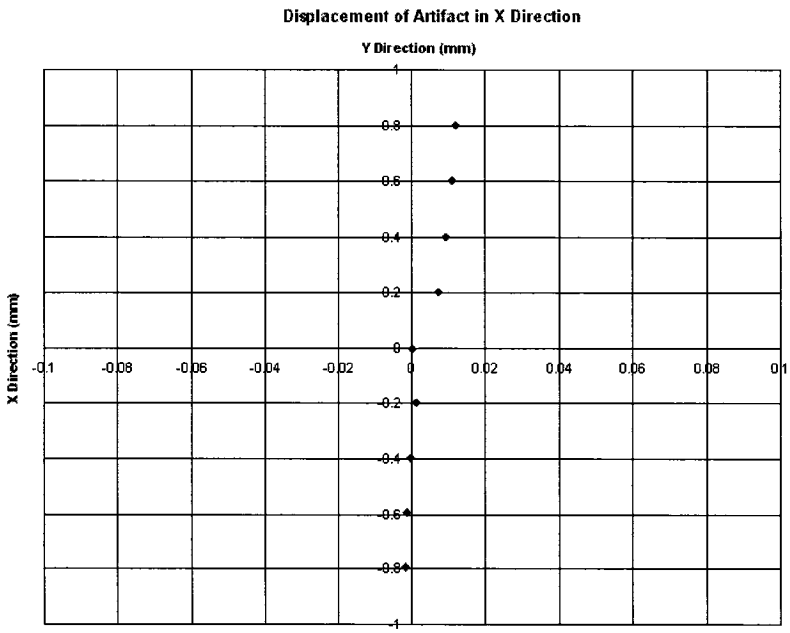

Figure 4.16: Displacement of the measurement artifact in the X direction.

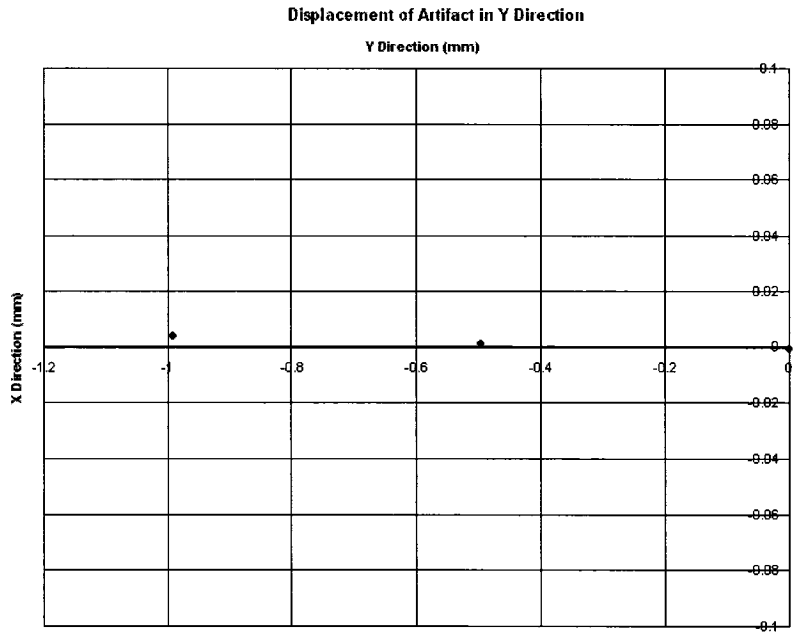

Figure 4.17: Displacement of the measurement artifact in the Y direction.

Figure 4.17 illustrates the measurement of a typical displacement in the Y direction. Two displacements are illustrated in this figure. The actual displacements consist of two 0.5 mm motions in the $-Y$ direction. Since the images produced by displacing the artifact in either the $-Y$ direction and $+Y$ direction appear similar, only the $-Y$ direction is considered here. The data in this figure demonstrate that the image processing algorithm exceeds the design requirements in this respect.

Finally, the algorithm used in this calibration system must be able to extract measurements over a distance of at least ± 0.3 mm in the Z direction. The displacement of the artifact in the Z direction is not controlled using the $X-Y$ table since this table can only control displacements in the $X-Y$ plane. Instead, the robot is repositioned using the robot controller to four positions in the Z direction. It is understood that these displacements are not accurate, but they do allow the algorithm to process images of the artifact at various positions in the Z direction. The four data points in Figure 4.18 illustrate the

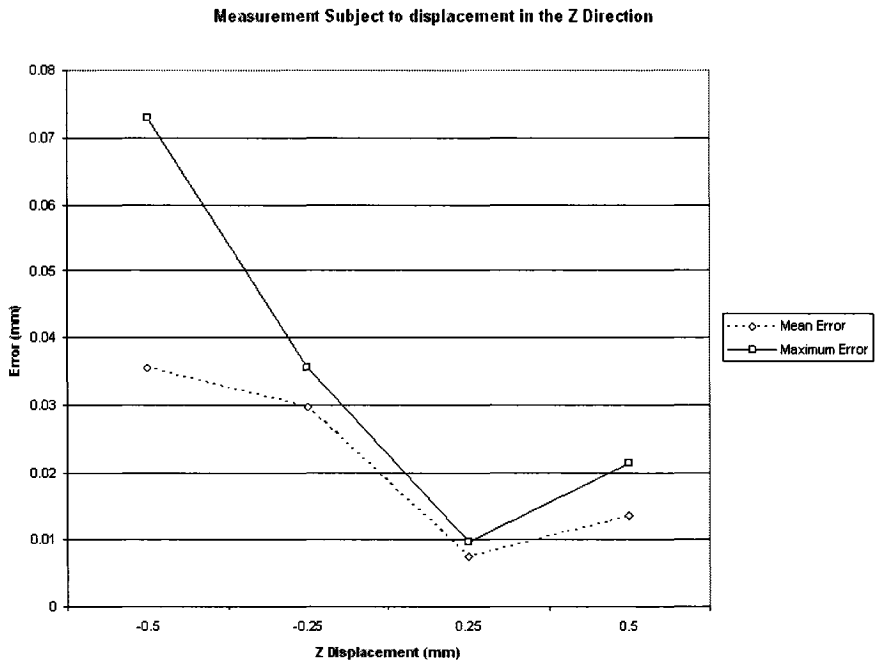

Figure 4.18: Measurement error produced by the calibration system subject to displacement in the Z direction.

robot-controlled displacement of the measurement head to 0.25 mm, 0.5 mm, -0.25 mm and -0.5 mm. At each of the four positions, the measurement artifact is displaced to five positions spanning both directions of the $X - Y$ plane. The displacement of these five positions are measured and used to produce a mean and maximum error value for each Z displacement. Based on the results of Figure 4.18, it appears that the measurement error is dependant on the position of the end-effector in the Z direction. The algorithm is able to produce measurements spanning a displacement of at least ± 0.5 mm, but the error in these measurements increases as the Z displacement is increased. In order to further quantify this dependency, the displacement in the Z direction should be controlled using some external device. This calibration system is operational over a distance of ± 0.5 mm and so this requirement is exceeded.

Chapter 5

Conclusions and Recommendations

This thesis outlines the development of a camera-based calibration system from equipment selection to measurement validation. Based on the validation results in Section 4.3, the design of this algorithm meets the design requirements set forth in Section 2. An attempt can be made to apply this algorithm to the calibration scheme outlined in the introduction, but the results of this application are uncertain since the actual resolution of the measurements are slightly worse than the suggested order of magnitude greater than the robot repeatability. This algorithm presents two methods of post-processing that are available for processing data. The first method, referred to as *PT* post-processing, uses a homogeneous transformation to remove perspective distortion from all image data. This transformation also scales the image data so that measurements can be directly extracted. The main disadvantage of this transformation is that it requires accurate knowledge of the artifact from which measurements are extracted. The manufacturer suggested that the lengths of the vertical graduations on the measurement artifact that are used to produce the projective transformation matrix can vary by up to 0.2 mm along the length of the ruler. This variation in length is likely the cause of the larger errors magnified during the *PT* post-processing procedure. The second method, referred to as *IS* post-processing,

does not require knowledge of the lengths of vertical graduations. As a result, the error in measurements resulting from the use of this procedure is reduced. This method of post-processing is highly dependant on the orientation of the camera. For the calibration scheme for which this camera-based measurement system is developed, the orientation of the camera will only stray within the nominal vertical orientation repeatability and this method can be applied.

Figure 5.1 illustrates the use of relative measurements in characterizing the deviation in robot end-effector position along a linear path. Because these are programmed motions, these deviations are due to the robot positioning accuracy.

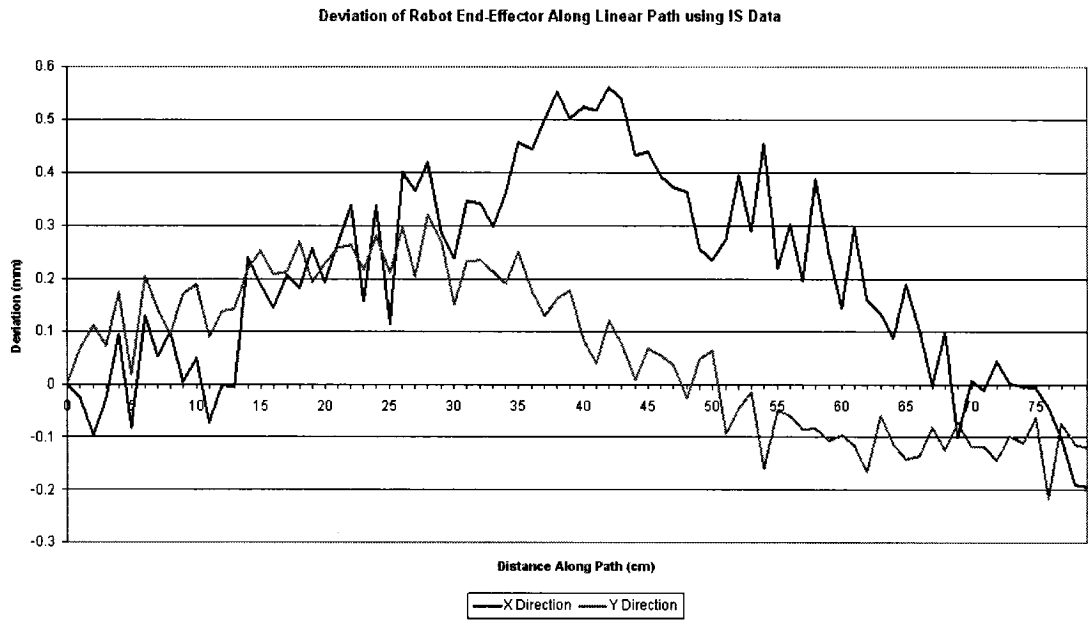

Figure 5.1: Measured position of the robot end-effector in the $X-Y$ plane at discrete points along a theoretically linear path.

The device used for the purpose of displacing the ruled surface in Section 4.1 is an $X-Y$ table. This table is able to displace the measurement artifact in two directions, but no tolerance for the orthogonality of these two directions is available. A small deviation from the desired two directions (X and Y) may have limited the resolution of measure-

ments produced using this device. Further work regarding the validation of this relative measurement scheme might involve the use of some high-resolution digital displacement device. A device that could also control the orientation of the measurement artifact would allow for further characterization of the image processing algorithm.

The lens used in this calibration system is the Rodenstock 1x Macro lens. This lens allows each pixel on the CCD chip to view an area of approximately 0.01 mm^2 on the surface of the measurement artifact based on the geometry of the camera, lens and artifact in the robot workspace. The selection of this lens is primarily based on its coverage area. The lens is able to view the full length of vertical graduations on the surface of the measurement artifact. A Rodenstock 2x Macro lens can be use to reduce the area viewed by each pixel. Using the 2x magnification, each pixel would view an approximate area of 0.005 mm^2. This increase in viewing resolution would also result in an increase in the resolution of measurements produced by the system. One problem that arises from the selection of the Rodenstock 2x Macro lens is the lack of any algorithm for the removal of perspective distortion. The algorithm described in this paper requires the full length of the vertical graduations on the measurement artifact to be observed in each image. The use of this lens with higher magnification prevents the full length of vertical graduations from appearing in any image. Also, this higher magnification would allow the machined tolerance of the measurement artifact (± 0.002 mm) to play a more prominent role in limiting the resolution of the measurements. Consideration would have to be give to the selection of alternate measurement artifacts with higher machined tolerance values.

The resolution of the CCD chip used in this calibration system is limited to 480×640 pixels. The actual resolution of the CCD chip is slightly higher, as explained in Section 2.1.2. There are several rows and columns of pixels that are disregarded. The selection of a framegrabber card that does not limit the resolution of the system would result in images that view a larger overall area on the surface of the measurement artifact. This

larger surface area might contain at least one additional vertical graduation that could be used in producing the displacement between any two images. The addition of this graduation may result in a reduction in the measurement error produced by the system. The resolution of available CCD chips has increased dramatically over the past decade. A CCD chip with a resolution that is an order of magnitude greater than that of the chip selected for the purpose of this system could be used to increase the resolution of the system. This increase in resolution would reduce the measurement error by allowing each pixel to view a smaller area on the surface of the measurement artifact. The increase in resolution would also increase the effects of noise in the image data and might limit the resolution of these measurements.

The displacement of the robot end-effector in the Z direction requires the use of a laser distance sensor. This sensor must be integrated to the current measurement head and configured to extract the displacement of the robot end-effector in the Z direction. The use of this sensor might require a smooth surface reference object from which to measure Z displacement. The measurement error produced by this Z measurement should not exceed that of the measurement error in the X and Y directions.

A cost analysis containing all of the aforementioned component upgrades should be performed in order to evaluate the feasibility of each. This camera-based calibration system must remain low in cost relative to all of the alternative calibration systems in order to be considered as a feasible alternative.

References

[1] A.A. Fratpietro and M.J.D. Hayes. Relative measurement for kinematic calibration using digital image processing. *Proceedings of the CSME Forum 2004*, pages 758–767, 2004.

[2] A.A. Fratpietro, N.W. Simpson, and M.J.D. Hayes. Advances in robot kinematic calibration. Technical report, Carleton University, 2003.

[3] A.A. Fratpietro and M.J.D. Hayes. Digital image processing applications of robot calibration. *Proceedings of the 19th Canadian Congress of Applied Mechanics*, 2003.

[4] M. Abderrahim and A.R. Whittaker. Kinematic model identification of industrial manipulators. *Robotics and Computer Integrated Manufacturing*, 16:1–8, 2000.

[5] Alberto Omodei, Giovanni Legnani, and Riccardo Adamini. Calibration of a measuring robot: experimental results on a 5 dof structure. *Journal of Robotic Systems*, 18(5):237–250, 2001.

[6] Hanqi Zhuang, Zvi S. Roth, Xuan Xu, and Kuanchih Wang. Camera calibration issues in robot calibration with eye-on-hand configuration. *Robotics and Computer-Integrated Manufacturing*, 10(6):401–412, 1993.

[7] Christophe Garcia. Fully vision-based calibration of a hand-eye robot. *Autonomous Robots*, 6:223–238, 1999.

[8] Jose Mauricio S.T. Motta, Guilherme C. de Carvalho, and R.S. McMaster. Robot calibration using a 3d vision-based measurement system with a single camera. *Robotics and Computer-Integrated Manufacturing*, 17:478–497, 2001.

[9] Jack Jeswiet and Ray Helferty. Measuring robot repeatability: an application of ISO and ANSI standards. *Advanced Robotics*, 10(5):503–520, 1996.

[10] Chichyang Chen and Yuan F. Zheng. New robotic hand-eye calibration method by active viewing of a checkerboard pattern. *Proceedings of the IEEE International Conference on Robotics and Automation*, 2:770–775, 1993.

[11] H. Zhuang. Hand-eye calibration for electronic assembly robots. *IEEE Transactions on Robotics and Automation*, 14(4):612–616, 1998.

[12] Remy S. Dhome, J.M. Lavest, and N. Daucher. Hand-eye calibration. *IEEE International Conference on Intelligent Robots and Systems*, 2:1057–1065, 1997.

[13] Song De Ma. A self-calibration technique for active vision systems. *IEEE Transactions on Robotics and Automation*, 12(1):114–121, 1996.

[14] Dongmin Kim. Dual quaternion applications to kinematic calibration of wrist-mounted camera. *Journal of Robotic Systems*, 13(3):153–162, 1996.

[15] Reimar K. Lenz and Roger Y. Tsai. Techniques for calibration of the scale factor and image center for high accuracy 3-d machine vision metrology. *IEEE Transactions on Pattern Analysis and Machine Intelligence*, 10(5):713–720, 1988.

[16] Hanqi Zhuang and W-C. Wu. Camera calibration with a near-parallel (ill-conditioned) calibration board configuration. *IEEE Transactions on Robotics and Automation*, 12(6):918–922, 1996.

[17] R. Horaud and F. Dornaika. Hand-eye calibration. *International Journal of Robotics Research*, 14(3):195–210, 1995.

[18] Hanqi Zhuang. A note on hand-eye calibration. *International Journal of Robotics Research*, 16(5):725–730, 1997.

[19] Guo-Qing Wei, Klaus Arbter, and Gerd Hirzinger. Active self-calibration of robotic eyes and hand-eye relationships with model identification. *IEEE Transactions on Robotics and Automation*, 14(1):158–166, 1998.

[20] M.J.D. Hayes and P.L. O'Leary. Kinematic calibration procedure for serial robots with six revolute axes. Technical report, Institute for Automation at the University of Leoben, 2001.

[21] N.W. Simpson. *Kinematic calibration of 6-axis serial robots using the relative measurement concept.* Carleton University, 2004.

[22] N.W. Simpson and M.J.D. Hayes. Kinematic calibration of industrial manipulators. *Proceedings of the 19th Canadian Congress of Applied Mechanics*, 1:180–181, 2003.

[23] N.W. Simpson and M.J.D. Hayes. Simulation of a kinematic calibration procedure that employs the relative measurement concept. *Proceedings of the CSME Forum 2004*, pages 62–71, 2004.

[24] K. English, M.J.D. Hayes, M. Leitner, and C. Sallinger. Kinematic calibration of six-axis robots. *Proceedings of the CSME Forum 2002*, 2002.

[25] Ronald Ofner, Paul O'Leary, and Markus Leitner. A collection of algorithms for the determination of construction points in the measurement of 3-d geometries via light-sectioning. Technical report, Institute for Automation at the University of Leoben, 1998.

[26] Ramesh Jain, Rangachar Kasturi, and Brian G. Schunk. *Machine Vision.* MIT Press and McGraw-Hill, 1995.

[27] Robert K. Sleeper and Eunice G. Smith. A transformation method for deriving, from a photograph, position and heading of a vehicle in a plane. Technical report, NASA Langley Research Center, 1976.

[28] Yael Edan, Lea Friedman, Avraham Mehrez, and Leonid Slutski. A three-dimensional statistical framework for performance of robotic systems. *Robotics and Computer-Integrated Manufacturing*, 14:307–315, 1998.

[29] Kevin L. Conrad and Panayiotis S. Shiakolas. Robotic calibration issues: Accuracy, repeatability and calibration. *Proceedings of the 8th Mediterranean Conference on Control and Automation*, 2000.

[30] A. Ito, Y. Aoki, and S. Hashimoto. Accurate extraction and measurement of fine cracks from concrete block surface image. *IEEE 2002 28th Annual Conference of the Industrial Electronics Society*, 3:2202–2207, 2002.

[31] D.D. Udrea, P. J. Bryanston-Cross, W.K. Lee, and M. Funes-Gallanzi. Two sub-pixel processing algorithms for high accuracy particle centre estimation in low seeding density particle image velocimetry. *Optics and Laser Technology*, 28(5):389–396, 1996.

[32] Ronald Ofner, Paul O'Leary, and Markus Leitner. A collection of algorithms for the determination of construction points in the measurement of 3-d geometries via light-sectioning. Institute for Automation at the University of Leoben, 1998.

[33] Saeed B. Niku. *Introduction to Robotics: Analysis, Systems, Applications.* Prentice Hall, 2001.

[34] Roberto Cipolla and Peter Giblin. *Visual Motion of Curves and Surfaces.* Cambridge University Press, 2000.

[35] G.D. van Albada, J.M. Lagerberg, A. Visser, and L.O. Hertzberger. A low-cost pose-measuring system for robot calibration. *Robotics and Autonomous Systems*, 15:207–227, 1995.

[36] M.J.D. Hayes, P.J. Zsomber-Murray, and A. Gferrer. largest ellipse inscribing an arbitrary polygon. *Proceedings of the 19th Canadian Congress of Applied Mechanics*, 2003.

[37] R.S. Figliola and D.E. Beasley. *Theory and design for mechanical measurements, 3^{rd} ed.* John Wiley and Sons, Inc., New York, N.Y., U.S.A., 2000.

Appendix A

Calibration Cost Analysis

Robotic manipulators perform a variety of tasks in automated processes. Many of these tasks require a high degree of accuracy in the kinematic model that the robot must maintain over the course of its working life. This can be a difficult task for the robot controller when one considers the constant wear, fatigue, and stress to which the robot will be subjected. In order to maintain an accurate kinematic model, the robot needs to be calibrated on a near-continuous basis. A low-cost system that allows the measurement and correction of error in the kinematic model without disturbing the robot from its work-related tasks would be ideal for this situation.

The camera-based robotic calibration system uses images of a precision-ruled surface taken from a measurement head attached to the robot end-effecter to identify the error in the kinematic model of the robot. An appropriate correction to the model is then fed back into the robot controller, resulting in a higher degree of accuracy.

The baseline calibration system consists of several components: a precision ruled surface of which images are produced, a flat standard used for measuring the distance between the ruled surface and the camera, a CCD camera and lens used to produce images of the ruled surface, a framegrabber PC card used for capturing images produced by the camera,

a light source used to illuminate the surface of the ruler, a distance sensor and associated data acquisition hardware used to measure distance between surface of the flat standard and camera, and a personal computer with the LabView or Simulink and MATLAB software for reading and processing the information that is produced by the rest of the system.

A.1 Scope of the Cost Analysis

Three different approaches are used in the preparation and presentation of the cost analysis for this camera-based robotic calibration system.

A.1.1 Engineering Approach

The engineering approach assumes that the analyst has an extensive knowledge of the entire system and of the operation of each of its separate components. The extensive knowledge required for this type of approach can be gained through studying operations manuals, experimenting with similar components, and other general research pertaining to each component.

A.1.2 Analogy Approach

The analogy approach assumes that information regarding a system similar to the one being analyzed is readily available and can be used as an analogue to the system under development. In the case of the camera-based robotic calibration system, a working prototype has been under development for several years and is used as a baseline for the current system under analysis.

A.1.3 Expert Opinion Approach

The expert opinion approach assumes that one or many individuals already have extensive knowledge of the system or system components. These individuals may have suggestions relating to their past experience regarding possible improvements to the system under development. Markus Leitner of Steinbichler worked on the previous iteration of the camera-based robot calibration system while at the Institute for Automation at the Mining University in Leoben, Austria, and is a knowledgable source of information for the current iteration.

A.1.4 Explanation of Currency

This analysis includes the costs associated with the purchasing of parts, delivery of parts, and integration and testing of the system. The costs of various parts are obtained from product catalogues, internet price lists, and through requests for quotes from the manufacturers or their distributors. An explanation of delivery and integration and testing costs is located in sections A.4 and A.5 of this report. It is possible that some assets for use in this system may be inherited from the Carleton University Department of Mechanical and Aerospace Engineering and other sources, but these assets remain in a state of uncertainty and will not be considered in this analysis. It can be noted that these assets may reduce the overall cost of the system.

All dollar values stated in this report are given in fiscal year 2003 constant Canadian dollars and as a result inflation is not considered.

A.2 Comparison of System Components

The camera-based robotic calibration system has several different components and each of these components should be evaluated separately. Each component evaluation consists of a

brief description of the component in question, a list of constraints with their explanations, a description of the baseline design, a summary table filled with possible alternatives to the baseline, and a comparison of these possible alternatives. Each evaluation is followed by a recommendation and reason for this recommendation.

There is an overall payload constraint on the weight of the fully equipped measurement head imposed by the payload of the robot being used for validation of the system. This constraint is a 2 kg maximum mass. Therefore, the combined mass of all components mounted to and including the measurement head must not exceed 2 kg. It is also necessary that the all devices requiring an electronic cable attachment between the measurement head of the calibration system and a port external to the robot workspace use a cable configuration that does not interfere with the movement of the robot. For this purpose, all cables attaching to the measurement head must be at least 5 m in length and will be fastened along the length of the robot from measurement head to robot base.

A.2.1 CCD Camera

The CCD camera is the transducer that converts an optical image of the ruled surface into a set of electrical signals that can be interpreted by a framegrabber PC card. This device is rigidly mounted to the measurement head and has its optical axis aligned in the negative z-direction of the robot tool-flange coordinate system. The CCD camera must successfully integrate with an optical lens and communicate with a PC framegrabber card.

There are six parametric constraints placed on the selection of the CCD Camera:

Colour- The use of colour is not required for the purpose of extracting metric information from digital images and can further complicate the procedure. Since cameras without colour regularly cost less than cameras producing coloured images, the selection of a CCD-Camera is restricted to black and white.

C-Mount Interface- There are several standard lens mount types that are common in industry. The most common for the purpose of attaching lenses to CCD-cameras in machine vision is the C-mount. An explanation of the C-mount is found in the appendix of this report. The selection of a CCD-camera is constrained to include a C-mount lens interface.

Analog- Analog cameras are typically cheaper and lighter then their digital counterparts. The selection of a CCD-camera is constrained to analog cameras.

Interlace scan- Interlace scan and progressive scan are two types of scanning that a CCD implements to produce images. A description of these scan-types can be found in the appendix of this report. The selection of a CCD-camera is constrained to interlace scan resulting in higher picture quality when compared to progressive scan at the same bandwidth.

Analog Interface- CCIR (Comité Consultatif International des Radiocommunications - International Radio Consultative Committee) video format regulates the transmission level and timing of a video signal. It is one of several well-documented video format standards and is used in this CCD-camera comparison out of convenience. This format implements a standard BNC cable for data transfer.

$\frac{1}{2}$ Inch CCD Size- There are several common CCD sizes ($\frac{1}{3}$ inch, $\frac{1}{2}$ inch, $\frac{2}{3}$ inch). The $\frac{1}{2}$ inch CCD size is selected as a constraint because it was selected in the baseline design and it is possibly the most common of the three common CCD sensor sizes.

The CCD-camera determined to be the baseline in this iteration of the camera-based robotic calibration system development is the Pulnix TM-6CN. Two features of this camera include manual high-speed shutter control and miniature size. Table A.2.1 compares the Pulnix TM-6CN to two possible alternatives.

Table A.1: Comparison of CCD cameras.

Specifications	Pulnix TM-260	Hitachi KP-M22-C	Pulnix TM6-CN
Digital /Analog	Analog	Analog	Analog
Colour	B+W	B+W	B+W
Lens Mount	C	C	C
Weight (g)	120	100	171
Resolution (pixels)	752x582	752x582	752x582
Frame Rate (fps)	60	50	30
S/N Ratio (dB)	50	56	50
Pixel Size (um)	8.3x8.6	8.3x8.6	8.3x8.6
CCD Size (inch)	1/2	1/2	1/2
TV Lines	560x420	560x575	560x420
Active Area (mm)		6.47x4.83	6.4x4.8
Sensitivity (lux)	0.5	0.3	0.5
Analog Interface	CCIR	CCIR	CCIR
Sync.	Internal External HD	Internal External HD	Internal
Scan Type	Interlace	Interlace	Interlace
Cost (CAD)	1,125.33	822.61	872.11

Table A.2: Comparison of CCD camera Accessories.

Specifications	Pulnix TM-260	Hitachi KP-M22-C	Pulnix TM6-CN
Power Source (CAD)	109.32	185.61 (incl. trans)	109.32
Video Transmission (CAD)	12.95 (25 ft BNC)		12.95 (25 ft BNC)
Total Cost (CAD)	122.27	185.61	122.27

Alternative one is the Hitachi KP-M22-C. This camera offers a sizable weight reduction over the baseline design and also a reduction in cost when considering the camera alone. The power and video transfer cables for the KP-M22-C (table A.2.1) raise the total cost of this camera above that of the Pulnix TM6-CN. This camera is not recommended to be used in the current design iteration of the calibration system since it offers no significant advantage over the baseline design and a cost excess.

Alternative two is the Pulnix TM- 260. The advantages with this camera are a reduction in weight and an increase in frame-rate. The frame-rate of a camera is important to applications where the objects being imaged are moving relative to the camera axis. The camera-based robot calibration system uses a stop and shoot approach to imaging a ruled surface and so all relative movement is removed and the frame-rate becomes less significant. The reduction in weight does not justify the increase in cost between the TM6-CN and the TM-260 and so the baseline Pulnix TM6-CN is recommended as the camera to be used in this system design iteration. This component will cost 1,059.10 dollars including the cost of delivery.

A.2.2 Camera Lens

The camera lens is required to magnify a clear image of a stainless steel ruled surface and project the image onto the surface of a CCD camera chip. This device is required to be rigidly mounted to a CCD camera and magnify images along the camera optical axis. The lens may also be required to rigidly mounted to the system measurement head depending on its mass.

There are three parametric constraints placed on the selection of the lens:

C-Mount Interface- The lens interface is constrained to be type C-mount in order for the lens to be compatible with the CCD-camera.

Field Coverage- The field coverage of a lens is the area of the object in sensor view that the lens can focus onto a CCD sensor of a specific size. In the case of the camera-based robotic calibration system, at least three lines on the ruled surface must be observed on the CCD at any time (these three lines allow the movement of images of lines on the ruler to be easily tracked). Three lines on the ruler correspond to three millimeters horizontal distance. Therefore, the field coverage for a CCD sensor must have at least three millimeters in the horizontal direction. This field coverage corresponds to a magnification of roughly 2x.

F-Stop- The constraint on the F-stop (less than 0.1) insures that an appropriate amount of light will pass through the lens and that the image will be sufficiently bright enough for processing.

The lens determined to be the baseline for this iteration of system design is the Rodenstock MR2/O lens. This macro lens meets all specified constraints and additionally provides compact size. Table A.2.2 offers a comparison between the Rodenstock MR2/O lens and four possible alternatives.

Table A.3: Comparison of lens component.

Specifications	Rodenstock MR2/O	Infinity InfiniStix 3X	Navitar Precise Eye 1.8X	Sill Telecentric Lens	Lippolis MQM Series
Mount	C	C	C	C	C
Magn.	2x	2x	1.8x	2x	2x
Working Distance (mm)	75	68	92	87	75
F-Stop	0.076		0.071		0.076
Coverage 1/2" CCD (mm)	3.2x2.4	3.2	3.6x2.7	3.2x2.4	3.2x2.4
Distortion (percent)	0.2			0.2	0.2
Depth of Field (mm)	0.2				0.2
Diameter (mm)	16	15	26	30-40	16
Length (mm)	72.8	90	99.1	129	75
Cost (CAD)	1,117.13	707.10		1,119.78	1,356.66

Alternative one is the Infinity InfiniStix 3x CCD-camera lens. This lens offers a significant reduction in cost, although several of the lens' characteristics have not yet been disclosed. It is expected that this lens will result in a large increase in image distortion and can not be recommended.

Alternative two is the Navtar Precise Eye 1.8x. This lens is comparable to the Rodenstock lens in most characteristics, although it's larger size and lower magnification allow it to appear less favorable than the baseline lens.

Alternative three is a telecentric lens from Sill Optics. This lens is also comparable to the Rodenstock lens in most characteristics. One disadvantage to this lens is its larger size and length compared to all other alternatives. This lens does have the advantage of being telecentric (removal of perspective distortion) while remaining extremely close in price to the baseline lens. It is for this reason that the Sill telecentric lens is the lens recommended for this iteration of the calibration system design. This component will cost 1,236.10 dollars including the cost of delivery.

Alternative four is the Lippolis MQM Series lens. This is also the most expensive lens in this analysis although it offers no significant advantage over the baseline Rodenstock lens.

A.2.3 Framegrabber

The framegrabber PC card is the device that receives the video signal from the CCD-camera in a specified format and then converts that signal into a digital image from which the PC can extract metric information. This device is inserted into one peripheral slot on the motherboard of the PC and the analog images are acquired through an interface with the CCD-camera.

There are six parametric constraints placed on the selection of the framegrabber PC card:

Analog The framegrabber must be able to accept analog signals in order achieve compatibility with the CCD-camera.

Black/White The framegrabber must be equipped to accept black and white images in order to achieve compatibility with the CCD-camera.

Analog Interface The analog interface is constrained to be CCIR video format in order to achieve compatibility with the CCD-camera.

LabView The framegrabber is required to be accessible using the LabView or Simulink software. This software is used to import images into the image-processing environment.

Interlace Scan The framegrabber is required to be compatible with interlace scan CCD-cameras.

PCI Bus The interface between the framegrabber and the PC is constrained to the PCI bus. This bus type allows the rapid transfer of high-resolution images from the framegrabber to the PC.

The framegrabber determined to be the baseline for this iteration of the system design is the NI PCI-1409. This framegrabber was implemented in the prototype design and meets all stated requirements. Two additional features include the availability of four separate inputs and 640×480 resolution. Table A.2.3 compares the NI PCI-1409 to two possible alternatives.

Alternative one is the Bitflow Raven 110. This framegrabber possesses most of the same characteristics as the NI PCI-1409 with a slight reduction in cost and the loss of the 16MB memory buffer. This design might be recommended if there was a requirement for 4 inputs on the framegrabber.

Table A.4: Comparison of framegrabber data acquisition cards.

Specifications	NI PCI-1407	Bitflow Raven 110	NI PCI-1409
Digital or Analog	Analog	Analog	Analog
Colour	B+W	B+W	B+W
Bus Type	PCI 32/33	PCI 32/33	PCI 32/33
Inputs	1	4	4
Resolution (pixels)	640x480	640x480	640x480
Data Rate (MHz)	20	30	40
Bit Depth	8	8	10
SDK (μ m)	LabView	LabView	LabView
Memory Buffer (MB)			16
Clock Type	Pixel Clock H/V Sync	Pixel Clock H/V Sync	Pixel Clock H/V Sync
Analog Interface	CCIR	CCIR	CCIR
Scan Type	Interlace	Interlace	Interlace
Cost (CAD)	959.30	1,511.42	1,649.40

Alternative two is the NI PCI-1407. This framegrabber card has only one input port compared to the 4 input ports of the PCI-1409. This calibration system only requires the use of one input port and so the large cost reduction that the PCI-1407 offers result in the recommendation of the NI PCI-1407 for this iteration of the robot calibration system design. This component will cost 1,023.05 dollars including the cost of delivery.

A.2.4 Light Source

The light source is used to maintain a certain level of illumination on the ruled surface to be imaged. It remains rigidly mounted to the measurement head, powered by a separate cable, and directed towards the area on the ruled surface currently under investigation.

There are no parametric constraints placed on the selection of the light source, but several valuable points are considered:

1 The light source must provide a high level of contrast between the surface and the markings on the surface. This will allow greater accuracy in the extraction of metric information from these images.

2 The level of illumination should be reasonably constant in all images regardless of position and orientation of the measurement head. Constant levels of illumination will allow less complexity in the image processing algorithms.

The light source determined to be the baseline for this system is a red LED array. This device requires the additional design and manufacture of a mounting board and electronics. An estimate of the cost for implementing this design suggests approximately 100 dollars for parts (cable, LED array, resistors, voltage regulator, power source) and approximately 16 man-hours for design and construction of the device. All parts can be procured locally and so no delivery charges will be required.

One possible alternative to this design is the VarioFlash system that is available from The Imaging Source. This system consists of an LED array module (385.03 dollars), a five meter cable(67.62 dollars), and a power source(104.89 dollars). The cost of delivery of these parts is estimated to be 56.63 dollars and approximately 1 man-hour should be required to integrate the system. This results in a total cost of 614.16 dollars and one man-hour for implementing this design.

The baseline system appears to be the better option. It provides large cost savings over the alternative and will be recommended for the camera-based robot calibration system.

A.2.5 Distance Sensor and Data Acquisition Hardware

The distance sensor is a device that determines the distance along the optical axis of the camera between the camera and the ruled surface. This measurement is required in the calibration of the manipulator. The distance sensor remains rigidly mounted to the measurement head, powered and communicating through a single cable, measuring distance parallel to the optical axis of the camera. The data acquisition hardware allows the information produced by this sensor to be read by the PC.

There are two constraints placed on the selection of the distance sensor and data acquisition hardware:

Resolution The sensor is required to perform measurements to within a resolution of 5um. This measurement resolution is required for the high-precision calibration of the manipulator.

Interface Format The electronic output of this sensor is required to remain compatible with some common PC data and physical format.

The baseline system for distance measurement implements a MEL M5/10 Laser Distance Sensor communicating with an Agilent 34401A Multimeter through a 25-pin D-

Table A.5: Summary of distance sensor and data acquisition sub-system baseline.

Specifications	Component Cost [CAD]	Delivery Cost [CAD]	Cost [CAD]
Agilent 34401 A Multimeter	1,543.73	97.84	1,641.60
MEL M5L / 10	2,534.34	169.30	2,703.60
NI AT-GPIB/TNT (PCI)	915.00	64.19	979.19
Total Cost (CAD)			5,324.40

connector cable. The multimeter is then interfaced through an IEEE 488 standard 24-pin connector and cable to an NI AT-GPIB/TNT (Plug and Play) ISA card that plugs into the ISA port in the personal computer. Most computers no longer implement the older ISA card interface and so the baseline is changed to an NI AT-GPIB/TNT (Plug and Play) PCI card. The estimated cost of implementing this solution as detailed in table A.2.5 is 5,324.40 dollars. This system offers rapid transfer of data with little loss in measurement data resolution over the transfer.

One possible alternative to the baseline distance sensor and data acquisition hardware is under investigation. This alternative involves the elimination of the Agilent 34401A Multimeter and the GPIB PC card. It may be possible to interface the MEL M5L/10 laser distance sensor directly to the PC serial port via the RS-232 transfer protocol. The MEL M5L/10 laser distance sensor can be packaged with an optional RS-232 interface to allow this connection. The only question that remains with respect to this interface is the loss in data measurement resolution. If this loss in resolution does not significantly effect the overall calibration error then this solution would offer significant cost savings from the

baseline. This alternative is estimated to cost 2,703.60 dollars.

A.2.6 Measurement Head

The baseline design of the camera-based robot calibration system contains little information regarding the design of the measurement head. This device is required to rigidly and easily integrate with the robot end effector of most industrial-grade robotic manipulators. The measurement head is also required to provide mounting fixtures for the camera (possibly the lens), distance sensor, LED array, and a number of cables. The measurement head should be low weight and moderately resistant to thermal distortion. It is roughly estimated that such a device could be designed and built for approximately 200 dollars and 80 man-hours of labor, although further investigation will be performed.

A.2.7 Measurement Standards

The baseline design of the camera-based robot calibration uses two measurement standards to allow the calibration. The first standard is a stainless-steel flat straight edge with dimensions $1000 \times 50 \times 10mm$. This standard provides the laser distance sensor with a reference surface to measure displacement in the z-direction. This standard is fixed horizontally with respect to the robot base coordinate system. The second standard is a stainless steel ruled surface with dimensions $1000 \times 20 \times 20$. The markings on this surface are the focus of the camera and are used to determine the displacement of the robot in the x- and y-directions. The ruled standard is fixed parallel to the flat standard in the horizontal plane with respect to the robot base coordinate system.

The alternative measurement standard is a precision ruled surface from Schlenker Enterprises Limited. This ruler can be purchased for a total cost of 578.72 dollars including delivery. There is little information given regarding the flatness of this device when compared to the certificate issued from PZA regarding the accuracy of their device. This

Table A.6: Estimated cost of flat and ruled measurement standards.

Component	Cost [CAD]
PZA Straight Edge w/certificate 131011000	134.50
PZA Precision Rule w/certificate 140001000	550.82
Cost of Packaging and Delivery	117.63
Total Cost (CAD)	802.95

accuracy will most certainly be required for the system under design. Also, a quote was not issued (although it was requested) regarding the unruled and flat measurement standard also required for this calibration system. The implementation of this device results in little cost savings when considering the cost of delivery of this one piece from Schlenker Enterprises Ltd. and the flat standard from PZA. As a result, this device will not be recommended.

The baseline design will be recommended for the current iteration. The costs associated with this design are detailed in table A.2.7, but the total cost of obtaining these parts is 802.95 dollars.

A.2.8 Personal Computer

There was no baseline specification regarding the selection of a personal computer. As a requirement, this device must contain all input and output ports required by the other devices in the system. These ports include a PCI slot for a framegrabber card, a serial

port for the distance sensor and a serial port for use with the robot controller. An optional port that may be considered in the future is an interface for operation the LED array. This connection is not required right at this point in time.

This PC that is recommended for this iteration of the calibration system design is the Digital Design Bronze Package available from CompuNation Computers Inc. in Ottawa. There no cost of delivery associated with this product since it can be procured locally. This PC includes peripherals such as a monitor, keyboard and mouse, as well as a motherboard with 3 available PCI slots. The cost of this system is 1493.89 dollars.

A.3 Summary and Conclusions

A rough estimate of the total cost of this system is now available. Table A.3 is a summary of the costs that will be incurred through the purchase and acquisition of each recommended component as well as an estimate of the man-hours required for integration and testing. The cost of this system is estimated to be 8,618.69 dollars and 426 hours of labor.

This cost estimate of 8,618.69 dollars represents the cost of the system recommended by the author of this document and is based on the reduction of system costs and the maintaining of system performance. A table summarizing the cost associated with using the baseline system can be found in section A.6. It can be noted that the recommended system offers a savings of 3,260.44 dollars over the baseline system with the potential for no loss in performance.

A.4 Cost of Delivery Estimate

The estimate of cost of delivery is calculated using the Federal Express rate of delivery calculator found on the internet at the following address.

$http://www.fedex.com/ratefinder/shipInfo.$

Table A.7: Summary of suggested system components.

Component	Labor Required [hours]	Cost of Component including delivery [CAD]
Camera Pulnix TM6-CN	80	1,059.10
Lens Sill Telecentric Lens	40	1,236.10
Framegrabber NI PCI-1407	40	1,023.05
LED Array and Electronics	16	100.00
MEL M5L/10 w/Serial Comm.	80	2,703.60
Measurement Head	80	200.00
Measurement Standards	40	802.95
Personal Computer	10	1,493.89
Total Cost	426	8,618.69

This calculator uses location and destination of the parcel, the mass of the parcel, an assumption regarding the shape of the parcel, and the estimated cost of the parcels contents to estimate the rate of cost of its delivery. This estimate includes most or all necessary tariffs associated with international delivery and courier pick-up of packages being delivered from a location within Canada or the United States. All rates assume the that the parcels are being delivered to the Canadian postal code **K1S 5B6**. This code refers to the location of Carleton University in Ottawa, Canada.

A.5 Cost of Integration and Testing

The integration and testing phase of the camera-based robot calibration system development is the period of time during which all parts have been acquired and the only resource being used is man-hours of labor. The estimates of man-hours required are loosely based on a combination of the cost and the interface complexity of the parts being integrated. This basis assumes that more time should be spent with parts that cost more because these parts will be more difficult to replace. Also, parts that have complicated interfacing requirements (ie, require programming, mounting) will require more time to integrate. There are two categories of time allotment that are implemented. The first category is the work-day (8 man-hours). Parts that fall into this category require very little time to integrate (1 hour) and the remainder of a day to thoroughly test that the part is functioning exactly as expected. Some examples of work-day parts include cables and power sources. The second category is the work-week (40 man-hours). Parts that fall into this category require a larger integration time as a result of a more complex interface (ie, hardware/software design). Some examples of work-week parts include the framegrabber and distance sensor. Table A.5 is a list of all components and an estimate of the time required for integration and testing.

Table A.8: Cost of delivery estimation.

Product/Model	Distributor	Location Postal/Zip Code	Estimated Mass Camera+Accessory [kg]	Estimated Cargo Value [CAD]	Estimated Cost of Delivery via FedEx [CAD]
Camera Hitachi KP-M22-C	OPSCI	Colorado Spr.,CO USA 80918	0.100+0.3	818.59+185.61	64.76
Camera Pulnix TM-6CN	OPSCI	Colorado Spr.,CO USA 80918	0.171+0.3	872.11+122.27	64.76
Camera Pulnix TM-260	OPSCI	Colorado Spr.,CO USA 80918	0.120+0.3	1,125.33+122.27	65.86
Lens Rodenstock MR2/O	The Imaging Source	Charlotte,NC USA 28204	0.2	1,117.13	65.30
Lens Infinity InfiniStix	Infinity Photo-Optical Co.	Boulder,CO USA 80301-2458	0.2	707.10	63.65
Lens Navitar Precise Eye	Navitar	Rochester,NY USA 14623	0.2		
Lens Sill Telecentric	Eureca Messtechnik GmbH	Koln Germany 50769	0.2	1,119.78	116.32
Lens Lippolis MQM Series	Lippolis Optical-Video Tech.	Rescaldina,MI Italy 20027	0.2	1,356.66	75.42
Framegrabber NI PCI-1407	OPSCI	Colorado Spr.,CO USA 80918	0.1	959.30	64.21
Framegrabber Bitflow Raven 110	OPSCI	Colorado Spr.,CO USA 80918	0.1	1,511.42	66.42
Framegrabber NI PCI-1409	OPSCI	Colorado Spr.,CO USA 80918	0.1	1,649.40	66.97
VarioFlash Cable Power Supply	The Imaging Source	Charlotte,NC USA 28204	0.08 0.1 0.1	385.03 67.62 104.89	56.63
Agilent Multimeter 34401A	Tequipment.net	Hazlet,NJ USA 07730	3.6	1136.00	97.83
Sensor MEL M5L/10 laser	Laseroptronix	Vallentuna Sweden 18362	0.1	2,534.34	169.30
GPIB NI PCI	National Inst.	Austin,TX USA 78759-3504	0.1	915.00	64.19
Ruler 1000x20x20 Precision	Schlenker Enterprises Ltd.	Hillside,IL USA 60162	4.0	479.14	99.58

Table A.9: Labor required for integration and testing of specific components.

Component	Labor Required [man-hours]
Camera	80
Lens	40
Framegrabber	40
LED Array and Electronics	16
VarioFlash System	8
Sensor/Multimeter/ GPIB System	80
Sensor w/Serial Comm.	80
Measurement Head	80
Measurement Standards	40
Personal Computer	10

Table A.10: Summary of system costs for the baseline system.

Component	Labor Required [hours]	Cost of Component including delivery [CAD]
Camera Pulnix TM6-CN	80	1,059.10
Lens Rodenstock MR2/O	40	1,182.43
Framegrabber NI PCI-1409	40	1,716.37
LED Array and Electronics	16	100.00
Distance Sensor MEL M5L/10	80	2,703.60
Agilent 34401A Multimeter	(included in MEL)	1,641.60
NI AT-GPIB / TNT (PCI)	(included in MEL)	979.19
Measurement Head	80	200.00
Measurement Standards	40	802.95
Personal Computer	10	1,493.89
Total Cost	426	11,879.13

A.6 Baseline System Component List

The baseline camera-based robot calibration system was designed by Markus Leitner of Steinbichler while attending the Institute for Automation at the Mining University in Leoben, Austria. The costs associated with obtaining and assembling the components for this baseline design are summarized in the following table.

A.7 Estimation of Cost of Purchased Parts

Table A.11: Summary of system components purchased for the camera-based calibration system.

Component	Labor Required [hours]	Cost of Component [CAD]
Camera Pulnix TM-200	80	839.00
Lens Rodenstock Macro 1X	40	924.55
Framegrabber NI PCI-1409	40	1,723.50
LED Array and Electronics	16	842.43
Measurement Head	80	200.00
Measurement Standards	40	635.93
Personal Computer	10	1,500.00
Total Cost	426	6,665.41

Appendix B

Measurement Head Design

The design of the measurement is based on several requirements. The first requirement is based on the limitation of the robotic end-effector. The Thermo CRS A465 manipulator has a maximum rated payload of 2.0 kg. The positional repeatability of the robot is based on this payload. Any loading that exceeds 2.0 kg will result in a decrease in positional repeatability. Since the repeatability of the system is very important for the purpose of extracting positional errors, 2.0 kg is the requirement for the maximum mass of the measurement head with all calibration system components fully integrated. The mass of all of the components that must be integrated with the measurement head are listed in table B.1.

Given the requirement for a total payload of less than 2.0 kg and the 0.607 kg mass of all components attached to the measurement head, the mass of the measurement head

Table B.1: Summary of components to be integrated with the measurement head.

Component	Mass
Camera	157 g
Lens	100 g
LED Array	150 g
Cabling	200 g
Total	607 g

structure is not to exceed 1.393 kg. The magnitude of the maximum mass is considered large and does not drive the design of the measurement head. The design is based on the geometry of the components which can be observed in the equipment data sheets. The following figures describe the geometry of the measurement head. The final mass of the measurement head is given as approximately 0.2 kg.

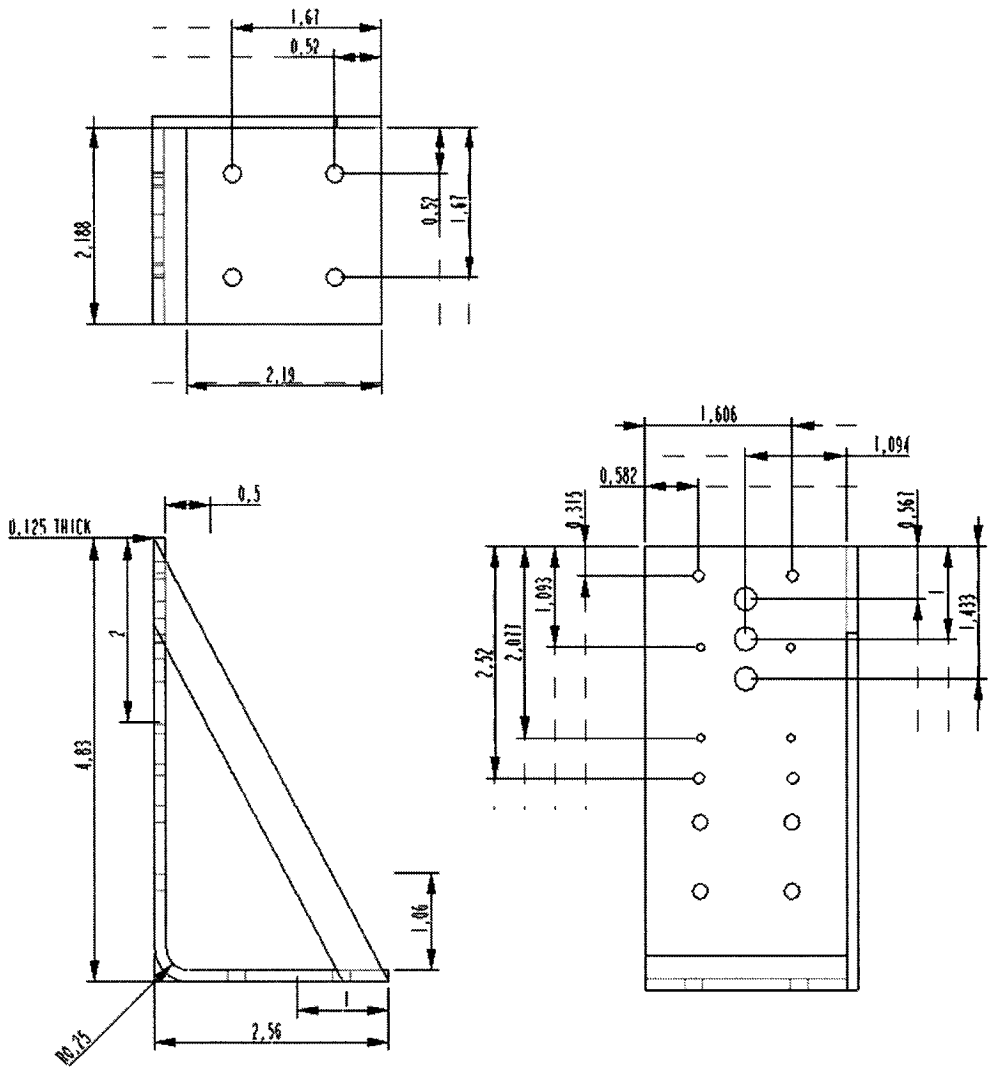

Figure B.1: Schematic diagram of the measurement head structure.

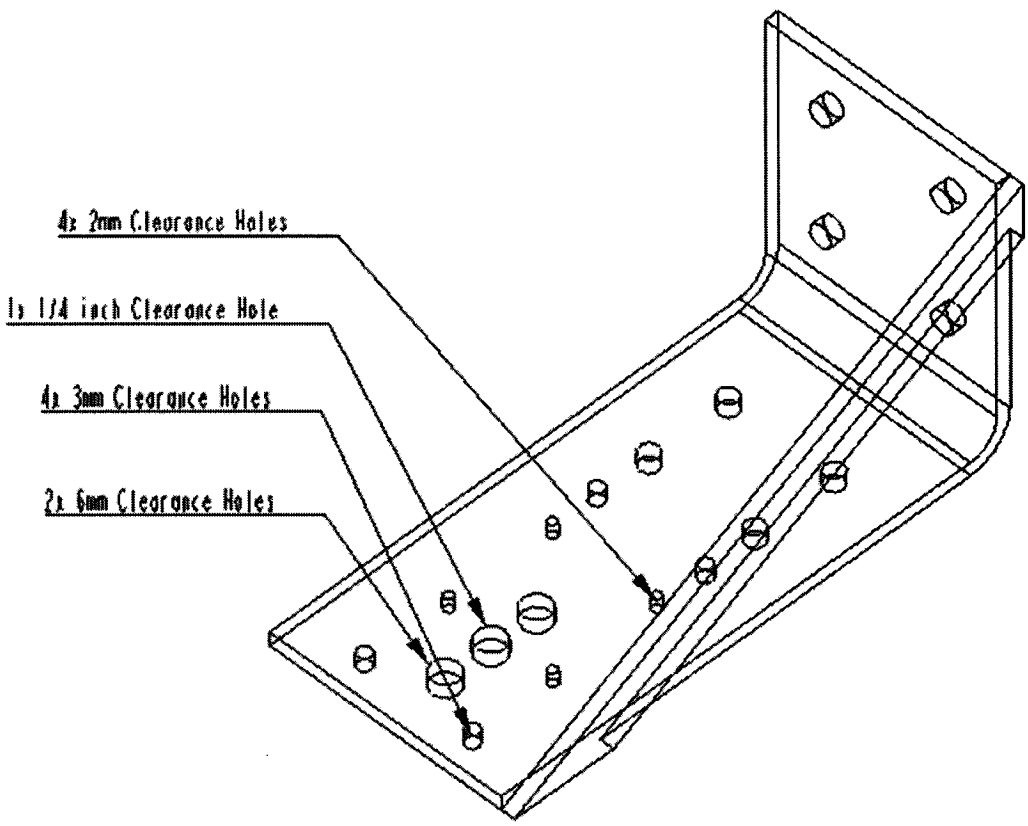

Figure B.2: Orthographic view of the measurement head labeling the size of attachment holes - the holes used for attaching the measurement head to the robot end-effector plate are no. 10 clearance holes.

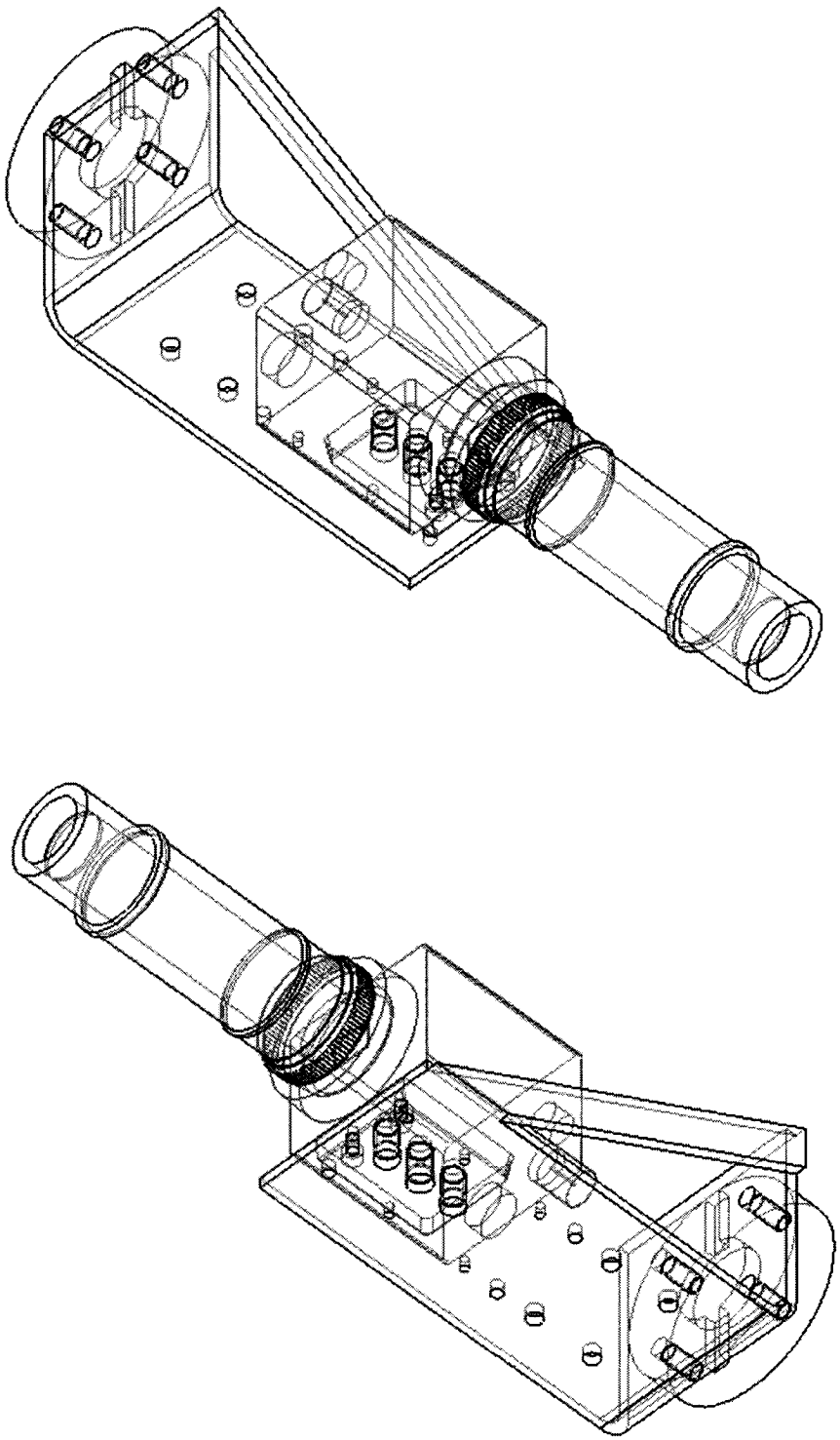

Figure B.3: Wire-frame model of the complete camera/lens/measurement head structure.

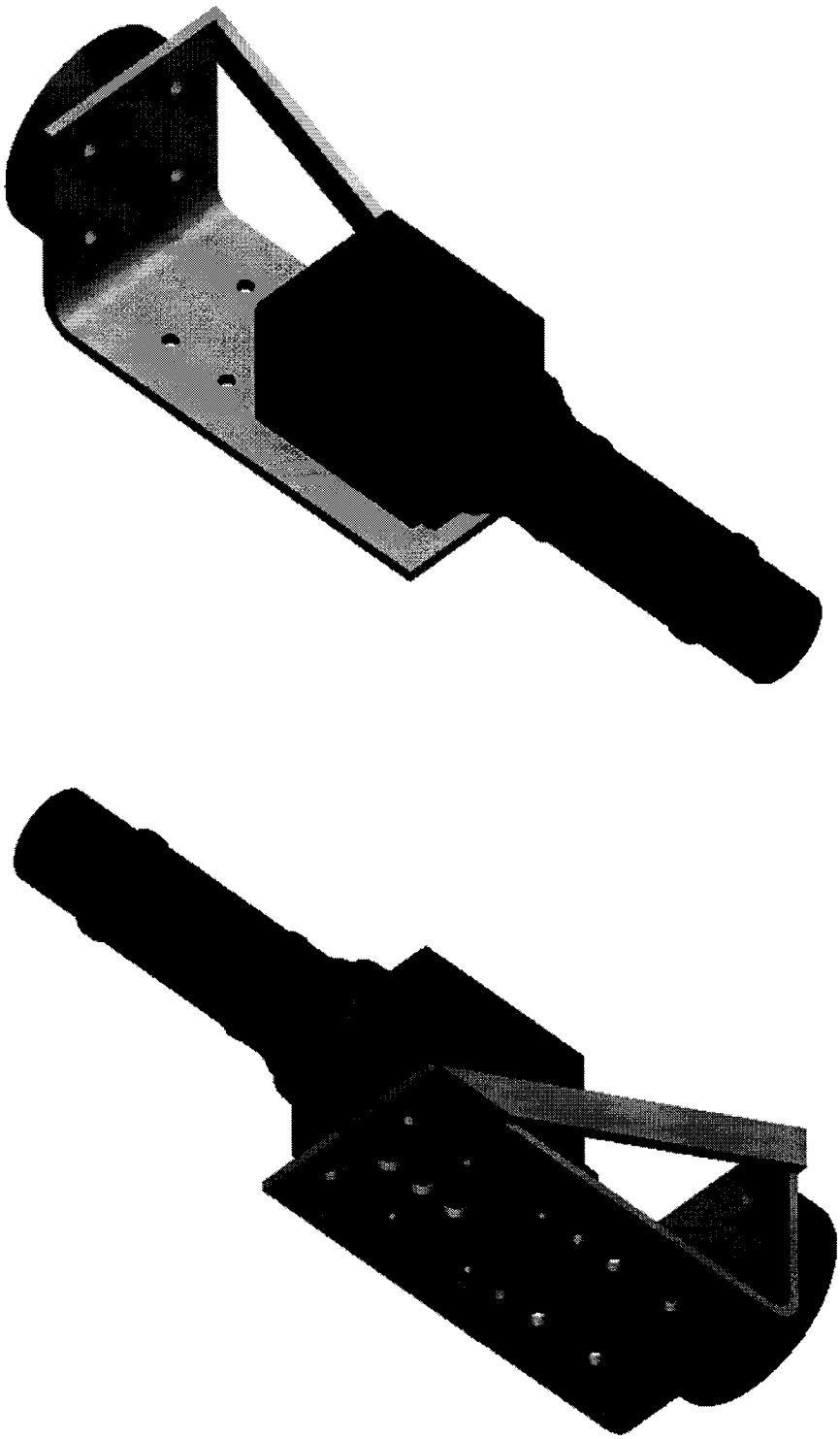

Figure B.4: Rendered model of the complete camera/lens/measurement head structure.

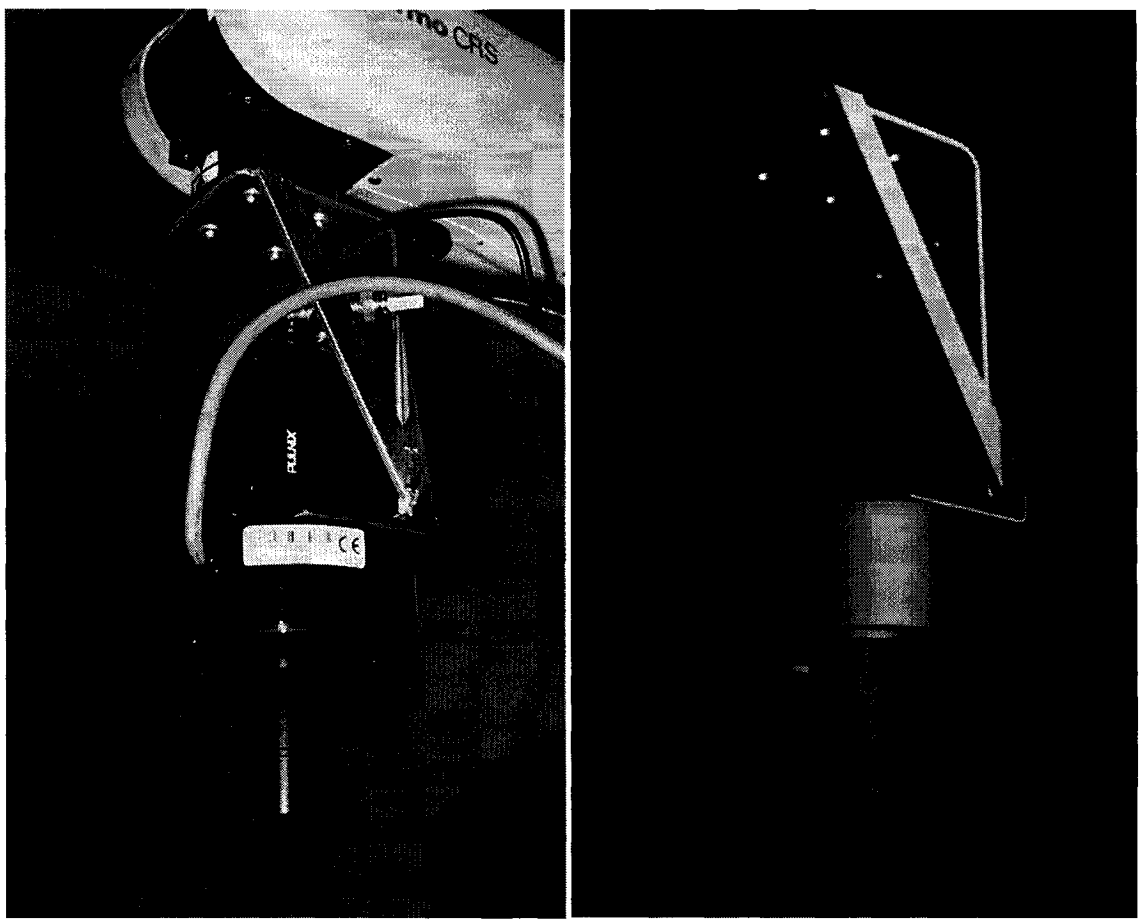

Figure B.5: Comparison between the modeled camera/lens/measurement head assembly and the actual assembly.

Appendix C

Comparison Data Tables

Table C.1: Noise filter comparison data.

Type of Filter	Average Error *PT* data (mm)	Maximum Error *PT* data (mm)	Average Error *IS* data (mm)	Maximum Error *IS* data (mm)
No Filter	0.0183	0.0593	0.0082	0.0211
Mean	0.0131	0.0573	0.0085	0.0217
Gaussian	0.0121	0.1506	0.0082	0.0202
Median	0.0160	0.1727	0.0081	0.0205
Directional	0.0138	0.0861	0.0085	0.0219

Table C.2: *TestHeight* parameter comparison data.

Value of Parameter	Average Error *PT* data (mm)	Maximum Error *PT* data (mm)	Average Error *IS* data (mm)	Maximum Error *IS* data (mm)
2	0.0122	0.0403	0.0084	0.0214
5	0.0131	0.0573	0.0085	0.0217
10	0.0127	0.0659	0.0085	0.0217
15	0.0142	0.1585	0.0085	0.0217
20	0.0150	0.1583	0.0085	0.0217

Table C.3: *TestWidth* parameter comparison data.

Value of Parameter	Average Error *PT* data (mm)	Maximum Error *PT* data (mm)	Average Error *IS* data (mm)	Maximum Error *IS* data (mm)
2	0.0141	0.0647	0.0082	0.0218
5	0.0131	0.0573	0.0085	0.0217
10	0.0140	0.1553	0.0084	0.0212
15	0.0135	0.1527	0.0085	0.0195
20	0.0159	0.0372	0.0087	0.0191

Table C.4: *LCCmin* parameter comparison data.

Value of Parameter	Average Error *PT* data (mm)	Maximum Error *PT* data (mm)	Average Error *IS* data (mm)	Maximum Error *IS* data (mm)
0.8	0.01305671	0.0572754	0.00848598	0.02174108
0.82	0.01354395	0.15255998	0.0083728	0.02145782
0.84	0.01470428	0.15420789	0.00839479	0.02145569
0.86	0.01695737	0.15896871	0.00834059	0.02100924
0.88	0.01996002	0.21340955	0.00827924	0.02049826

Table C.5: *Percentage Elimination* parameter comparison data.

Value of Parameter	Average Error *PT* data (mm)	Maximum Error *PT* data (mm)
0	0.01306	0.05728
5	0.01301	0.05719
10	0.01299	0.05716
15	0.01298	0.05721
20	0.01298	0.05728
25	0.01299	0.05738
30	0.01299	0.05740
35	0.01298	0.05733
40	0.01297	0.05736
45	0.01296	0.05736